PARTICLES AND FIBERS IN FLUID FLOWS FOR ENVIRONMENTAL APPLICATIONS

BY

MATTIA CAVAIOLA

Dissertation discussed in partial fulfillment of
the requirements for the Degree of

DOCTOR OF PHILOSOPHY

Civil, Chemical and Environmental Engineering
curriculum in Fluid Dynamics and Environmental Engineering,
Department of Civil, Chemical and Environmental Engineering, University of Genoa, Italy

April, 2022

Adviser(s):
Prof. Andrea Mazzino - DICCA, University of Genova

External Reviewers:
Prof. Paolo Gualtieri - Dipartimento di Ingegneria Meccanica e Aerospaziale, Sapienza Università di Roma, Roma Italia
Prof. Sergio Chibbaro - Institut Jean Le Rond D'Alembert, Sorbonne Université, Paris France

Examination Committee:
Prof. Michele Bolla Pittaluga - Dipartimento di Ingegneria Civile, Chimica e Ambientale, Università di Genova
Prof. Costantino Manes - Dipartimento di Ingegneria Ambientale, del Territorio e delle Infrastrutture, Politecnico di Torino
Prof. Rosaria Ester Musumeci - Dipartimento di Ingegneria Civile e Architettura, Università di Catania
Prof. Luca Solari - Dipartimento di Ingegneria Civile e Ambientale, Università di Firenze
Prof. Rodolfo Repetto - Dipartimento di Ingegneria Civile, Chimica e Ambientale, Università di Genova

Ph.D. program in Civil, Chemical and Environmental Engineering
Curriculum in Fluid Dynamics and Environmental Engineering
Cycle XXXIV

ABSTRACT

The thesis is divided in two parts showing applications of active and passive models, in which the Lagrangian tracking of rigid fibers and slender swimmers can be employed to access to flow properties, and to study a turbulent puff in order to access information on spreading of virus-containing droplets.

The first part of the thesis addresses the measure of flow properties by means of slender objects, i.e. rigid fibers. Two different strategies have been employed to model the fiber: first an active model, a fully-coupled fiber described in terms of an immersed-boundary method, and, second, a passive model, a one-way coupling where the fiber is described by the slender body theory. After the characterization of the fiber inertia in terms of rotational Stokes Number, the motion of the fiber is investigated for different classes of closed streamline flows, steady or time dependent, two-dimensional or three dimensional. For sufficiently small Stokes, the fiber turns out to be a proxy of the underlying flow by considering the velocity difference between the fiber end points and the same difference relative to the underlying fluid velocity, both projected along the direction normal to the fiber. Moreover, by composing an assembly of rigid fiber, the whole flow gradient tensor can be accurately reconstructed by simply tracking the fiber assembly and measuring suitable fiber velocity differences evaluated at the fiber ends.

Furthermore, it has been investigated the possibility to measure two points flow properties by means of slender swimmers. A swimmer model, describing both pusher and puller swimmers, has been proposed and validated in the Stokes limit finding excellent agreement. The slender swimmer model has been exploited in a chaotic flow field up to a flow Reynolds number of 10, a swimming number ranging between zero and one and different swimmer inertia measured in terms of a suitable definition of the swimmer Stokes number. The following results have been obtained: (i) pusher and puller reach different swimming velocities for the same, given, propulsive force, due to a different distribution of the vorticity within the wake. (ii) for a wide range of flow/swimmer Reynolds numbers, both pusher and puller swimmers are able to sense hydrodynamic signals with good accuracy.

The second part of the thesis is devoted to understand the role of the turbulence on the fate of virus-containing droplets expelled during a human cough, modeled as a turbulent puff, under realistic conditions. To this aim, high resolution DNS have been performed for the fluid flow and humidity field, complemented by a passive Lagrangian solver for the droplet dynamics including a dynamical equation for the evolution of the droplet radii modeling the evaporation-condensation process. After having validated the turbulent puff against theoretical predictions, the results show how a full account of turbulence is crucial to determine the fate of virus-containing droplets. Then, the dependence of the results on the droplets initial size distribution and different ambient humidity is investigated. As a further step, it is analyzed the dependence of results on the airborne virus spreading on gender. Finally, the effectiveness of the barriers as protection devices within indoor environment is investigated.

This study is clearly motivated by the recent pandemic situation due to COVID-19 infection, although it is valid for all the infections where the main route of transmission is via airborne virus-containing droplets, by contributing to select optimal strategies of protection and mitigation of the airborne infection transmission, within indoor and outdoor environments.

INDEX

Chapter 1
Introduction

The study of the physical flow properties is an interesting and widely addressed research topic. The importance range from small-scale problems, such as suspensions dynamics [1] or flow in porous media [2] to large-scale problem in meteorology and oceanography[3]. In recent years, efforts have been made to introduce novel techniques able to access flow properties in a more detailed and convenient way based on Lagrangian tracking of fibers, both numerically and experimentally [4, 5, 6]. Moreover, experimental analyses have outlined the potential of using dispersed rigid rods as a new paradigm to measure flow properties in turbulence [7], since their tumbling rate is found to be approximately equal to the characteristic time of turbulent structures of comparable size (provided inertia does not affect the fiber dynamics [8, 9]). Also the case of flexible fibers has been recently addressed both experimentally [10] and numerically [5]. One of the main findings is the identification of a flapping regime where the fiber deformation is slaved to turbulent fluctuations, enabling to quantify their statistical properties by measuring only the distance and velocity difference between the fiber free ends. Further attempts of such a Lagrangian description have seen the employment of other kinds of particles for evaluating both two-point (limited to distances between particles smaller than the Kolmogorov viscous scale) and single-point quantities [11, 12], paving the way for new strategies to investigate turbulent flows.

On the other hand, the analysis of flow properties is an useful strategy to obtain information on particles motions. Nowadays, the study of particle spreading is another hot topic, covering aspects ranging from pollution dispersion in urban environment, erosion and sediment transport to the spreading of airborne diseases. Flows of this kind are characterized by particles, droplets or bubbles dispersed within a carrier phase. The ability to predict the behaviour of this kind of flow is therefore of considerable interest. However, due to the complexity of these flows, available models are usually crude simplifications and cannot predict fluid and particle behaviour for the whole range of process conditions of interest [13]. Pope [14] and Yeung [15] developed stochastic models of turbulent transport with promising results. For the development of stochastic models, the experimental determination of statistical properties of particles in a Lagrangian frame is essential. However, the study of the particle motion in a numerical framework is clearly simpler with respect to an experimental analysis. The most popular numerical approach is the Eulerian-Lagrangian approach, which can be applied under various assumptions. In some problems, such as the dispersion of atmospheric pollutants, it may be assumed that the particles do not perturb the flow field. Then, the solution involves the tracing of particle trajectories in a known velocity field [16].

By focusing on numerical approaches, this thesis will show applications of active and passive models, in which the Lagrangian tracking of rigid fibers and slender swimmers can be employed to access to flow properties, and to study a turbulent puff in order to access information on spreading of virus-containing droplets.

Active and passive models can be used to model slender objects or particles in various environmental fluid-flow applications. In other words, we are speaking about the fluid-structure interaction (FSI), which is a multiphysics coupling between the laws that describe fluid dynamics and structural mechanics. This phenomenon is characterized by interactions, which can be stable or oscillatory, between a deformable or moving structure and a surrounding or internal fluid flow. With active models we mean that the immersed object is fully coupled to the fluid flow, i.e. a two-way coupling interaction. The body acts on the surrounding fluid, forcing it to move with its boundaries, by enforcing the no-slip condition. On the other hand, the fluid exerts forces on the body through pressure differences and viscous shear stress. In contrast, in a passive model, i.e. one-way coupling, the object dynamics is affected by the underlying flow but it does not react back to the flow.

The one-way coupling approach provides a formally clean framework to examine in detail the influence of turbulence on particles at low particle concentration, but gives no information regarding the influence of particles on turbulence and particle-particle interactions. In the case of rigid particles with ellipsoidal shape and which are sufficiently small to evolve in a Stokes flow with negligible fluid inertia, an analytical expression for the fluid torque acting on the particle was originally derived by Jeffery [17]. Such a result has been later generalized to other shapes and widely exploited in a variety of problems. These include studies on the rheology of suspensions in low-Reynolds-number flow conditions (Butler and Snook [18]), as well as on the dynamics of dispersed fibres in turbulent flows. The main findings of these works are related to orientation and rotation statistics, which show a tendency of fibers to align in the direction of the mean flow close to the wall, and to the preferential concentration of particles. The same observables have also been evaluated in Direct numerical simulations of isotropic turbulence (e.g. see Refs.[19, 20, 21] and references therein) in which fiber alignment induced by the fluid velocity gradients resulted in rotation rates much lower than those predicted by rotationally averaged models.

The main assumptions characterizing the one-way coupling approach for fibers are that they are approximated as non-interacting ellipsoids with uniformly distributed mass immersed in a dilute flow. Additionally, the fiber size is assumed to be smaller than the Kolmogorov length scale, and lubrication forces arising when particles are in close proximity are ignored. Also ignored are aggregation and breakup phenomena [1]. Other examples are studies which applied Lagrangian tracking of particles in large-eddy simulation (LES)-resolved turbulence fields [22]. Njobuenwu and Fairweather [23] studied the effect of particle shape on their dynamics in an LES-resolved turbulent channel flow. They used shape-and orientation-dependent drag and lift coefficients to solve for translational and rotational motions of oblate and prolate ellipsoids. Lecrivain et al. [24] studied the sedimentation of fibers in flat and roughened channels using quasi-DNS resolution. On the other hand, Bianco et al. [25] observed that the filtered subgrid-scale fluid motions in LES flow fields have significant effects on the rotational statistics of ellipsoidal particles. In fact, filtering the fluid velocity field yields approximate computation of the forces acting on particles and, in turn, trajectories that are inaccurate when compared to those of Direct numerical simulations.

Another interesting application of passive model, which highlights the importance of taking into account all scales of turbulence, can be found in Celani et al. [26] in the field of cloud microphysics. They addressed the problem of droplet growth by condensation in a turbulent flow of nearly saturated vapour, both theoretically and numerically. By means of direct numerical simulations of the turbulent flow velocity, which advects a vapour field, and of the evolution of droplet trajectories and radii, they showed the presence of a correlation between droplet trajectories and supersaturation field, leading both to the enhancement of the droplet growth rate and to a fast spreading of the droplet size distribution. In that study, the use of a passive model was justified because the droplets volume fraction is sufficiently small so that to neglect the back reaction of the droplets to the flow.

In the case of high volume fraction, even small particles will influence the fluid momentum. Owing to preferential concentration and clustering, this can occur locally as well as globally. A more complete view of multiphase flows can be gained calling into play two-way, i.e. by accounting for the inter-phase momentum exchange [27]. In dense flows, interparticle collisions may also become important, leading to aggregation or fragmentation with direct and indirect effects on the collective dynamics of the particles [1]. Eulerian-Lagrangian fully coupled simulations for fibers on the order of the Kolmogorov scale in turbulent channel flow have been performed to examine the collision mechanisms of fibers with the walls (see Ref. [28]), as well as the physics of fiber-induced turbulence modulation and its dependence on fiber length [29]. These aspects are investigated for semidilute concentrations considering statistical observables based either on fluid and fiber velocities (e.g., turbulent kinetic energy, fluid-fiber correlations) or on fiber orientation (e.g., direction cosines). The cases of flexible fibers with finite size, in homogeneous isotropic turbulence, is very far from the realm of application of Jeffery's model for at least three main reasons. The fibers are elastic, inertial and they do not evolve locally in a linear flow (i.e. their size is well within the inertial range of scales). Nowadays, systems involving flexible bodies interacting with a surrounding fluid flow are commonplace, for example flapping flags and swimming fishes, are becoming increasingly prevalent in biological engineering applications. Moreover, as already said before, recent works have highlighted the possibility to use flexible and rigid fibers to quantify turbulence two-point statistics, both numerically and experimentally [5, 6, 4]. Many numerical experiments, as the ones mentioned before, involving fibers immersed in turbulent and laminar flows, are conducted by means of the immersed boundary (IB) method, in order to simulate interactions between fluids and structures. Due to its greatly simplified grid generation requirement, the IB method has received much attention. In literature many versions of the IB method can be found. For example, Huang et al. [30] developed a version of the IB method for simulating anchored flexible filaments in a uniform flow.

The IB method was originally developed by Peskin [31] to simulate cardiac mechanism and associated blood flow. While the fluid is represented on an Eulerian grid, the structure is represented on a Lagrangian coordinate. The Eulerian fluid motion and the Lagrangian IB motion are solved independently and their interaction force is calculated explicitly using a feedback law. Then, the core of the IB method is based on two simply concepts: interpolation and spreading. The forcing, acting on the structure, is first evaluated at each Lagrangian point, in order to enforce the no-slip, by interpolating the fluid velocity at the Lagrangian points. Then a spreading operation is performed over the surrounding Eulerian points, yielding the forcing acting on the flow equations. Both interpolation and spreading feature a Dirac operator. Spring forces, bending resistance or any other type of behavior can be built into this term. Immersed boundary solvers have been employed successfully for simulating biological flows, physiological flows, flow-induced vibration and complex turbulent flows.

The IB method has been used for a wide range of problems, from strictly engineering to biofluid dynamics applications. For example, Olivieri et al. [32] used a computational framework based on the immersed boundary method to investigate the flag-in-the-wind problem exploring the effect of the turbulence intensity on self-sustained flapping. Moreover, the IB method show great capabilities for a number of biological problems. Mittal et al. [33] used the IB method to simulate the flows associated with biological locomotion, both flying and swimming. Also hydrodynamic interaction between swimming organisms has long been a topic of interest in fluid-structure interaction. Especially, collective motion of swimming organisms such as bacteria, spermatozoa, and worms has recently received a great deal of attention from researchers. Mirazimi [34] examined individual, pairwise, and collective interactions of worms observing phenomena such as synchronization, attraction as well as aggregation, in dilute suspensions of swimmers. Another important application of the IB method is given by Dillon et al. [35]. They described how biofilm processes, which are of interest to researchers in a variety of fields including bioremediation, oil recovery, waste-water treatment, medicine, and dentistry, can be modelled successfully using the IB method.

In this thesis active and passive models have been used for two different environmental flow applications. Chapter 2 will show how rigid fibers and slender swimmers, i.e. self-propelled slender objects, can measure two-point flow properties (velocity differences between two points or flow gradient components). Here, the main focus is on active models. To this aim, direct numerical simulations exploiting a state-of-the-art immersed boundary technique, to model the slender object fully coupled to the fluid flow, have been carried out in laminar cellular flows, both in two and three dimensions, time dependent and time independent. The choice of these flow configurations allows a direct and reliable comparison between the unperturbed flow velocity, which is known analytically, and the fiber velocity. After having characterized the inertia of the slender object via the rotational Stokes number, it will be presented the technique to access to the velocity differences and gradient components of the fluid flow, by means of immersed slender objects. Chapter 3 investigates the role of the turbulence on the fate of virus-containing droplets expelled during a human cough under realistic conditions. Direct numerical simulations have been performed for the fluid flow and humidity field, complemented by a passive Lagrangian solver for the droplet dynamics including a dynamical equation for the evolution of the droplet radii modeling the evaporation-condensation process. Specifically, the combined role of turbulence and droplet inertia on the virus-containing droplet evaporation will be investigated. Then, the influence of different ambient humidity conditions and different initial size distributions of the droplet, taken from literature, have been considered. As a further step, it will be investigated the influence of the gender of the emitting subject in the dynamics of violent expiratory events in order to better characterize the transport and evaporation process undergone by the exhaled saliva droplets. Finally, the spread of the virus-containing droplets in indoor environments will be studied, where a barrier used as protection device from disease infection is present, considering two different ambient humidities.

Chapter 2
Fibers and slender swimmers measure flow properties

The aim of this chapter is to show the possibility to measure two-point flow properties (i.e. flow velocity differences between two points or, more generally flow gradient components) by means of rigid fibers fully coupled to the flow field, with or without internal propulsion. In both case our fibers are slender and rigid. All numerical experiments have been performed by Direct numerical simulations exploiting a state-of-the-art immersed boundary technique to model the fluid-structure interactions. Hence, the main focus is on active models where the immersed objects are fully coupled to the fluid-flow. Our numerical experiments are carried out in cellular flows both in two and three dimensions, time dependent and time independent. The relative simple structure of these flow configurations allows us to perform the numerical experiments under controlled conditions. For the selected flow field, the unperturbed velocity is indeed known analytically, a fact that allows us accurate comparison of the unperturbed flow properties against those reconstructed in terms of our fibers. The chapter is structured as follow: Sec. 2.1. presents the state-of-the-art and research motivations, Sec. 2.2. presents the employed numerical approach to model rigid fibers and slender swimmers, Sec. 2.3. characterizes the inertia of the slender objects via the rotational Stokes number, Sec. 2.4. shows the measure of flow properties by means of slender objects and finally Sec. 2.5. draws the conclusions related to this chapter.

2.1. Background and research area

Fiber-like objects interacting with fluid flows are typically encountered in many environmental and industrial processes, such as pollutant and pollen dispersion, microfluidic devices and paper production. Compared with point-like particles, the dynamics of fiber-like objects is more complex due to the additional degrees of freedom related to the object orientation and structural elasticity. Active research is thus being devoted to improve the understanding of such fluid-structure interactions, both in laminar and turbulent flow conditions [36, 1].

In the laminar case, flapping instabilities of flexible filaments immersed in two-dimensional, low-Reynolds flows were identified [37] and similar mechanisms were investigated to be exploited for passive locomotion and flow control purposes [38, 39, 40].

In the case of turbulence, dilute suspensions of both rigid and deformable fibers were investigated in different flow configurations, including the case of wall-bounded channel flow [41, 42, 43], as well as that of homogeneous isotropic turbulence [20, 44, 45, 9, 46, 47].

More specifically, some recent contributions have considered this kind of objects as the key ingredient for a novel way of flow measurement. In particular, the possibility of using flexible fibers to quantify two-point statistics has been highlighted in the case of homogeneous isotropic turbulence by means of fully-resolved direct numerical simulation [5, 6]. In this situation, the existence of different fiber's flapping states was identified, in some of which the fiber behaves as a proxy of turbulent eddies with size comparable to the fiber length. Two-point statistical quantities, such as the velocity structure functions, were thus acquired simply by tracking the fiber end points in time. Along a similar line of reasoning, recent experimental studies focused on how to measure fluid velocity gradients using particles made by connections of slender deformable arms, both in the case of two-dimensional shear flow and three-dimensional turbulence [11]. Furthermore, Brizzolara et al. [4] proposed and validated a novel experimental technique to measure two-point statistics of turbulent flows. It consists in spreading rigid fibers in the flow and tracking their position and orientation in time and therefore it has been named "Fiber Tracking Velocimetry" (FTV). The idea is to replace single particles, typically used in particle image or tracking velocimetry (PIV/PTV) to measure single-point fluid properties [48, 49, 50], by single fibers (or assemblies of them) in order to access two-point (or multi-point) properties. A well-known issue of tracer-based techniques, such as PIV or PTV, is the evaluation of two-point statistical quantities, which are of special interest in turbulence. A significant problem, when using particles/tracers to evaluate turbulence statistics, is that two particles tend to separate from each other (following the Richardson diffusion law, where the relative distance between two particles initially close enough grows in time as $t^{3/2}$), thus making it practically impossible to obtain converged statistics for a fixed separation distance. Moreover, technological limits make it difficult to measure small-scale quantities, such as gradient tensor or shear rate. This in view of the extremely high number of particles needed to access these small-scale quantities [4]. The reason for considering fibers instead of particles is rather simple and relates to the fact that the distance between the two ends of the fiber is constant. The main result in the literature is that finite-length fibers (i.e., fibers whose length falls within the inertial range) rotate (rigid fibers) [51] or deform (flexible fibers) [5] at the same frequency as the turbulent eddies of comparable size.

Motivated by these evidences, the goal of the first part of this chapter is to investigate similar possibilities for the case of rigid fibers which are fully coupled to the underlying laminar flow field. Rigid fibers are indeed easier to fabric than elastic ones and are good candidates for novel experimental, non-invasive techniques able to access small-scale, multi-point, properties of fluid flows.

Direct numerical simulations have been performed to solve the incompressible Navier-Stokes equations, with spatially periodic boundary conditions i.e. the so-called ABC and BC flows [52, 53]. The choice of this setting will allow us to perform a direct and reliable comparison between the measured fiber's velocity and the underlying, unperturbed fluid flow velocity. In this framework, a new way for measuring the fluid velocity gradient tensor will be proposed, and tested exploiting the assembly of different fibers (three fibers for the two-dimensional incompressible case and eight fibers for the corresponding three-dimensional case). Accessing the velocity gradients is of particular importance when dealing with turbulent flows, since from their knowledge one can construct the vorticity and the strain-rate tensors, as well as obtain the energy dissipation rate and other key quantities.

The second part of the chapter addresses the issue on whether self-propelled slender object like swimming animals can detect flow signals. Motility of swimming animals and microorganisms is an issue attracting a great deal of attention in different fields of research, covering aspects that range from feeding, reproduction and prey-predator interactions [54], to biological-inspired intelligent navigation [55, 56, 57].

The individual swimming strategies have been the subject of several investigations carried out by means of experimental [58, 59, 60, 61, 62], theoretical, and numerical strategies [63, 64, 65, 66]. A series of contributions analyzed the dynamics of a population of swimming organisms, e.g. in relation to encounter rates and other collective behaviors [67, 68, 69, 70]. Some of them focus on the mutual interactions of microorganisms with the fluid flow environment [71, 72, 73], others on active matter clustering induced by non-homogeneous flows or turbulence [74, 75, 54]. Moreover, scientific evidence clearly show that swimming organisms are able to react to hydrodynamic cues both in laminar and turbulent conditions in order to take different actions [76, 77, 78, 79].

The perception of hydrodynamic signals is an important issue for researchers oriented to the development of bio-inspired mechanosensitive receptors, to promote the advancement of multifunctional sensors in the fields of bio-medical engineering, robotics, and artificial intelligence [80]. Moreover, the combination of the navigation system and biologically-inspired approaches has attracted considerable attention, thus becoming an important research area in the field of intelligent robotic system [81]. Since the emerged trend of bio-metric underwater robots, as an alternative to traditional propeller-driven underwater vehicles, the capability of recognizing and characterizing flow properties through hydrodynamic sensing, makes it possible to take advantage of the flow [82], e.g., by increasing the propulsion efficiency and stability of an underwater robot [83]. In the recent years, efforts have been made for the development of behavioral schemes and bio-inspired sensor for hydrodynamic detection [80, 84, 85, 86], which turn out to be useful in many everyday applications, environmental monitoring, and industrial affairs.

From the point of view of fluid dynamics, self-propelled objects can be classified based on how they set the surrounding fluid during motion. If the induced flow field describes a fluid pushed away along the propulsion axis and dragged in from the sides, the swimmer is named “pusher”. In contrast, when the fluid is pulled inwards towards the swimmer along the propulsion axis and ejected to the sides, it is classified as a “puller”[60].

The main concern of the second part of this chapter is on whether the self-propelled object (i.e. a solid object which may possess inertia and internal elastic degree of freedom) may detect some features of the unperturbed flow field despite its perturbing presence. Such an issue is highly not trivial: even a rigid rod in a fluid flow modifies the unperturbed flow because of the no-slip condition. Pre-existing flow velocity gradients along the rod axis are flattened out owing to the rigidity condition of the rod structure. The perturbation will be even stronger if the rod is self-propelled. Are there features of the flow field very close to the swimmer which remain unperturbed (e.g. as they would be in absence of the swimming object)? Answering this question is one the main concern of the present thesis, with potential interesting applications also in the field of flow measuring techniques via non intrusive Lagrangian techniques (see, e.g., Ref. [4] for the recently proposed ‘fiber tracking velocimetry’).

To answer this question, following the idea of Lushi and Peskin [87], a model for a slender self-propelled object able to accurately reproduce the flow disturbance generated by a pusher or puller swimmer has been built, with the goal of identifying flow properties which remain essentially unchanged despite the invasive presence of the swimmer.

Also for the self-propelled slender object, fully-periodic DNSs have been performed in a time-dependent version of the three-dimensional ABC (Arnold-Beltrami-Childress) flow [88] with high chaoticity uniformly distributed in space for Reynolds numbers up to 10, showing the capability of slender swimmers of sensing hydrodynamic signals net of self-motion.

2.2. Fiber modeling

In this section we will discuss the numerical approach used to model rigid fibers and motile slender objects (slender swimmers) by means of an immersed boundary technique with the aim of measuring flow properties. As far as rigid fibers are concerned, two different approaches will be presented: i) an active model where the fiber is fully coupled to the fluid flow (i.e. a two-way coupling interaction); ii) a passive model (one-way coupling) where the fiber dynamics is affected by the underlying flow but not it does not react back to the flow which can be thus assumed as assigned once and for all. The second part of the section is dedicated to the modeling of swimming fibers, able to reproduce the features of swimming micro-organism. Two different swimmer models are discussed, the 'di-Stokeslet' model and the slender swimmer model, which can behave as pusher or puller. Next, the validation of the swimmer models will be presented.

2.2.1. Rigid fibers

Let us start from the general situation where the considered fiber is a one-dimensional, inertial, elastic and inextensible slender object having length c and diameter d ($d \ll c$). It is characterized by a linear density ρ_1 and bending stiffness γ. Huang et al. [30] is the reference paper for the numerical description of the fiber. In particular, ρ_1 denotes the density difference between the filament and the surrounding fluid. The equation of the fiber motion is expressed in Lagrangian form. Given the position of a material point belonging to the fiber $\mathbf{X} = \mathbf{X}(s, t)$, as a function of the curvilinear coordinate s and time t, the fiber dynamics is governed by the Euler–Bernoulli's beam equation

$$\rho_1 \ddot{\mathbf{X}} = \partial_s(T \partial_s(\mathbf{X})) - \gamma \partial_s^4(\mathbf{X}) - \mathbf{F}. \tag{2.1}$$

Since Eq.(2.1) is one-dimensional in space, the actual filament density is $\rho_1 + \rho_0 A$, where A denotes the sectional area of the filament and ρ_0 the fluid density. In Eq. (2.1), $\mathbf{F}$ denotes the Lagrangian forcing exerted on the filament by the surrounding fluid, while T is the tension necessary to enforce the inextensibility condition

$$\partial_s(\mathbf{X}) \cdot \partial_s(\mathbf{X}) = 1. \tag{2.2}$$

The fiber is freely moving in the flow, hence the corresponding boundary conditions at its ends are:

$$\partial_{ss}\mathbf{X}|_{s=0,c} = \partial_{sss}\mathbf{X}|_{s=0,c} = 0, \tag{2.3}$$

$$T|_{s=0,c} = 0. \tag{2.4}$$

Eq.(2.1) can be rewritten in dimensionless form, where for convenience the dimensionless quantities are written in the same form as their dimensional counterpart

$$\frac{\partial^2 \mathbf{X}}{\partial t^2} = \partial_s \left(T \frac{\partial \mathbf{X}}{\partial s} \right) - \frac{\partial^2}{\partial s^2} \left(\gamma \frac{\partial^2 \mathbf{X}}{\partial s^2} \right) - \mathbf{F}. \tag{2.5}$$

The characteristic scales are: the reference fiber length c for length, the far-field velocity U_0 for velocity, c/U_0 for time, $\rho_1 U_0^2/c$ for the Lagrangian forcing $\mathbf{F}$, $\rho_1 U_0^2$ for the tension force T, and $\rho_1 U_0^2 c^2$ for the bending rigidity γ.

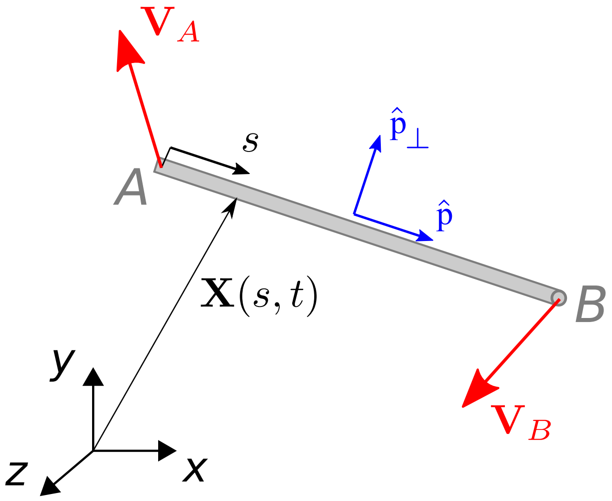

Figure 2.1: Sketch of a generic fiber configuration (the characteristic quantities here indicated are introduced in the text).

The focus in this work is on rigid fibers, sketched in Fig. 2.1. To this end, throughout the work has been choose and retain sufficiently large values of γ for which the fiber has an essentially rigid behavior with negligible deformations. This latter has been checked *a posteriori* in order to be always smaller than $\mathcal{O}(10^{-8})$. The fiber is discretized along s into segments with spatial resolution $\Delta s = c/(N_\mathrm{L} - 1)$, N_L being the number of Lagrangian points.

2.2.2. The fully-coupled model

In order to model the fluid-structure interaction in terms of a two-way coupling, the fiber is fully-coupled to the fluid flow and its dynamics is resolved using an immersed boundary (IB) technique, inspired by the method proposed by Huang et al. [30], for anchored filaments in laminar flows. The method was also exploited for dispersed fibers in turbulent flows [5, 6, 89].

The incompressible Navier–Stokes equations for a Newtonian fluid, which in dimensionless form (see Ref. [30]) are

$$\partial_t \mathbf{u} + \mathbf{u} \cdot \boldsymbol{\partial} \mathbf{u} = -\boldsymbol{\partial} p + \frac{1}{Re} \partial^2 \mathbf{u} + \mathbf{f}^V + \mathbf{f}, \tag{2.6}$$

$$\boldsymbol{\partial} \cdot \mathbf{u} = 0 \tag{2.7}$$

where $\mathbf{u}$ is the fluid velocity, p is the pressure and Re is the Reynolds number. The volume forcing $\mathbf{f}^V$ is used to generate the desired flow field, whose characteristic velocity/length scales are used to define the Reynolds number, Re. $\mathbf{f}$ represents the effect of the immersed boundary, mimicking the presence of the slender body by means of the no-slip enforcement at the Lagrangian points. Accordingly, in the IB method, the Lagrangian forcing $\mathbf{F}$ in Eq. (2.5) is first evaluated on the Lagrangian grid in order to enforce the no-slip condition $\dot{\mathbf{X}} = \mathbf{U}(\mathbf{X}(s,t),t)$. Namely,

$$\mathbf{F}(s,t) = \beta\,(\dot{\mathbf{X}} - \mathbf{U}), \tag{2.8}$$

where β is a problem-dependent large negative constant, and

$$\mathbf{U}(\mathbf{X}(s,t),t) = \int \mathbf{u}(\mathbf{x},t)\delta(\mathbf{x} - \mathbf{X}(s,t))\,\mathrm{d}\mathbf{x} \tag{2.9}$$

is the interpolated fluid velocity on the Lagrangian points. A spreading operation is finally performed around the surrounding Eulerian points, yielding the volume forcing acting on the flow

$$\mathbf{f}(\mathbf{x},t) = \rho \int \mathbf{F}(s,t)\delta(\mathbf{x} - \mathbf{X}(s,t))\,\mathrm{d}s. \tag{2.10}$$

where $\rho = \rho_1/(\rho_0 A)$ comes from non-dimensionalization. Both the interpolation and spreading are performed in terms of a suitable regularized Dirac δ. The one proposed by Roma et al. [90] has been used in the present thesis.

The Direct Numerical Simulations (DNS) has been performed in a cubic domain of size L which is discretized in terms of a uniformly spaced Cartesian grid cells per side. The number of Lagrangian points describing the fiber is chosen in such a way that the Lagrangian spacing Δs is very close to that of the Eularian grid Δx ($\Delta s \approx \Delta x$).

When using this approach, a cubic domain of side $L = 2\pi$ with periodic boundary conditions in all directions has been considered, which is discretized into a uniformly spaced Cartesian grid using $N = 64$ cells per side. The fiber has length $c = 1$ with $N_{\mathrm{L}} = 11$ Lagrangian points. Doubling both resolutions, the variation of results was found to be negligible. The timestep used is $\Delta t = 5 \times 10^{-5}$, after assessing the convergence for this parameter as well.

The flow governing equations are solved numerically using an in-house code. The equations (2.6) and (2.7) are discretized via finite difference, fractional step method on a staggered grid with fully explicit second-order central-differencing scheme in space and third-order Runge-Kutta scheme in time. A fast and efficient FFT-based approach is used to solve the resulting Poisson equation for pressure. The fiber dynamic equations (2.5) is advanced in time with the marching scheme proposed by Huang et al. [30]. Moreover, the code is parallelized via MPI interface. The strategy described above and the code have been implemented and extensively validated to study fiber dynamics in both laminar and turbulent flows in a variety of problems [5, 6, 89, 91, 92, 93].

2.2.3. Passive model

In the second approach, a one-way coupling is assumed, i.e. the fiber is forced by the flow but not vice versa. The problem thus essentially consists in solving only Eq. (2.5), within which the forcing term is expressed as

$$\mathbf{F} = \frac{1}{\tau_s}\,(\dot{\mathbf{X}} - \mathbf{u}(\mathbf{X}(s,t),t)), \tag{2.11}$$

τ_s being the relaxation time of a fiber immersed in viscous flow, i.e. it can be identified with a Stokes time. Overall, it represents a measure of the fiber inertia compared to the flow, and also quantifies the strength of the coupling. In this approach, $\mathbf{u}$ is assigned and does not get modified by the presence of the fiber. Note that this model is similar (apart from the contribution of inertia considered in this model) to that of Young and Shelley [94]; Quennoz et al. [95], relying on local slender body theory, and further simplified assuming an isotropic form for $\mathbf{F}$.

Using this model, the convergence of the solutions have been assessed only with the Lagrangian resolution (since there is not the need of an Eulerian grid in this case) and the computational time step. Given the substantially lower computational demand of this approach compared with the fully-coupled (see Sec. 2.2.2.), for a fiber with length $c = 1$, $N_{\mathrm{L}} = 31$ and $\Delta t = 10^{-6}$ have been used, although a numerically stable and resolution-independent solution was already found with coarser resolution, accordingly with the findings for two-way coupling case.

2.2.4. Swimming fibers

IB realization of the "di-Stokeslet" model

The numerical framework described above in Secs. 2.2.1. and 2.2.2. has been used to build a swimming fiber in order to reproduce an idealized swimmer model with the main features of aquatic swimmer micro-organisms. Here, Eq. (2.5) becomes

$$\frac{\partial^2 \mathbf{X}}{\partial t^2} = \partial_s \left(T \frac{\partial \mathbf{X}}{\partial s} \right) - \frac{\partial^2}{\partial s^2} \left(\gamma \frac{\partial^2 \mathbf{X}}{\partial s^2} \right) - \mathbf{F} - \mathbf{F}_T \tag{2.12}$$

where $\mathbf{F}_T$ is a unit-length forcing, mimicking the propulsion mechanism causing a net motion along the swimmer axis. In plain words,

$$\mathbf{F}_T = k \hat{\mathbf{p}} \tag{2.13}$$

where k is kept constant and controls the propulsion magnitude and $\hat{\mathbf{p}}$ is the unit vector indicating the swimmer orientation. On the self-propelled slender object a constant tangential propulsive force has been imposed.

The simplest swimmer model presented is the "di-Srokeslet", which based on the IB strategy, mimics swimming micro-organisms generating dipolar flow fields [58, 59, 96, 97] characterized by the well-know r^{-2} decay in space of the flow disturbance triggered by the swimmer motion. Depending on the characteristics of the propulsion mechanism, one can have rear-actuated swimmers, i.e., pushers (such as bacteria *E. coli* or *Spermatozoa*), or front-actuated swimmers, i.e., pullers (such as rotifer *Brachionus plicatilis*). For pusher/puller swimmers, the description of the locomotion is made in terms of two oppositely directed point forces of equal magnitude, but acting in different points on the Lagrangian grid, a configuration used to mimic the so-called stresslet (or di-Stokeslet) [96]. Fig. 2.2 reports for the sake of example a pusher swimmer. By looking at Fig. 2.2 one force (blue arrow) acts on the last point of the Lagrangian grid, where both the no-slip condition and the propulsion are imposed, and it is associated with the swimmer body. The second force (red arrow) acts on the fluid (by spreading a point force applied to the first Lagrangian point of the grid). The no-slip condition is not applied on this point and the same is for all remaining points of the Lagrangian grid (grey points). While the first point force mimics the propulsion caused by, e.g., the flagella, the second mimics its pushing effect on the fluid. Although Fig. 2.2 refers to a pusher, the description for a puller proceeds in a very similar way and will be described in the next section.

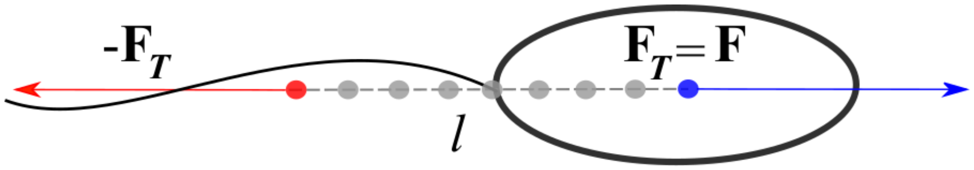

Figure 2.2: Sketch of the realization based on the IB method of a di-Stokelest, modeling a pusher swimmer, such as *Spermatozoa*. The blue arrow indicates the propulsive force on the swimmer (acting along its axis) $\mathbf{F}_T$ used in Eq. 2.12, coinciding with the direction of the motion. The red arrow represents the force exerted by the swimmer flagella to the fluid. The dashed line indicates the separation distance, $l = n\Delta s$, with n being the number of intervals Δs between the two point forces. The grey dots represent the Lagrangian grid points. The no-slip condition and the propulsion force is imposed only on the blue grid point. The inextensibility constraint makes the propulsion force to propagates on the rest of the rigid slender body, causing this latter to swim. By using Eq. (2.10), the spreading of $-\mathbf{F}_T$ is imposed on the red dot. Finally $\mathbf{F}$ denotes the force acting on the fluid due to the friction between the fluid and the immersed body. Note that in the Stokes regime forces acting on the swimmer and on the fluid are both balanced.

A slender swimmer model

The limitation of the di-Stokeslet model is that it condensates all details of a swimming object only in a point (blu dot in Fig. 2.2). The slender swimmer is a generalization that allows to overcome such a limitation. This latter is a less idealized swimmer model able to describe a more elongated organism, which at level of minimal model can be thought as a slender swimmer [55]. By tacking inspiration from Lushi and Peskin [87], the slender swimmer has been build by imposing the no-slip condition and the propulsion force on the same half length, $\ell = c/2$, of the slender motile object, the spreading of the pushing/pulling forcing acting on the fluid being imposed on the other half. One obtains a pusher by imposing the pushing force on the first half edge of the Lagrangian grid, starting from the trailing edge. The second half part of the slender body corresponds to the region where the propulsion is acting on the fluid, as shown in Fig. 2.3 top. A puller is obtained in a similar way but the pulling force is applied on the second half of the Lagrangian grid, as depicted in Fig. 2.3 bottom.

2.2.5. Validation of the swimmer models

The di-Stokeslet model

Let us now start by validating the flow field generated by the IB method sketched in Fig. 2.2. The DNS are performed in a cubic domain of side $L = 4\pi$ and 8π, which is discretized using $N = 128$ and 256 cells per side, respectively. Doubling the resolution, of both the Eulerian and

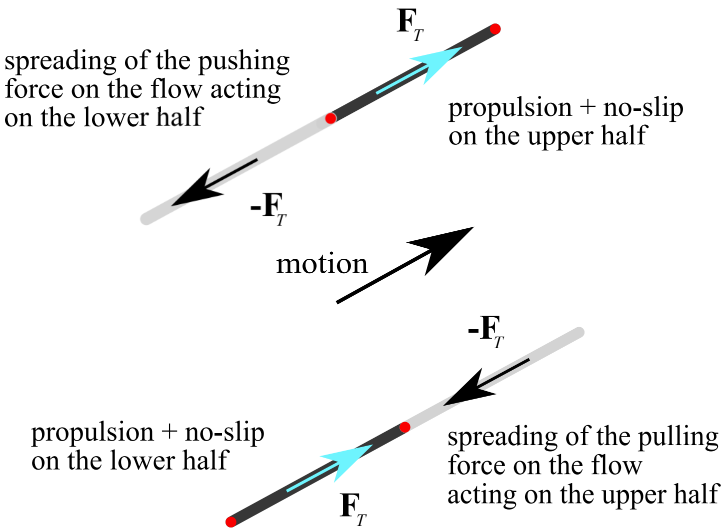

Figure 2.3: Top: sketch of a slender pusher swimmer. The spreading of the pushing force on the fluid is applied to the lower half; the no-slip condition is applied to the upper half. Bottom: sketch of a slender puller swimmer. The spreading of the pulling force is applied to the upper half; the no-slip condition is applied to the lower half. The red dots identify the end-to-end swimmer distance.

Lagrangian grid (in such a way that $\Delta s \approx \Delta x$), gave no substantial variation of the results we are going to show. The same sensitivity analysis has been carried out also for the time step. The numerical solutions have been obtained after a convergence study, ensuring that halving the time step causes relative variations of the resulting flow field smaller than a few percent.

In still fluid, the swimmer is free to evolve from rest until it reaches its terminal velocity, u_s, with a resulting swimmer Reynolds number, $Re_s \ll 1$. After a transient time, also the flow field reaches a steady-state regime characterized by a constant kinetic energy. In what follow, the comparison between the results from the numerical simulations and theory are presented for time instants corresponding to the steady state. Different snapshots taken at different times are identical provided that a translation of the reference system (moving with the swimming velocity u_s) is considered. Here, $Re_s = u_s l/\nu$ is based on the separation distance, l, between the two point forces of Fig. 2.2. To check the resulting flow field, it has been used the well-known solution of the Stokes flow past a sphere for $Re \ll 1$. Written in polar coordinates, its expression reads:

$$\frac{u_r}{u_s} = \left[1 - \frac{3}{2}\frac{R}{r} + \frac{1}{2}\left(\frac{R}{r}\right)^3\right]\cos\theta \tag{2.14a}$$

$$\frac{u_\theta}{u_s} = \left[-1 + \frac{3}{4}\frac{R}{r} + \frac{1}{4}\left(\frac{R}{r}\right)^3\right]\sin\theta \tag{2.14b}$$

where u_r and u_θ are the radial and the transverse velocity components, respectively. $R \approx dx$ is the radius associated to the sphere, according to the regularized Dirac δ-function. To mimic the di-Stokeslet, Eq. (2.14) has been combined with a similar solution for another sphere, separated from the former by a distance l (here $l = 0.6$). The two spheres are associated to

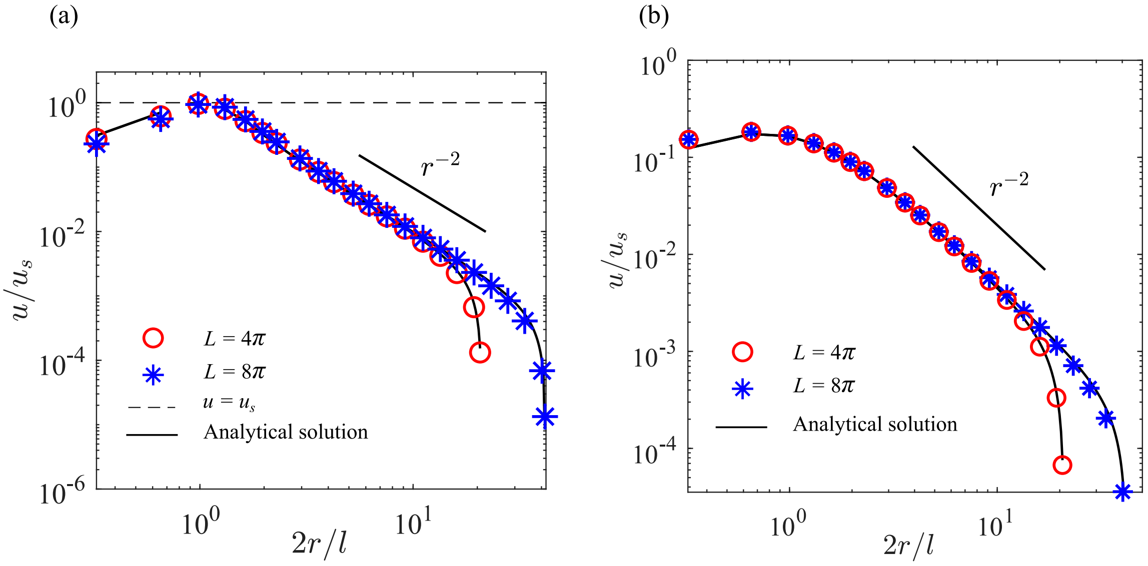

Figure 2.4: Spatial decay of the fluid disturbance caused by a di-Stokeslet swimmer (pusher). The flow velocity magnitude, u, normalized by the swimming velocity, u_s, is plotted against the distance r, normalized by the separation distance l ($Re_s = 0.001$). Red circles represent the solution for a domain of length $L = 4\pi$; blue stars for a domain of length $L = 8\pi$. (a) along the motion direction, the dashed line indicating the swimming velocity u_s. (b) along a direction perpendicular to the motion. Black lines denote the analytical solution from the di-Stokeslet built from Eq. (2.14). The agreement between the numerical results and the theoretical prediction is excellent, also in relation to the r^{-2} decay typical of dipolar flows (continuous straight lines).

two unperturbed flows having opposite directions but possessing the same magnitude u_s. The resulting flow configuration is considered in a periodic domain to match the periodic boundary conditions of the simulations based on the IB strategy.

The comparison between the analytical flow solution and the one obtained from the IB strategy shows an excellent agreement (see Fig. 2.4), while capturing both the near field and the far field fluid flow. Fig. 2.4 shows the decay of the flow field velocity magnitude, u, both along the swimming direction (Fig. 2.4a) and along its normal (Fig. 2.4b). A pusher swimmer is considered in figure, but the same results have been obtained for a puller swimmer (not shown here).

It is possible to see a clear r^{-2} scaling, the fingerprint of a dipolar flow; it is very well reproduced by the numerical simulations, despite the use of the periodic boundary conditions. The latter cause a degradation of the power law behavior which is however limited to the region close to the side of the periodicity box. As shown in Fig. 2.4, the effect of the periodicity can be moved away from the swimmer by simply increasing the size of the periodicity box. Its effect on the near-field behavior turns out to be negligible with a box size of 4π, where a clear r^{-2} decay (see Fig. 2.4) can be detected. Accordingly, 4π has been fixed as size of the periodicity box for the analysis reported in the following.

The slender swimmer model

Also in this case the swimmer is free to reach its terminal velocity u_s starting from rest. In this case, $Re_s = u_s\ell/\nu$ is based on the length of the slender swimmer, ℓ (here $\ell = 0.4$). The resulting flow field is compared with the solution for an extended stresslet [96], where the velocity field in a point $\mathbf{r}$ is reconstructed by superimposing several (here 5) di-Stokeslet solutions. Namely,

$$\mathbf{u}(\mathbf{r}) = \frac{|\mathbf{F}_T|}{8\pi\mu} \sum_{i=1}^{5} \left[\mathbf{S}\left(\mathbf{r} - \frac{i\Delta s}{2}\hat{\mathbf{p}}\right) - \mathbf{S}\left(\mathbf{r} + \frac{i\Delta s}{2}\hat{\mathbf{p}}\right)\right] \hat{\mathbf{p}} + \ldots \tag{2.15}$$

where dots stay for contributions coming from all other boxes when the effect of periodicity is explicitly accounted for. In Eq (2.15), μ is the dynamic viscosity, $\mathbf{F}_T$ is the propulsive force (per unit length) used in the IB method and

$$\mathbf{S}(\mathbf{r}) = \frac{1}{r}(\mathbf{I} + \hat{\mathbf{r}} \otimes \hat{\mathbf{r}}) \tag{2.16}$$

is the bulk Stokeslet, with $\mathbf{I}$ the identity matrix, $r \equiv |\mathbf{r}|$, $\hat{\mathbf{r}} \equiv \mathbf{r}/r$, and $\otimes$ the tensorial product.

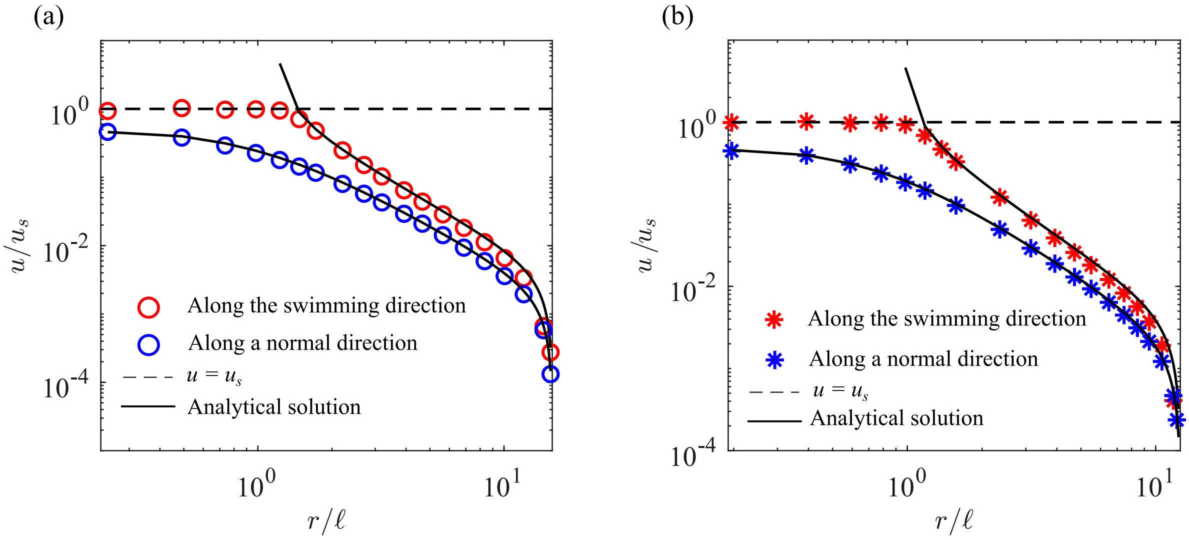

Figure 2.5: Spatial decay of the fluid disturbance due to the presence of a slender pusher swimmer, circles (a), and a slender puller swimmer, stars (b), in a domain with size $L = 4\pi$. The numerical data are complemented by a superposition of the di-Stokeslet (black lines, Eq. (2.15)). The flow velocity, u, normalized by the swimming velocity u_s, is plotted against the distance r normalized by the swimmer length, ℓ. Red markers: along the motion direction; blue markers: along a direction perpendicular to the motion. The dashed line indicates the terminal velocity, u_s, reached by the swimmer ($Re_s = 0.0002$). Also in the present case, an excellent agreement between numerical results and theory can be detected.

In Fig. 2.5 the flow behavior due to slender pusher/puller swimmer are reported, along the motion direction, and along the direction perpendicular to it. Both pushers and pullers accurately capture the decay of the flow velocity with respect to r. Moreover, it has been also verified that the model captures the fluid flow generated by a swimmer from a more qualitative point of view. In Fig. 2.6 a pusher and a puller swimmer, together with the flow field they generate due to their locomotion, are shown. The model accurately captures the flow field that a swimmer generates by its locomotion, as also observed in experiments [59].

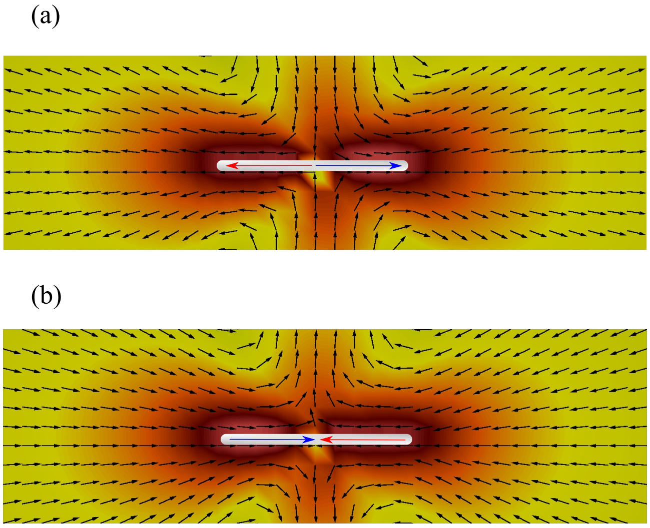

Figure 2.6: IB-method-based simulations of the flow field generated by a pusher swimmer (a) and by a puller swimmer (b). In both panels, the blue arrow indicates the propulsive force acting on the swimmer and the motion direction; the red arrow indicates the action of the pushing (top panel) and pulling (bottom panel) forces.

2.3. The rotational Stokes Number

The first step of our analysis is to characterized the slender body inertia via a rotational Stokes number St, which is the most suitable quantity when dealing with flow observables related to transverse velocity differences as those considered in this work. To this end, the steady two-dimensional Beltrami-Childress (BC) cellular flow [53, 52, 98] has been considered, which is described by:

$$\begin{aligned} u &= \cos y \\ v &= \cos x \end{aligned} \tag{2.17}$$

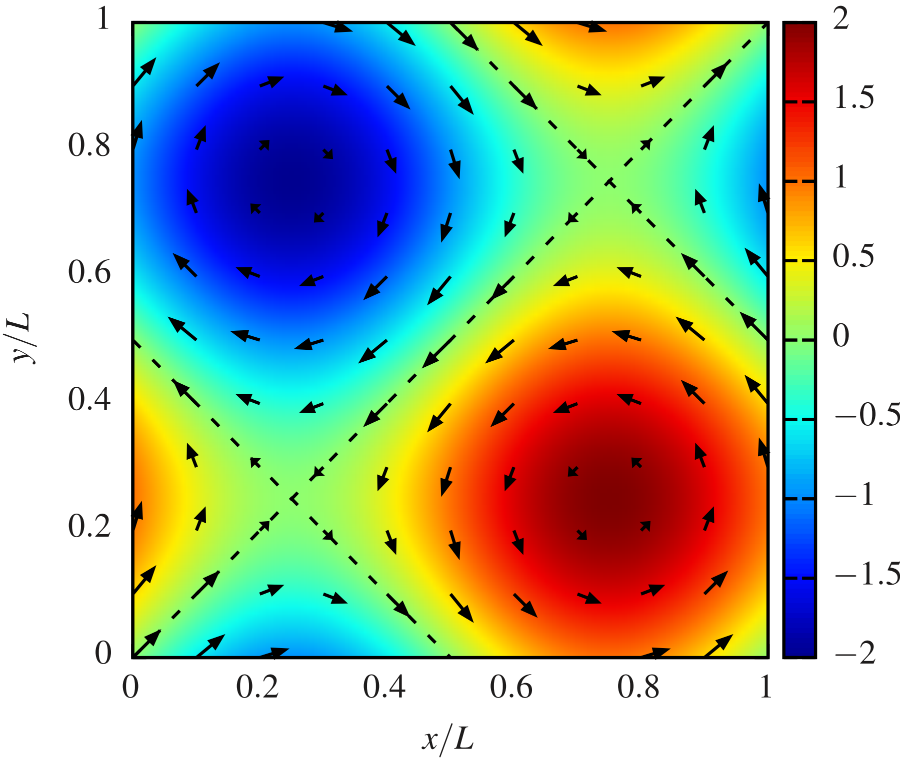

Figure 2.7: The so-called *BC* cellular flow (the colormap showing the stream function given by $\Psi(x, y) = \sin(y) - \sin(x)$ along with the corresponding velocity vectors).

To obtain the BC flow (see Fig. 2.7) as a stable solution of the Navier-Stokes equations a volume force $\mathbf{f}^V = (1/Re)\mathbf{u}$ has been applied to the right hand side of Eq. (2.6) for Re up to 10 (see Ref. [52]). To evaluate the Stokes time, the slender object, without propulsion (i.e. $\mathbf{F}_T = 0$) , and initially at rest, is placed at the center of one cell in the BC flow (see Fig. 2.7). Under the action of the flow, the slender object starts to rotate (fully coupled to the flow) around its center of mass. We measure the time it takes for the slender object peripheral velocity, $V(t)$, to adapt to the corresponding flow velocity V_0. Measurements have done in terms of exponential fits:

$$V(t) = V_0 \left(1 - e^{-t/\tau_s}\right) \tag{2.18}$$

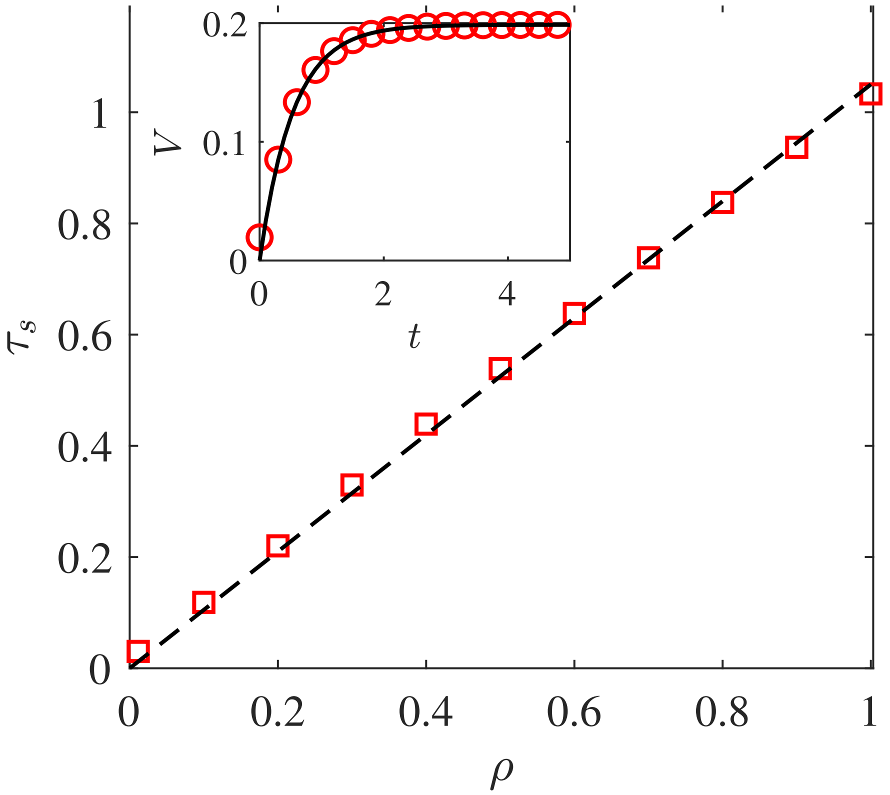

Figure 2.8: Rotational Stokes time as a function of the dimensionless swimmer linear density. Here $Re = 1$. Red squares: measured value; black dashed line: linear fit. Inset: time history of the velocity magnitude of one swimmer end (red circles) fitted using Eq. (2.18) (black line), for a swimmer with $\rho = 0.5$.

from which the Stokes time, τ_s, has been extracted. This operation has been made both for fibers and slender swimmers. Fig. 2.8 report the results for slender swimmers. The same evidence is obtained for fibers. In the inset of Fig. 2.8, an example of this procedure is provided. The resulting behavior of τ_s as a function of ρ, is reported in Fig. 2.8, showing that it can be well described by a linear law. Since τ_s depends also on the length of the slender object, as well as on its mass, the linear fit $\tau_s = a\rho$ gives different results: for fibers having a length $c = 1$, $a \approx 0.04$, while for swimmers having a length $\ell = 0.4$, $a \approx 1$ for $Re = 1$. Because of our interest in investigating the swimming behavior for larger Re, the same analysis has been performed in a fluid with $Re = 10$. Also in this case it has been found that a linear relationship between τ_s and ρ holds, with $a \approx 10$ (not shown). The increase in a by a factor 10 is reasonable because of the expected inverse proportionality between the Stokes time and the viscosity, which has been reduced to obtain the desired Reynolds number. The Stokes number is defined as $St = \tau_s/\tau_f$, where for fibers $\tau_f = c/U_0$ is the characteristic hydrodynamic timescale. The definition of St for the slender swimmers will be introduced in Sec. 2.4.4..

This has been done for the sole fibers modeled with the active model, since the Stokes number is an assigned parameter in the one-way coupling case, as shown by Eq. (2.11).

2.4. Measuring flow properties

The capability of a rigid fiber, or slender swimmer, to act as a proxy of a laminar, cellular flow in terms of a few fiber properties, such as its position and the velocity of the fiber/swimmer end points will be discussed. The measures have been performed in 2-D and 3-D laminar flows such as the BC flow, already introduced in Sec. 2.3., the ABC flow [52], a time-dependent and two-dimensional flow and a time-dependent version of the three dimensional ABC (Arnold–Beltrami-Childress) flow [88].

The choice of this setting allows us to perform a direct and reliable comparison between the measured fiber/swimmer velocity and the underlying unperturbed fluid flow velocity.

2.4.1. Normal derivative of longitudinal velocity component

Let us start by investigating the possibility to measure flow properties by means of rigid fibers fully-coupled to the flow. Here, the 2-D BC flow with $Re = 1$ has been employed. Fig. 2.9 reports the velocity magnitude of one fiber end as a function of time, compared to the velocity magnitude of the unperturbed flow (i.e., in the absence of the fiber) evaluated at the same point. It is evident that the two quantities differ appreciably. This result indicates that a fiber cannot be used to measure single-point flow quantities as done, e.g., in PIV techniques using tracer particles [48].

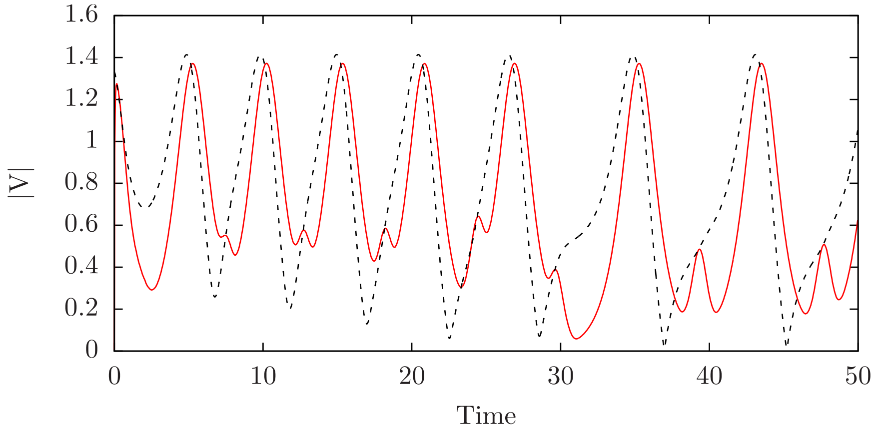

Figure 2.9: Velocity time series at one fiber end for the fiber (red solid line) and for the underlying unperturbed flow (black dashed line), for a fiber with $St \approx 0.01$ released into the BC flow, computed with the active model.

Now, let us consider the velocity difference between the fiber end points (Fig. 2.1), i.e. $\delta \mathbf{V} = \mathbf{V}_B - \mathbf{V}_A$, and denote by $\delta \mathbf{u} = \mathbf{u}|_B - \mathbf{u}|_A$ the corresponding unperturbed flow velocity difference. Comparing directly these two quantities, however, would still yield the same mismatch previously found for the velocity of one end. Such a mismatch is due not only to the fiber inertia, but also to the fiber inextensibility constraint. Indeed, if we consider the projection of the velocity difference introduced above along the direction parallel to the end-to-end distance, $\hat{\mathbf{p}}$, for a rigid and inextensible object, such quantity is always zero, although the same quantity for the underlying unperturbed flow is clearly not. The idea is then to project $\delta \mathbf{V}$ on a plane normal to $\hat{\mathbf{p}}$ by simply arguing that along that direction the effect of the inextensibility constraint should be washed out. In terms of the normal unit vector $\hat{\mathbf{p}}_\perp$ (shown in figure 2.1), we define the projections:

$$\delta V_\perp = \delta \mathbf{V} \cdot \hat{\mathbf{p}}_\perp, \tag{2.19}$$

$$\delta u_\perp = \delta \mathbf{u} \cdot \hat{\mathbf{p}}_\perp. \tag{2.20}$$

The projected quantities (2.19) and (2.20) are compared in Fig. 2.10 where we report the results of the analysis in the BC flow configuration while varying St, for both two-way and one-way approaches. For relatively low St (i.e., the first two rows of the figure), it is possible to notice a remarkable agreement, i.e. the fiber is able to accurately measure the (unperturbed) flow transverse velocity increments in terms of its transverse velocity increments. For increasing St, i.e. the fiber inertia, the agreement gets worse, as expected. Overall, we observe a close resemblance between results for fibers starting from the same position, using the active (left panels) and passive (right panels) model, especially for the smallest St. This suggests that here the effective coupling between the flow and the fiber could be actually neglected, in relation to the measurement of transverse velocity differences. Accordingly, when extending the analysis to three-dimensional and unsteady flows (Sec. 2.4.2.) it will exclusively employ the passive model on the basis of such evidence. Note however that from Fig. 2.10 it is evident that the role of feedback cannot be entirely neglected. For sufficiently large Stokes numbers ($St \approx 0.1$), the curves on the left panels and those on the right ones are different, revealing that the motion of the fiber center of mass is affected by the feedback of the fiber to the flow. The effect of the latter is indeed crucial when the fiber center of mass moves close to the flow separatrix, potentially causing totally different trajectories compared to the one-way approach.

Some further comments are worth considering. First, the projection along the normal direction to the fiber is crucial for the fiber to be a proxy of the flow velocity differences: if we project the velocity differences along a generic direction, the agreement shown before is no longer present (not shown here). In the two-dimensional case, the normal direction is uniquely defined by $\hat{\mathbf{p}}_\perp = \pm(\hat{p}_2, -\hat{p}_1, 0)$. In the three-dimensional case there are instead an infinite number of directions belonging to the normal plane to the fiber orientation. It has been retained $\hat{\mathbf{p}}_\perp = (\hat{p}_2, -\hat{p}_1, 0)$, also for 3-D cases (see Sec. 2.4.2.) even if the results did not change for different choices of $\hat{\mathbf{p}}_\perp$ we have considered.

The situation considered in Fig. 2.10 refers to a fiber whose length is about 32% the size of the single cell. This is a case where the fiber length is sufficiently small compared to the variation scale of the flow. Under such condition the velocity difference between the free ends can be compared with the flow gradient evaluated at the fiber center of mass. For the latter, the same projection along $\hat{\mathbf{p}}_\perp$ has to be applied as before. However, due to the tensorial structure of the gradient $\partial_j u_i$, this translates to considering a double projection, first along the tangential and then along the normal direction:

$$D = \partial_j u_i \hat{p}_j \hat{p}_i^\perp. \tag{2.21}$$

In Fig. 2.10, where $c/L = (2\pi)^{-1}$, the curve representing D is not reported but would be essentially superimposed to that of the fluid velocity difference. Doubling the fiber length, i.e.

$c/L = \pi^{-1}$, the accuracy gets worse as expected. This simply means that, despite the fact that the fiber accurately measures the transverse velocity differences across the fiber ends, the fiber is too long to allow the derivative to be well approximated by the ratio of the increments.

Finally, another aspect to be considered is the tendency of inertial particles to sample preferential zones of the flow, giving rise to peculiar features such as small-scale clustering of dilute suspensions. This phenomenon is well-known and has been thoroughly investigated for spherical particles in turbulent flows (see, e.g., Refs. [99, 100, 101]) and has also been observed for anisotropic particles (see Ref. [1] and references therein). While this mechanism could impact on the potential of using fibers as a proxy of the flow (i.e., measuring only certain regions of space), by decreasing the Stokes number, along with improving the measure in itself, assures at the same time that preferential sampling is reduced. In steady cellular flows, it is possible to observe the role of inertia in this regard by looking at the fiber trajectories and, in particular, their deviation from the flow streamlines. A visualization from the data is given in Fig. 2.11 where two cases at different St are compered: the less inertial fiber with $St = 0.1$ initially follows the cell streamlines but, due to the centrifugal effect, eventually reaches the flow separation lines (Fig. 2.11a), while the heavier fiber with $St = 2$ shows a stronger deviation of its trajectory from the streamlines, resulting in a more diffusive behavior (Fig. 2.11b).

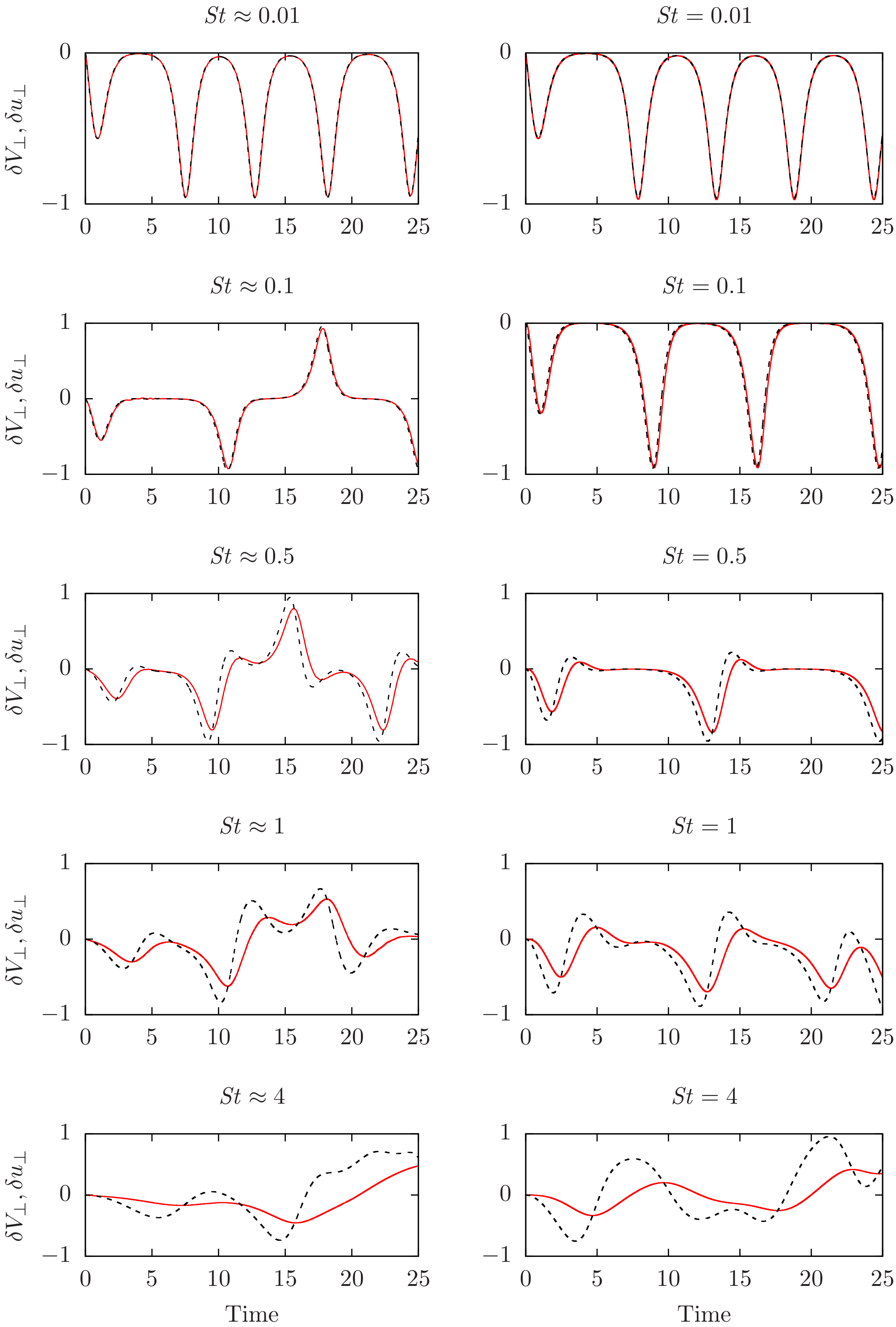

Figure 2.10: Transverse velocity differences of fiber $\delta V_\perp$ (solid line) and unperturbed BC flow $\delta u_\perp$ (dashed line) for different Stokes number, both for the two-way (left panels) and one-way (right panels) coupling. The normalized root-mean-square deviation between $\delta V_\perp$ and $\delta u_\perp$, for both active and passive model, is less than 1% for $St \leq 0.1$, of the order of 10% for $St \approx 0.5$ and larger than 15% for $St \geq 1$. The fiber length is unity and it is thus about 32% of the size of the single cell in the considered flow.

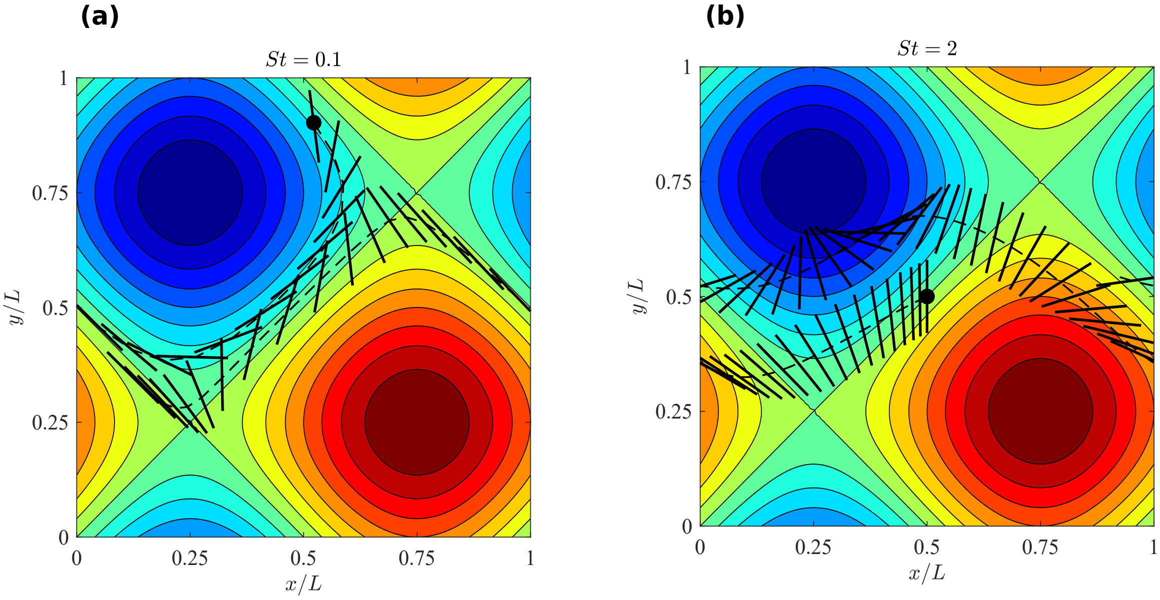

Figure 2.11: Superposition of fiber positions at different instants within the periodic two-dimensional BC flow (the colormap denoting the stream function), computed with the active model. (a) $St = 0.1$ and (b) $St = 2$. The dashed line represents the trajectory of fiber center of mass and the black circle indicates its starting position.

2.4.2. Extension to three-dimensional and unsteady flows

As further step of our analysis, let us test the capability of the fiber to measure the transverse velocity differences in three-dimensional steady or unsteady cellular flows. In light of the findings for the steady BC flow (Sec. 2.4.1.), only results obtained with the passive model will be presented, although checks using the active model have been performed and yield the same overall scenario as in the steady, two-dimensional case.

First, let us consider the so-called Arnold-Beltrami-Childress (ABC) flow, which is known to be a time-independent, three-dimensional solution of Euler's equations [52]:

$$\begin{aligned} u &= \sin z + \cos y \\ v &= \sin x + \cos z \\ w &= \sin y + \cos x \end{aligned} \tag{2.22}$$

Also in this case the same kind of volume force introduced in Sec. 2.3. has been used to obtain a stable solution of the Navier-Stokes equation, for $Re = 1$. In Fig. 2.12 (left panels) the results of the analysis for this 3-D case are presented. As for the BC flow, it has been found that for sufficiently low Stokes numbers, i.e. $St \leq 0.1$, the agreement is evident between the fluid and fiber transverse velocity differences. Like the 2-D case the agreement deteriorates for increasing St as expected.

Next, the results are presented for the unsteady, time-periodic, and two-dimensional flow (Eq. (2.23)).

$$\begin{aligned} u &= \sin[x + \epsilon_1 \sin(\omega_1 t)] \cos[y + \epsilon_2 \sin(\omega_2 t)] \\ v &= -\cos[x + \epsilon_1 \sin(\omega_1 t)] \sin[y + \epsilon_2 sin(\omega_2 t)] \end{aligned} \tag{2.23}$$

where $\epsilon_1 = \epsilon_2 = 0.2L$ are the amplitudes while $\omega_1 = 2\pi$ and $\omega_2 = 1$ are the frequencies of the oscillation along x and y, respectively. This choice corresponds to a situation where the Lagrangian trajectories of fluid particles are chaotic [102, 103]. The projected velocity differences are shown in Fig. 2.12 (right panels), where the same conclusions drawn for steady configurations are confirmed: the agreement between the fiber-based measurement and the direct evaluation using the flow expression (Eq. (2.23)) increases by decreasing the rotational Stokes number.

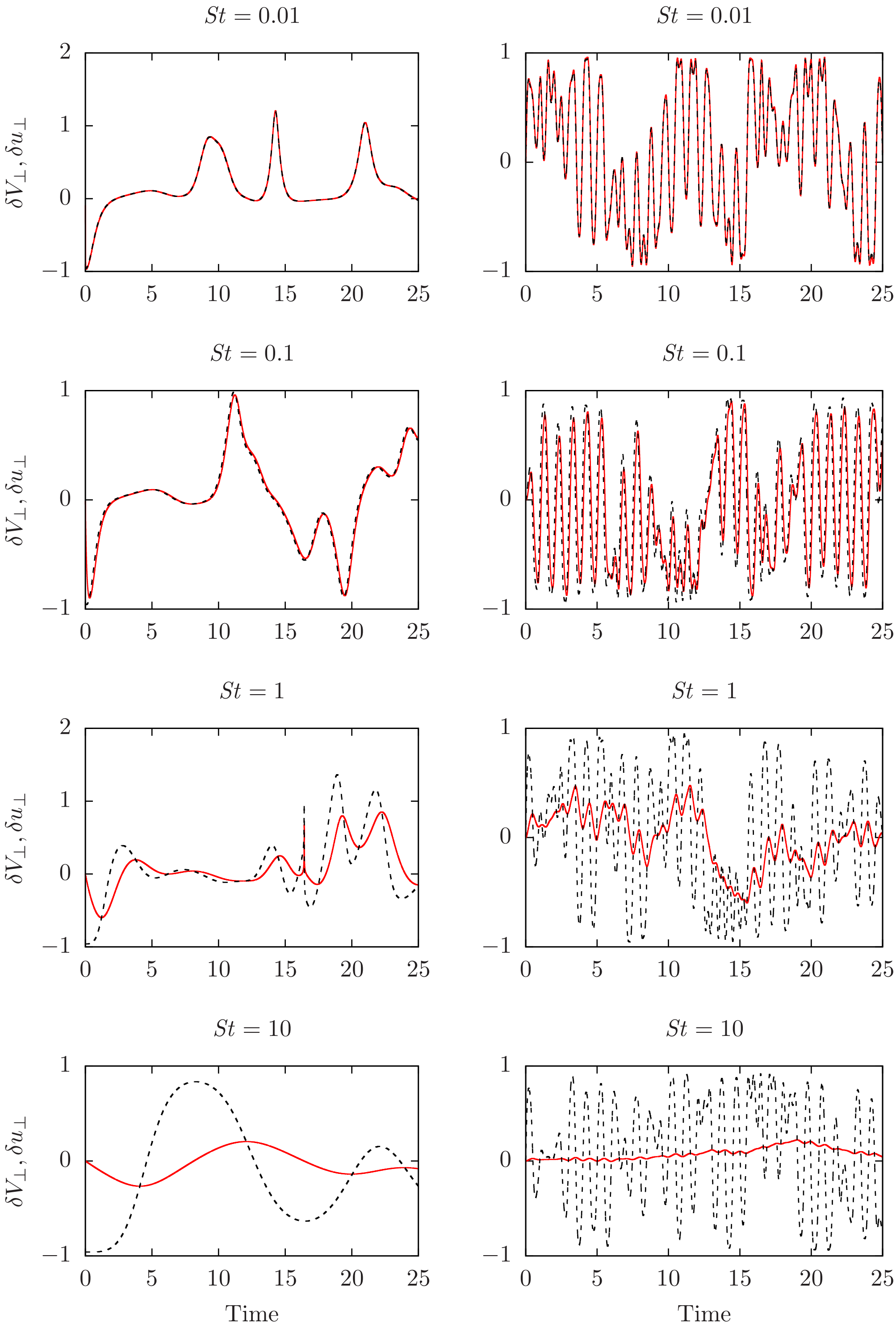

Figure 2.12: Transverse velocity differences of fiber $\delta V_\perp$ (solid line) and unperturbed flow $\delta u_\perp$ (dashed line) for different Stokes numbers, computed using the passive model. Left panels: ABC flow (Eq. 2.22); right panels: 2-D oscillating cellular flow (Eq. 2.23. The normalized root-mean-square deviation between $\delta V_\perp$ and $\delta u_\perp$, for both ABC flow and 2-D oscillating flow, is less than 1% for $St \leq 0.1$, of the order of 15% for $St = 1$ and larger than 20% for $St = 10$.

2.4.3. Evaluation of the velocity gradient tensor

Having characterized the behavior of single fibers, it is possible to move further, focusing on how to access the full velocity gradient tensor $\partial_j u_i$ and not only its normal projection. This will be achieved by assembling several fibers in a proper way and exploiting the following idea: for each fiber, Eq. (2.21) holds, where the velocity gradient becomes the unknown variable if $\delta V_\perp$ is used (that is measured by tracking the fiber trajectory) in place of D. Considering an assembly made by N_f fibers, it corresponds to having a system of N_f equations, from which the gradient can be obtained.

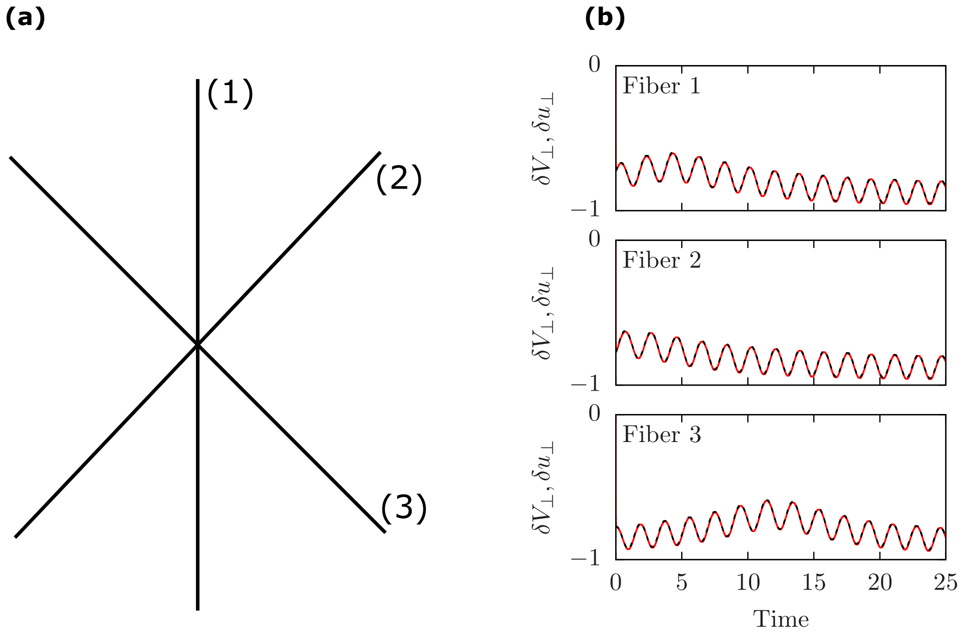

Figure 2.13: (a) Sketch of fiber assembly; (b) transverse velocity differences of each fiber $\delta V_\perp$ (solid line) and underlying unperturbed flow $\delta u_\perp$ (dashed line) in the case of BC flow with $c = 1$ and $St \approx 0.01$, computed using the active model.

Let us therefore estimate the number of fibers that are needed in the two-dimensional case: here $\partial_j u_i$ is made by 2×2 elements; however, the number of independent quantities is reduced of one by exploiting incompressibility. Hence, the assembly has to be made by $N_\mathrm{f} = 3$ fibers, yielding the following system to solve:

$$\begin{aligned} \delta V_\perp^{(1)} &= \partial_j u_i \hat{p}_j^{(1)} \hat{p}_i^{\perp(1)} \\ \delta V_\perp^{(2)} &= \partial_j u_i \hat{p}_j^{(2)} \hat{p}_i^{\perp(2)} \\ \delta V_\perp^{(3)} &= \partial_j u_i \hat{p}_j^{(3)} \hat{p}_i^{\perp(3)} \end{aligned} \tag{2.24}$$

In this system the final number of unknowns are three (i.e. three components of $\partial_j u_i$ out of four because of the incompressibility condition). In a 3-D case the assembly should be made by $N_\mathrm{f} = 8$ fibers, since $\partial_j u_i$ is made by 3×3 elements. Both the left-hand side of the equations and the coefficients of the velocity derivative tensor are easily measurable at each time step along the fiber trajectories and thus known from the numerical experiments. The system can be thus easily solved at each time step while following the fiber along its trajectory.

The three fibers will be connected at their centroids (numerically, it is convenient to realize these connections using springs with sufficiently high stiffness so that the distance between centroids results negligible). However, each fiber is left to behave as in the single case, its dynamics not being substantially altered by the link with the others. To this end, it is crucial to avoid any rotational constraint, so that fibers are able to rotate freely with respect to each other. For the assembly the rotational Stokes number has been measured following the same procedure described in Sec. 2.3. for the single fiber. The resulting relaxation times of each fiber composing the assembly turned out to be the same as the rotational Stokes time of the single isolated fiber. One can thus conclude that the Stokes time of the assembly is the same of a single fiber.

The outlined concept is tested in the steady BC flow already used in Sec. 2.4.1.. As a first step, we looked at the resulting time histories of the projected velocity difference for each fiber composing the assembly (Fig. 2.13b), recovering the same evidences found in the case of single fibers. This provides a clue that also in this configuration it is possible to capture the features of the fluid flow. Indeed, by proceeding to combine the information from all fibers, i.e. by solving the equations system (2.24), finally the velocity gradient tensor is obtained, as shown in Fig. 2.14, where the time series of each element $\partial_j u_i$ is reported, both for the Lagrangian fiber tracking and for the corresponding analytical value of the unperturbed flow. The comparison between the two quantities yields good agreement, with differences that are ascribed to numerical resolution and the finite inertia of fibers.

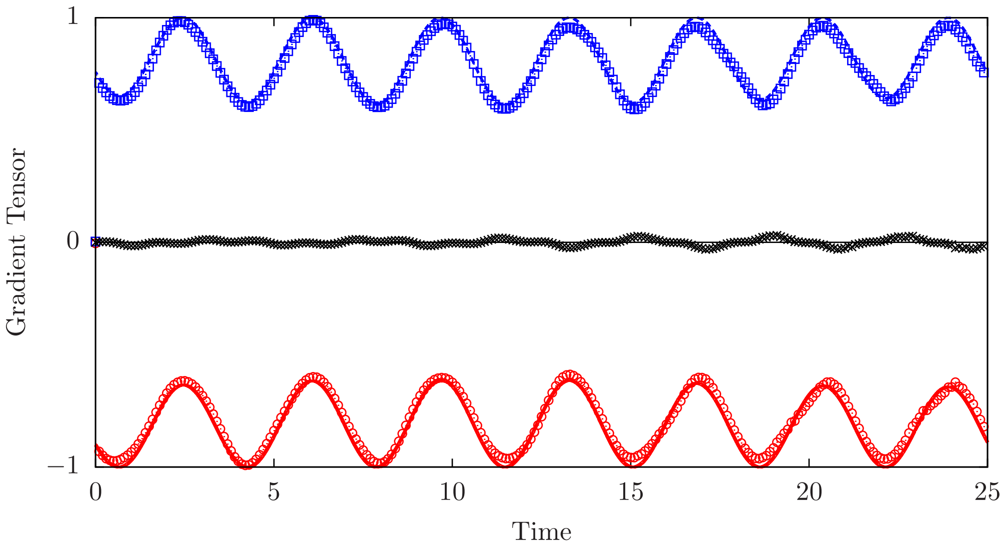

Figure 2.14: Velocity gradient tensor components in the BC flow (Eq. (2.17)) reconstructed by tracking the fiber assembly with $St \approx 0.01$, using the two-way coupling. Red circles: $\partial_y u$ obtained by the fiber Lagrangian tracking; red solid line: $\partial_y u$ for the unperturbed flow; blue squares: $\partial_x v$ obtained by the fiber Lagrangian tracking; blue dashed line $\partial_x v$ for the unperturbed flow; black crosses: $\partial_x u = -\partial_y v$ obtained by the fiber Lagrangian tracking; black line: $\partial_x u = -\partial_y v = 0$ for the unperturbed flow. The normalized root-mean-square error between the components of the gradient tensor reconstructed by the Lagrangian tracking and those of the unperturbed flow is of the order of 1%.

The reported results are obtained using the two-way approach but closely similar results are obtained using the passive model. In Fig. 2.15 the results for the assembly of fibers are shown in the static BC flow using the one-way approach, highlighting essentially the same behavior obtained in the active case (note that the same initial condition for the assembly of fibers was used in both cases). Finally, the analysis has been complemented by employing an assembly of fibers, using the one-way coupling, in the oscillating two dimensional flow introduced in Sec. 2.4.2. (Eq. (2.23)). Results are shown in Fig. 2.16 from which the same conclusions as before are confirmed.

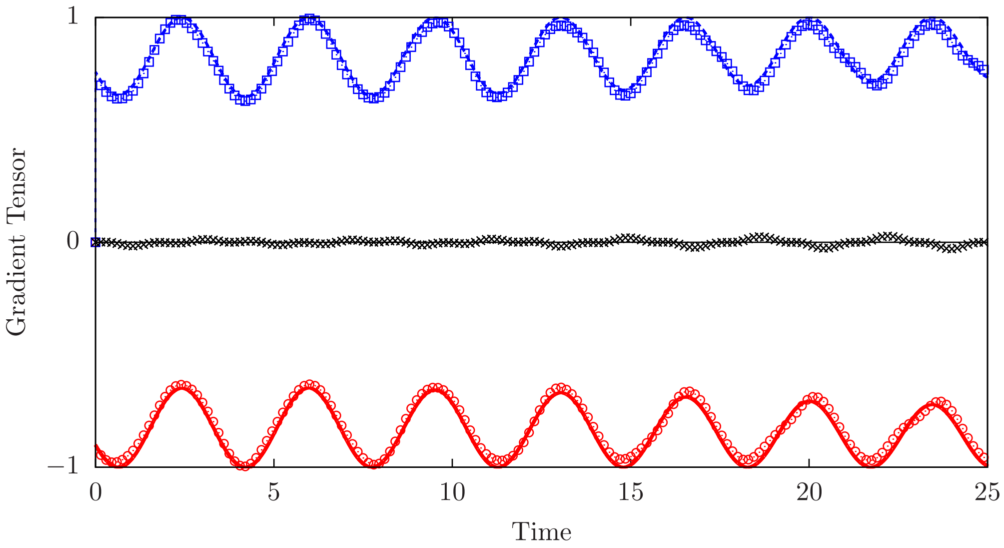

Figure 2.15: As in Fig. 2.14 but for assembly of fibers modeled with one way coupling. The normalized root-mean-square error between the components of the gradient tensor reconstructed by the Lagrangian tracking and those of the unperturbed flow is of the order of 1%.

It is worth noting that the linear system (Eq. 2.24) that has been numerically solved to obtain all components of the flow gradient can become overdetermined because of the alignment of two of more fibers. To avoid this problem a simple recipe has been found; by imposing a small displacement (of Δs, the size of the Lagrangian mesh) between the centroids of the fibers of the assembly (instead of imposing them to be zero) is enough to prevent perfect alignment of the fibers, thus preventing the breakdown of the solution. The results reported in Fig. 2.14, 2.15 and 2.16 have been obtained exploiting this simple, but effective, strategy. Fig. 2.17 reports the time history of the angle of the three fibers composing the assembly, in the oscillating two dimensional flow. As shown in figure, in the considered time frame the alignment between the fibers does not occur and the minimum value of the standard deviation between the three angles is 0.18 rad. Extending the time frame (not shown), up to 25, the minimum value of the standard deviation we measured was 0.0085 rad which was however large enough to allow an accurate solution of the system.

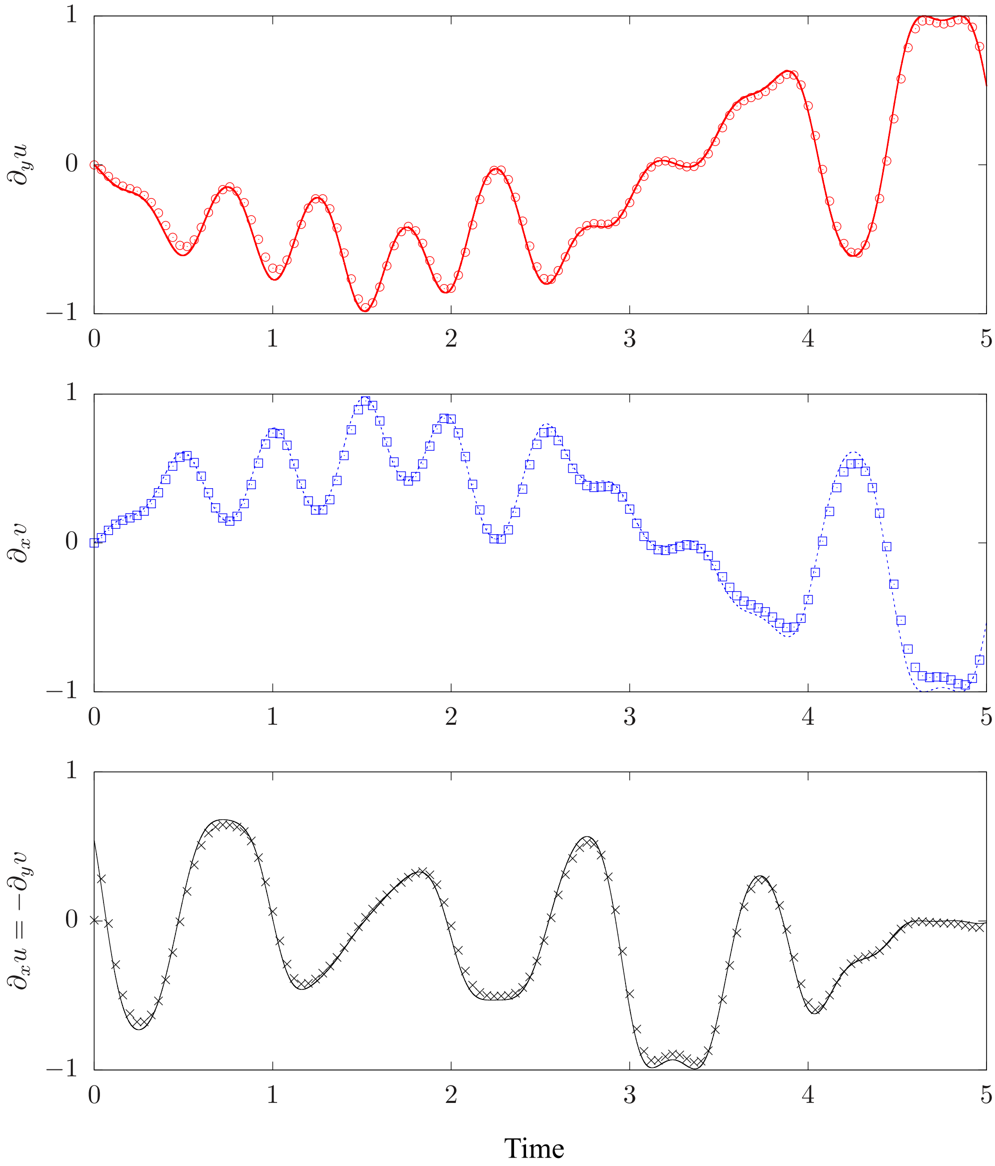

Figure 2.16: As in Fig. 2.15 but for the oscillating two dimensional flow (Eq. 2.23) (the figure is split into three panels for a better readability of the gradient tensor components). The normalized root-mean-square error between the components of the gradient tensor reconstructed by the Lagrangian tracking and those of the unperturbed flow is of the order of 1%.

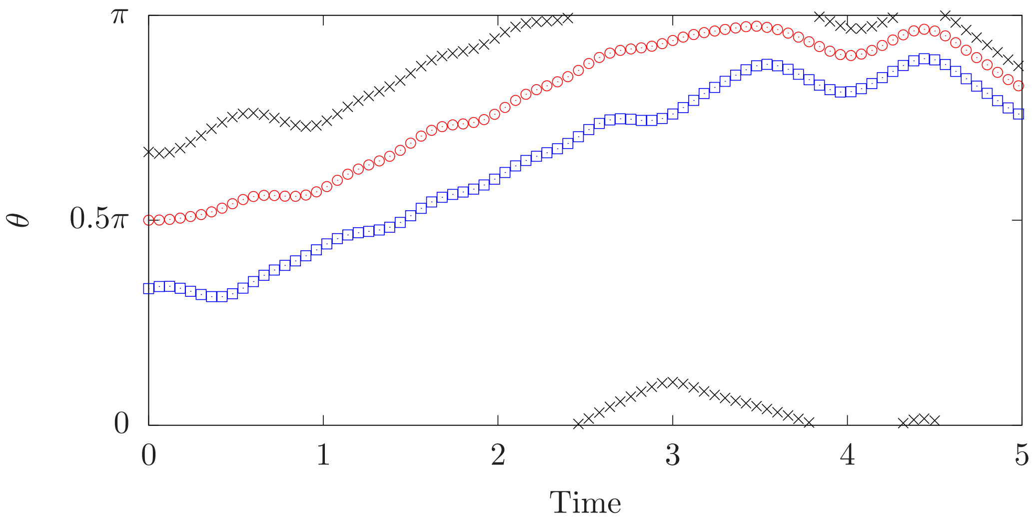

Figure 2.17: Time history of the angles (rad) of the three fibers composing the assembly in the two dimensional oscillating flow. Red circles: fiber 1; blue squares: fiber 2; black crosses: fiber 3. Angles are measured with respect to the horizontal direction. The minimum value of the standard deviation is 0.18.

2.4.4. Sensing velocity differences while swimming

Let us now pass to show the capability of a slender swimmer to measure flow properties in terms of swimmer position and velocity of the swimmer end points (red dots in Fig. 2.3) despite its pertubing presence. Before to pass to discuss how slender motile objects perceive hydrodynamic signals net of self-motion, it is necessary to asses its own swimming velocity given the propulsion $\mathbf{F}_T$ in Eq. (2.12).

Swimming velocity of pushers and pullers

Depending on swimmer type, i.e. pusher or puller, the swimming terminal velocity could be different because different flow disturbance are generated while swimming. When $Re_s \ll 1$, the swimming terminal velocity is given by the balance between the propulsive force and the Stokes drag exerted by the surrounding flow, as it has been shown in section 2.2.5. Here the resulting swimming velocities for the pusher and puller swimmers for different values of Re_s and $\mathbf{F}_T$ are presented.

The behavior of $\mathbf{F}_T$ versus the swimming velocity, u_s, and the corresponding Reynolds number, Re_s, for pushers and pullers, are shown in Fig. 2.18; u_s is normalized with the maximum swimming velocity investigated, while $\mathbf{F}_T$ with the expression from the slender body theory, $\mathbf{F}_{sl} = u_s 4\pi\mu h\eta$, where $h = \ell/2$ is the half length of the slender object, and $\eta = 1/\ln\alpha$, with $\alpha = h/R$ being the aspect ratio [104].

Velocities reached by pusher and puller swimmers in a fluid initially at rest with $Re = 1$, for $0.04 \le Re_s \le 0.4$, are reported in Fig. 2.18a. Fig. 2.18b reports the same quantities for $Re = 10$ (and $0.4 \le Re_s \le 4$). Considering fluids with different Re, allows us to investigate differences in locomotion of pushers and pullers when inertia becomes important.

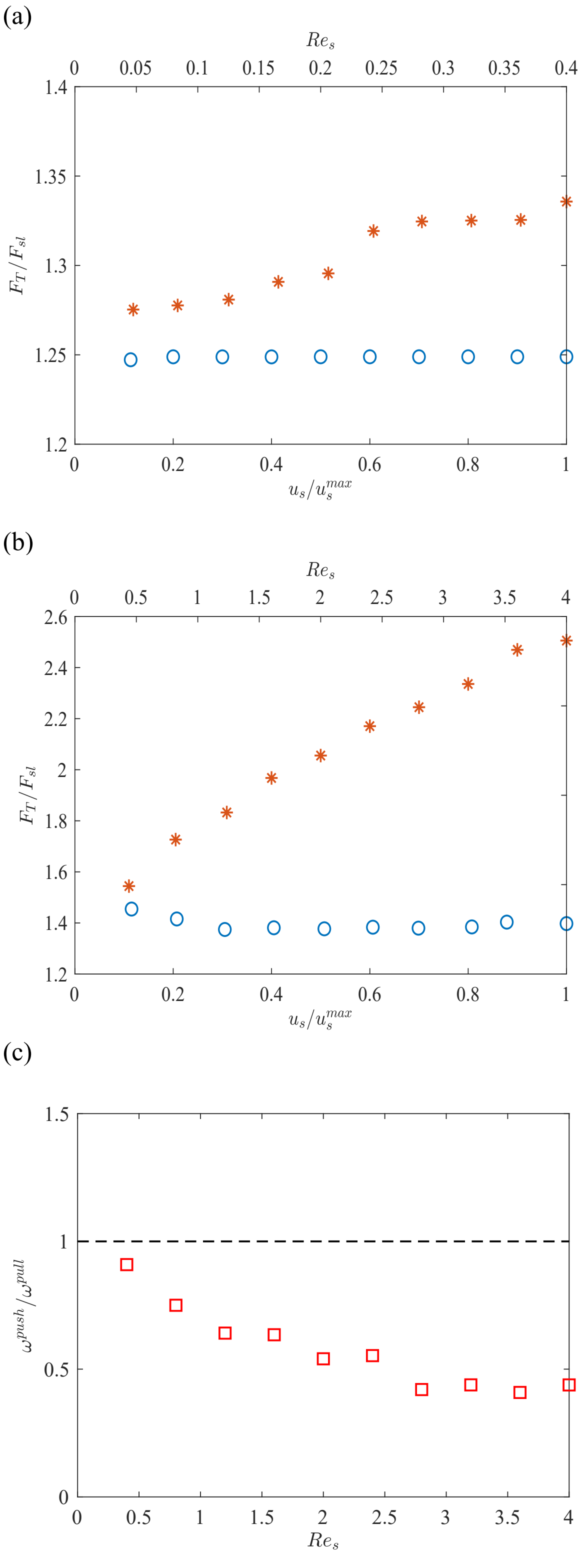

Figure 2.18: (a) swimming velocity reached by pusher (circles) and puller (stars) in a fluid initially at rest with $Re = 1$; (b) in a fluid with $Re = 10$. (c) squares: ratio between the maximum vorticity generated by pushers (ω^{push}) and pullers (ω^{pull}). The dashed line indicates $\omega^{push}/\omega^{pull} = 1$ (here $Re = 10$).

When $Re_s \ll 1$, for a given $\mathbf{F}_T$, pushers and pullers reach exactly the same u_s. As $Re_s \lesssim \mathcal{O}(1)$, it is found that for a given $\mathbf{F}_T$, pusher and puller swimmers reach different swimming velocities. Pushers show a constant ratio $\mathbf{F}_T/\mathbf{F}_{sl}$, as u_s increases, indicating a linear relationship between u_s and $\mathbf{F}_T$, up to $Re_s = 4$. With a pre-factor of the order of the unity, the external force acting on a pusher swimmer can be reasonably described by a slender body theory (see Fig. 2.18a). This is not the case for pullers: a non-linear relationship between u_s and $\mathbf{F}_T$, indeed holds in the range $0.04 \leq Re_s \leq 4$. Moreover, pullers are less efficient since they need a greater propulsive force to reach the same swimming velocity of pushers. The origin of this finding can be detected in Fig. 2.18c where it is shown the ratio between the maximum vorticity generated by pushers and pullers, $\omega^{push}/\omega^{pull}$, in the range $0.4 \leq Re_s \leq 4$. The ratio passes from being $\mathcal{O}(1)$ at small Re_s to about 0.5 at $Re_s = 2$, almost monotonically.

This findings are consistent with the results in Ref. [105] where the self-propulsion of pusher and puller squirmers has been investigated for Reynolds numbers between 0.01 and 1000. Authors found that pushers have efficient convection of vorticity past their surface leading to a steady axisymmetric flow that remains stable up to large Reynolds numbers. In contrast, pullers trap vorticity within their wake, which leads to flow instabilities causing a decrease in the swimming velocity at large Reynolds numbers. A deeper investigation of the flow field generated by slender swimmers is required for a full explanation of the differences in locomotion between slender pushers and pullers, especially for large Re_s, which is not the focus of this thesis.

Measuring flow signals net of self-motion

Once the swimming velocity has been assessed, it is possible to proceed to investigate the capability of a slender swimmer to measure flow properties in terms of swimmer position and velocity of the swimmer end points (red dots in Fig. 2.3). To do that, a time-dependent version of the three-dimensional ABC (Arnold-Beltrami-Childress) flow [88] it is considered:

$$\begin{aligned} u &= \sin(z + \epsilon\sin(\Omega t)) + \cos(y + \epsilon\sin(\Omega t)) \\ v &= \sin(x + \epsilon\sin(\Omega t)) + \cos(z + \epsilon\sin(\Omega t)) \\ w &= \sin(y + \epsilon\sin(\Omega t)) + \cos(x + \epsilon\sin(\Omega t)) \end{aligned} \tag{2.25}$$

where $\epsilon = 1$ is the cell oscillation amplitude, and $\Omega = 1.5$ the cell oscillation frequency. This choice ensures high chaoticity uniformly distributed in space with a maximum Lyapunov exponent $\lambda = 0.8$ (see Ref. [88]). In order to obtain the ABC flow as a solution of the Navier-Stokes equations, the volume force, $\mathbf{f}^V = \partial_t \mathbf{u} - (1/Re)\partial^2\mathbf{u}$, has been applied to the right hand side of Eq. (2.6). For the Reynolds numbers analyzed here, the resulting flow field turns out to be a stable (time-dependent) fixed point of the Navier-Stokes equations which agrees with the analytical expression.

Simulations with $Re = 1$ and 10, have been performed always checking that the flow remained stable for values of Re at least up to 100. Also in this case, the use of this setting allows us to perform a direct and reliable comparison between the swimmer velocity differences evaluated at its ends and the corresponding velocity difference of the underlying (unperturbed) fluid flow. With unperturbed flow velocity, we mean the velocity field in the absence of the swimmer (i.e. excluding the swimmer self-motion). Here, the swimmer inertia has been quantified via the Stokes number expressed in terms of the flow Lyapunov exponent, λ: $St = \tau_s \lambda$. Moreover, another parameter needs to be introduced; the swimming number, Φ, expressed in terms of the ratio between the measured swimming velocity and the fluid root mean square velocity, namely,

$\Phi = u_s/u_{rms}$. The parameter Φ together with St, Re and Re_s are the control parameters entering in the numerical experiments.

Also in this case, the velocity difference between the swimmer end points (red dots in Fig 2.3), $\delta\mathbf{V}$, and the corresponding unperturbed flow velocity difference $\delta\mathbf{u}$ has been considered and projected along a plane normal to the swimmer axis in a way to minimize the effect of inextensibility constraint, as already done in Sec. 2.4.1.. The normal plane used is the same employed in Sec. 2.4.1. for rigid fibers passively advected by flow, although the results seem to be independent on this particular choice.

The normalized root-mean-square error ($NRMSE$), between $\delta V_\perp$ and $\delta u_\perp$, with the corresponding error bars are reported in Fig. 2.19, for the time-dependent ABC flow. Examples of time series of $\delta V_\perp$ and $\delta u_\perp$ are presented in the insets. The measured $NRMSE$ for both pushers and pullers with $St = 0.04$ and 0.1, for $Re = 1$ are reported in Fig 2.19a, and for $Re = 10$ in Fig 2.19b, while Φ is ranging between 0 and 1. For the sake of comparison, it is also shown the $NRMSE$ for $\Phi = 0$, i.e. the slender body without propulsion. The $NRMSE$ is defined as:

$$NRMSE = \frac{\left(\frac{1}{t_{max}}\int_{t=0}^{t_{max}}(\delta V_\perp - \delta u_\perp)^2\,dt\right)^{\frac{1}{2}}}{\pi G} \tag{2.26}$$

where $G = \sqrt{\langle\dot\gamma^2\rangle}$ being the flow strain rate, with $\langle\dot\gamma^2\rangle = \langle e_{ij}e_{ij}\rangle$, $e_{ij} = \frac{1}{2}(\partial_i u_j + \partial_j u_i)$ is the strain tensor, and π is half of the periodicity box size. t_{max} has been chosen in a way to obtain a statistical convergence of the selected statistical indicator. Error bars represent the residual variability of the mean values at convergence. Apart from short time intervals where $\delta V_\perp$ and $\delta u_\perp$ are quite different, due to rapid changes of the underlying strain-rate/vorticity, both pusher and puller swimmers are able to ‘measure’ the unperturbed flow transverse velocity difference with satisfactory agreement across the different values of Φ (see Fig. 2.19). In particular, when $Re = 1$ and $St = 0.04$ the $NRMSE$ of pushers and pullers is almost the same, with a slight growth by increasing Φ. If $St = 0.1$, larger differences arise between pushers and pullers. $NRMSE$ of puller remains almost constant across the swimming numbers, Φ, while for pushers the $NRMSE$ presents a general increase by increasing Φ, with a maximum $NRMSE$ just over 2% (Fig. 2.19a). When considering $Re = 10$ and $St = 0.04$, the $NRMSE$ of puller increases more than the $NRMSE$ of pushers. Moving to $St = 0.1$, pullers maintain almost constant the $NRMSE$ up to $\Phi = 1$. For pushers, the $NRMSE$ behaves as that of pullers up to $\Phi = 0.7$; for larger swimming numbers the $NRMSE$ of pusher starts to increase up to a value around 3% (Fig. 2.19b).

In light of the results discussed above, two different patterns can be identified: first, pushers are more efficient to measure flow properties when their inertia is low; second, when swimmer inertia is relatively high, the conclusion is opposite: pullers are now more efficient than pushers to ‘measure’ flow properties. The conclusions drawn above hold for both value of Re we have considered, thus suggesting the robustness of this findings, at least in the range of Reynolds number investigated.

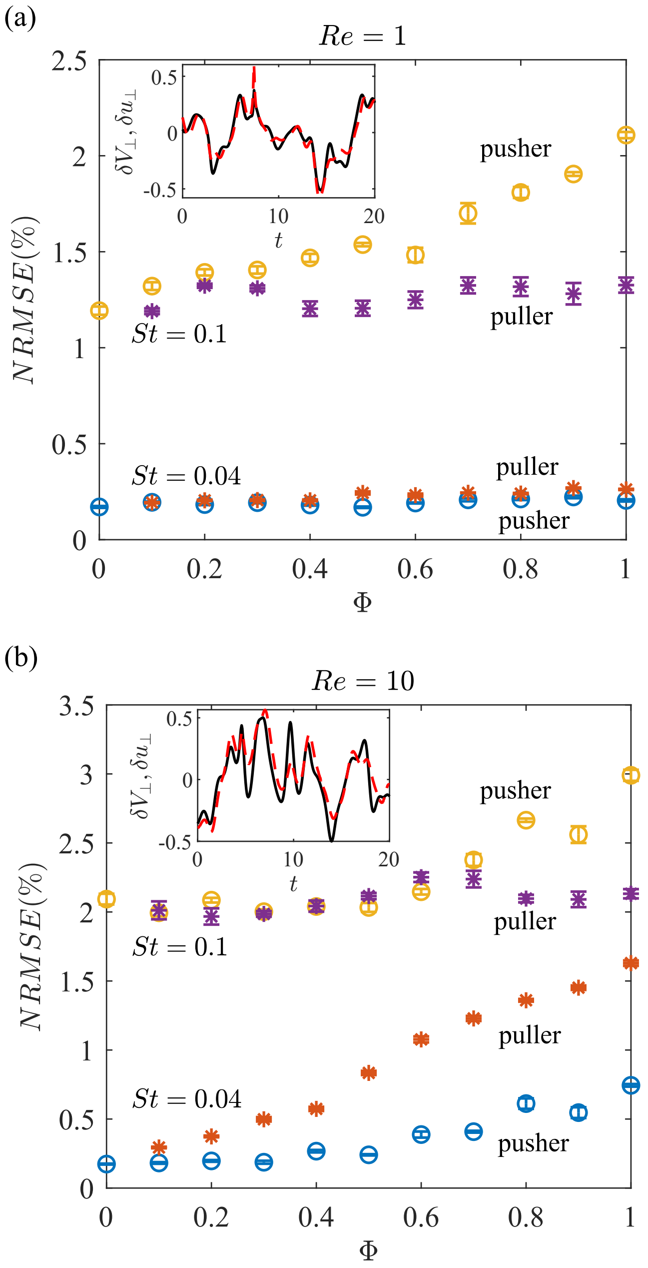

Figure 2.19: Normal root-mean-square error, with the respective error bars, between the transverse velocity difference $\delta V_\perp$ of swimmer, and the unperturbed ABC time-dependent flow $\delta u_\perp$, with (a) $Re = 1$ and (b) $Re = 10$, against Swimming number Φ. Blue circles and red stars are pusher and puller swimmers, respectively, with $St = 0.04$. Yellow circles and purple stars are pusher and puller swimmers, respectively, with $St = 0.1$. The markers in $\Phi = 0$, report the NRMSE for a slender object without propulsion. Insets: transverse velocity difference of a puller swimmer $\delta V_\perp$ (dashed line) and unperturbed time-dependent ABC flow $\delta u_\perp$ (solid line), for $St = 0.1$ and $\Phi = 0.1$.

2.5. Summary and outlook

The first part of this chapter is focused on the capability of measuring the whole structure of the velocity gradient in steady, unsteady regular and chaotic cellular flows by means of Lagrangian tracking of assembly of rigid fibers. Two different kinds of fiber models have been considered: first an active model, a fully-coupled fiber described in terms of an immersed-boundary method, and, second, a passive model, a one-way coupling where the fiber is described by the slender body theory. We have characterized the role of fiber inertia by defining a rotational Stokes number, which it is evaluated as a function of other parameters such as the fiber linear density. The rotational Stokes number has been evaluated for the sole active fiber, since for the fiber modeled with the passive approach it is an assigned parameter. By considering the velocity difference between the fiber end-points and the same difference relative to the underlying fluid velocity, both projected along the direction normal to the fiber, the fiber turns out to be a proxy of such two-point quantity. For sufficiently short fibers, two-point velocity difference reduces to the transverse component of the flow velocity derivative along the fiber direction. Furthermore, the comparison between results obtained for the active model (two-way coupling) and the passive model (one-way coupling) suggests that the coupling between the flow and the fiber could be neglected, at least for small St.

The observed capability of rigid fibers to measure two-point flow observables has potential application in experimental measurement techniques allowing to access small-scale, multi-point properties of fluid flows, offering an alternative to other methods that have been proposed which rely on complex elaborations using PIV/PTV (Refs. [49, 106, 107]). Attention will thus be paid to the practical implementation of the outlined concept in a laboratory environment. Preliminary results in this direction appear very encouraging [4] confirming the validity of the idea of using rigid fibers as a way of measuring flow properties, an idea that seems successful well beyond the laminar/chaotic examples analyzed here. The idea can be extended to measurements of three-dimensional and/or turbulent flows, along with considering assembly of fibers that would be able to describe the full structure of the velocity gradient.

The second part of the chapter investigates the perception of hydrodynamic signals by slender swimmers commonly classified as pusher or puller type. Two different swimmer models have been proposed. In the simplest model, the locomotion of a self-propelled organism is described in terms of two oppositely directed point forces of equal magnitude, but acting on different points of the Lagrangian grid associated to the swimmer. The resulting numerical solution of the flow field generated by the swimmer motion has been compared with the analytical solution corresponding to the so-called di-Stokeslet, obtaining excellent agreement.

As a less idealized model of swimmer, a model for a slender swimmer has been proposed by imposing the no-slip condition and the propulsion force on the same half length of the slender motile object, the spreading of the pushing/pulling forcing acting on the fluid being imposed on the other half (the so-slip condition was not applied in that portion of the Lagrangian grid). The resulting flow motion has been successfully compared with the solution for an extended stresslet, where the velocity field in a point of the flow domain is reconstructed by superimposing several (5 in the present study) di-Stokeslet solutions.

Once the models have been validated in the limit of Stokes flows in a fluid initially at rest, the more realistic model has been exploited in a chaotic flow field up to a flow Reynolds number of 10 (i.e. far from the Stokes regime), a swimming number ranging between zero and one, and different swimmer inertia. The main results can be summarized as follow. i) Pushers and pullers differently react to an imposed propulsive force. The net result of this observation is that they reach different swimming velocities for the same, given, propulsive force. Interestingly, if one exploit the slender-body theory to relate the imposed propulsion to the resulting swimming velocity, one finds that it reasonably works for pushers while this is not for pullers. The invoked reason to understand this finding is the different vorticity generated by the motion of the two swimmer type. ii) For a wide range of flow/swimmer Reynolds numbers, both pusher and puller swimmers are able to sense hydrodynamic signals with good accuracy, net of swimmer self-motion. This means that, despite the perturbation caused by the swimmer motion, there exist hydrodynamics observable practically unaffected by the swimmer motion, i.e. the swimmer velocity differences evaluated at the swimmer ends, projected along a direction on a plane normal to the swimmer orientation.

This finding opens to unconventional non-intrusive techniques to measure two-point flow properties (e.g. gradients) by following artificial self-propelled slender objects, thus generalizing the founding idea at the origin of the recently proposed ‘fiber tracking velocimetry’ [4].

Chapter 3
The fluid dynamics of airborne infection

This chapter is devoted to understand the role of the turbulence on the fate of virus-containing droplets expelled during a human cough under realistic conditions. To this aim, high resolution DNS have been performed for the fluid flow and humidity field, complemented by a passive Lagrangian solver for the droplet dynamics including a dynamical equation for the evolution of the droplet radii modeling the evaporation-condensation process. Such an accurate description is nowadays possible thanks to the deep understanding achieved in the microphysics of small liquid droplets under different ambient conditions. The fine structure of turbulence is expected to be crucial to correctly account for its effect on droplet evaporation. The chapter is structured as follow: Sec. 3.1. introduces the background and research motivations, Sec. 3.2. presents the employed numerical methods, Sec. 3.3. shows how a full account of turbulence affects the results on the fate of virus-containing droplets, Sec. 3.4. shows the dependence of the results on the droplets initial size distribution and different ambient humidity, Sec. 3.5. studies the dependence of results on the the airborne virus spreading on gender. Sec. 3.6. investigates the effectiveness of the the barriers as protection devices within indoor environment and finally Sec. 3.7. draws some conclusions.

3.1. Background and motivations

Turbulent transport of droplets in a jet or puff is a problem of paramount importance in science and engineering that nowadays has become even more important given the global emergency caused by the COVID-19 infection. The implementation of predictive models for the dynamics of the exhaled air emitted through respiratory events is important for a deep comprehension of the long-range transport mechanisms responsible for the infection spread far from the emission source. Some attempts in this direction appeared in the literature. In way of example, Bourouiba et al. [108] provided a simple interpretation of their experimental results obtained in the laboratory by generating a two-phase flow consisting of fresh water with heavier particles dispersed in it, which was abruptly introduced, through a piston, into a tank containing salty (and, therefore, denser) water. The experiments mimics a cloud of warmer (with respect to the ambient) air hosting droplets as it happens during a respiratory emission. Three different steps can be identified during a respiratory emission: the initial jet behavior of the emitted fresh fluid, its transformation into a puff-thermal in the far field, and, finally, the evolution of the two-phase mixture induced both by the entrainment process and by the sedimentation of the transported particles. The proposed theoretical model accurately predicts the observed time dependence of the longitudinal coordinate of the cloud center of mass by estimating the entrainment coefficients from the corresponding dependence of the characteristic 'radius' of the cloud from the longitudinal coordinate of the cloud center of mass.

The theoretical model proposed by Bourouiba et al. [108] has clear limitations. It basically ignores two important aspects of the phenomenon: the turbulent character of the fluid motion and its two-phase nature. The flow associated with respiratory emissions is indeed characterized by high values ($\sim 10^4$) of the Reynolds number [109]. Because of turbulence, the flow out of the mouth is extremely irregular, fluctuating, both in space and in time. Moreover, the mechanism of entrainment not only affects the buoyancy of the air cloud but also induces a reduction of its water vapor content. The ambient humidity is indeed smaller than the humidity of the exhaled air. The hypothesis that the environment is not saturated, in cases where the temperature of the cloud (about 30–35^oC during expulsion) is comparable with that of the environment (for example about 25^oC), is equivalent to saying that the absolute humidity of the environment is sufficiently lower than that of the exhaled air. As time runs, due to the mixing of the two air masses, the temperature of the exhaled air is lowered and its absolute humidity is reduced. The first effect, by lowering the saturated vapor pressure, favors condensation, but it is immediately counteracted by the second, and most important, which favors the evaporation of the droplets.

The turbulence characterizes also the mixing process which determines how the exhaled air, initially saturated of water vapor, dilutes with ambient air. This mechanism is intimately chaotic characterized by persistent fluctuations in the relative humidity field. The turbulent nature of the relative humidity field can have a dramatic effect on the fate of the evolution of saliva droplets. Cloud formation in the high atmosphere provides a large-scale example of the condensation/evaporation processes taking place in the air cloud exhaled from the mouth during coughing/sneezing/talking. The crucial role of turbulent fluctuations in the relative humidity field was isolated in relation to its role in the cloud droplet growth by condensation [26]. As a result of this study, turbulence turned out to be the key ingredient to explain the observed spectrum broadening of cloud droplets resulting at the end of the condensation stage. Due to this process of size broadening, the droplets can reach different terminal velocities, a fact that allows them to start the second phase of their growth dominated by collision and coalescence.

For the saliva droplets, the growth by condensation is certainly not the key phenomenon at play, at least on average. On the contrary, the expelled droplets, in general, move in an under-saturated medium. In this framework, the interesting questions, still largely unanswered, concern the way and the rate at which these droplets evaporate. To date, the evaluation of these characteristics is done via mean-field arguments, which either ignore the effects of turbulent fluctuations or describe them in an extremely simplified way. For the problem of respiratory droplet spreading, typical approaches found in the current literature are based on large-eddy simulations (LESs) and Reynolds-averaged Navier-Stokes (RANS) equations [110, 111, 112]. By definition, LESs and RANS equations only describe turbulent fluctuations at the largest scales involved. By reversing the way of reasoning followed to understand what happens in a cloud in the upper atmosphere, one can easily imagine that the role of turbulence is very important to determine the fate of expiratory droplets during their evaporation stage. Droplets that remain longer in less under-saturated zones will evaporate slower than other droplets remaining in regions where the relative humidity is lower.

Numerical approaches able to fully describe all the spatial and temporal scales, such as DNS, are thus crucial to assess quantitatively how turbulence dictates the fate of virus-containing droplets, and consequently provide useful insights on the spread of SARS-CoV-2 and other airborne transmitted infections.

3.2. Methods

This section will discuss state-of-the-art direct numerical simulations (DNS) in order to simulate the turbulent air flow exhaled from the mouth during a violent expiatory event, such as human cough. Moreover, a Lagrangian model for the droplet dynamics and their radii evolution due to evaporation will be described.

3.2.1. DNS of cough-generated airflow

The airflow exhaled from the mouth is ruled by the incompressible Navier-Stokes equations

$$\partial_t \mathbf{u} + \mathbf{u} \cdot \boldsymbol{\partial} \mathbf{u} = -\frac{1}{\rho_a} \boldsymbol{\partial} p + \nu \partial^2 \mathbf{u}, \tag{3.1}$$

$$\boldsymbol{\partial} \cdot \mathbf{u} = 0 \tag{3.2}$$

with ν being the air kinematic viscosity and ρ_a the air density. The list of all relevant parameters used in this study is reported in Table 3.1. Instead of simulating the evolution of the absolute humidity field (the exhaled air is saturated, or close to saturation [113]), it is more convenient to model directly the supersaturation field (i.e., $s = RH - 1$, RH being the relative humidity). Indeed, the supersaturation dictates the evaporation-condensation process, as it appears in the evolution equation for droplet radius [114]. The supersaturation field is ruled by the advection-diffusion equation [26]:

$$\partial_t s + \mathbf{u} \cdot \boldsymbol{\partial} s = D_v \partial^2 s \tag{3.3}$$

D_v being the water vapor diffusivity. Equation (3.3) assumes that the saturated vapor pressure is constant, an assumption that holds as long as the ambient is not much colder than the exhaled air, which is at about 30 °C according to Morawska et al. [113]. To simulate the airflow generated by a human cough, it has been adopted the inlet air velocity profile proposed by Gupta et al. [109], as shown in Fig. 3.1 The air is assumed to be saturated (i.e., $s = 0$) as it exits from the mouth opening of area $4.5\mathrm{cm}^2$. The duration of the expulsion is approximately $0.4\mathrm{s}$ and the peak velocity is $13\mathrm{m/s}$. The resulting Reynolds number (based on the peak velocity and on the mouth average radius) is about 9000. The flow field is thus fully turbulent as one can easily realize by looking at Fig 3.2.

Before discussing how the liquid part of the two-phase mixture is modeled, let us first validate the puff dynamics of the exhaled air. By means of a simple phenomenological approach, we show how one can derive the temporal scaling for the standard deviation of a cloud of tracers in a turbulent puff. The starting point is the result obtained by Kovasznay et al. [116] for the temporal scaling of the puff radius, $\sigma^u \sim t^{1/4}$ obtained by the authors in terms of a simple eddy-viscosity approach. A recent paper by Mazzino and Rosti [117] extend the temporal predictions for the puff bulk properties to the initial range two-point fluctuations. In order to determine the standard deviation, σ, for a cloud of tracers carried by the turbulent puff, one has to resort to the concept of relative dispersion. The latter can be described in terms of arguments

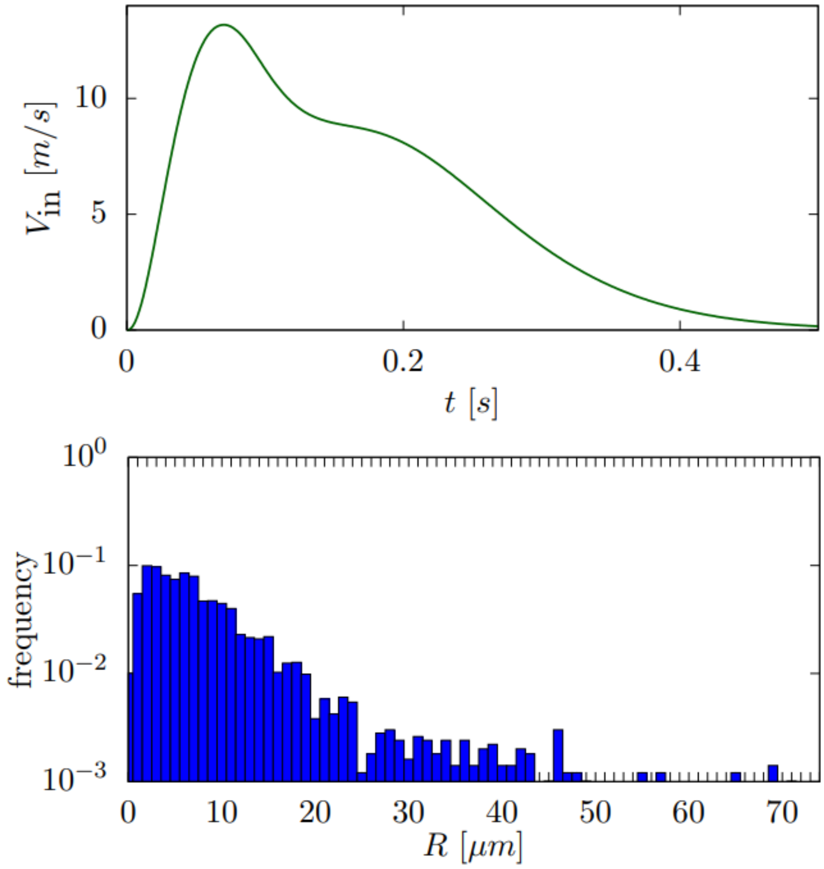

Figure 3.1: Top: Time-varying inlet air velocity representative of cough according to Ref. [109]. Bottom: Droplet initial size distribution according to Ref. [115].

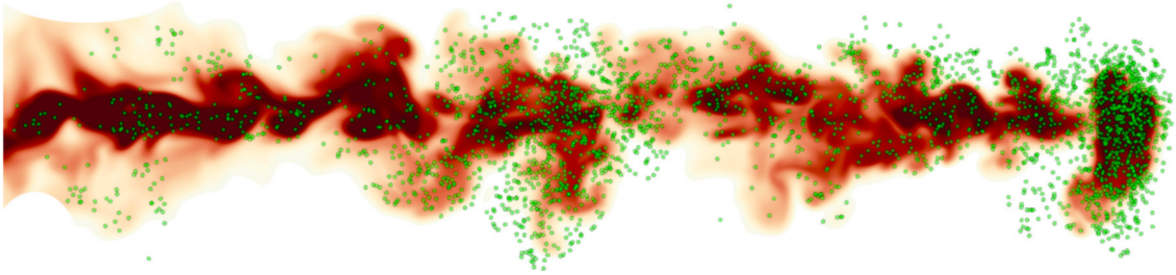

Figure 3.2: Snapshot of the expiratory event 7.6s after start coughing obtained from our numerical simulations. Different colors represent different values of the humidity field ranging between the 99$\%$ of the ambient humidity RH_a (red areas) and RH_a (white areas). Green bullets (shown not in scale) identify the position of the airborne droplets, initialized with the sizes taken from Ref. [115]. The streamwise extension of the puff at this time is $2.6\mathrm{m}$.

à la Richardson [118]. Accordingly, $\sigma(t) \sim \epsilon(t)^{1/2}t^{3/2}$ where $\epsilon(t)$ is the turbulence dissipation rate. This latter can be easily estimated from the well-known Kolmogorov $4/5$-law evaluated at the integral scale σ^u. Namely,

$$\epsilon(t) \sim \frac{\delta U^3}{\sigma^u} \quad \text{with} \quad \sigma^u = \frac{\delta U}{t}, \tag{3.4}$$

from which one immediately gets $\epsilon(t) \sim t^{-5/2}$. The scaling law for ϵ immediately leads to the temporal scaling for the standard deviation of the tracer cloud: $\sigma(t) \sim t^{1/4}$. Finally, because $\langle s \rangle$ is proportional to the puff volume, and this latter goes as $\sigma^3 \sim t^{3/4}$, the decay law for the mean supersaturation is $\langle s(t) \rangle \sim t^{-3/4}$.

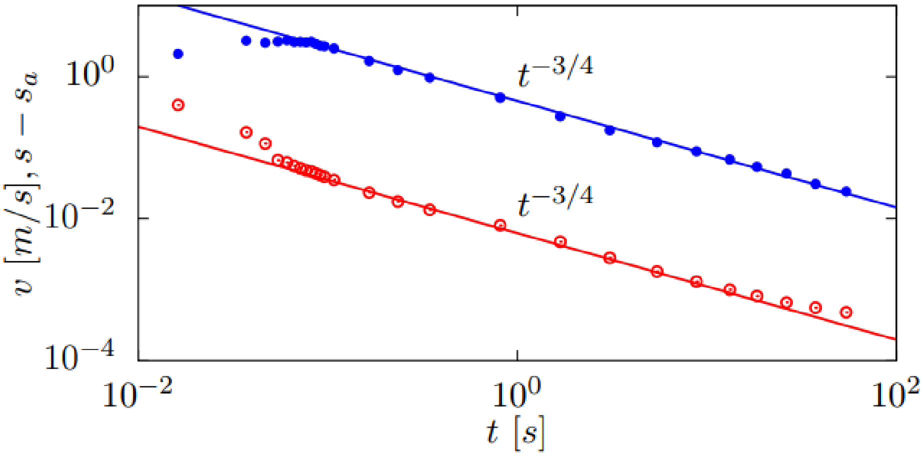

Figure 3.3: Mean velocity v of the exhaled air (solid blue circles) and of the supersaturation $s - s_a$ (open red circles) as a function of time. The blue line shows the scaling predicted for the velocity field in Ref. [116] which also holds for the supersaturation field (red line).

The same law holds for the mean stream-wise puff velocity [116]. The reliability of our puff dynamics is demonstrated in Fig. 3.3 , which clearly shows the expected scaling laws for more than two decades with high accuracy.

We are now ready to introduce the model for the liquid part of the two-phase mixture. It is described as an ensemble of N inertial particles ruled by the well-known set of equations [119]

$$\dot{\mathbf{X}} = \mathbf{U}_i(t) + \sqrt{2D_v}\eta_i(t), \quad \text{with} \quad i = 1, ..., N \tag{3.5}$$

$$\dot{\mathbf{U}}_i = \frac{\mathbf{u}(\mathbf{X}_i(t), t) - \mathbf{U}_i(t)}{\tau_i} + \boldsymbol{g} \tag{3.6}$$

$$\tau_i = \frac{2\rho_{Di}/\rho_a R_i^2(t)}{9\nu} \tag{3.7}$$

where N is the number of exhaled droplets (here $N \approx 5000$ according to Duguid [115]), $\mathbf{X}_i$ is the position of the $i\mathrm{th}$ droplet and $\mathbf{U}_i$ its velocity, and, finally, $\boldsymbol{g}$ is the gravitational acceleration. Each droplet is affected by a Brownian contribution via the white-noise process η_i. The reason for considering a nonvanishing Brownian force acting on the position process is twofold and detailed in Ref. [120]. Here, ρ_{Di} is the density of the $i\mathrm{th}$ droplet. Finally, τ_i is the Stokes relaxation time of the $i\mathrm{th}$ droplet and R_i is its radius.

Since the flow is neither statistically homogeneous nor stationary, we consider the characteristic flow time scale $\tau_{flow} = \sqrt{\nu\sigma_u/v^3}$, where v is the puff mean velocity measured by the Lagrangian tracers (as later described in Sec. 3.3.1.). Using the latter, we can define the Stokes number for the $i\mathrm{th}$ droplet as $St = \tau_i/\tau_{flow}$, which allows us to clearly distinguish droplets whose trajectory is (or is not) dominated by inertia, i.e., $St > 1$ (or $St < 1$).

Droplets are assumed to be made of salt water (water and NaCl) and a solid insoluble part (mucus) [121]. The droplet radius evolves according to the ruling equation [114]

$$\frac{d}{dt}R_i^2(t) = 2C_R\left(1 + s(\mathbf{X}_i(t), t) - e^{\frac{A}{R_i(t)} - B\frac{r_{Ni}^3}{R_i^3(t) - r_{Ni}^3}}\right), \tag{3.8}$$

$$R_i(t) = r_{Ni} \quad \text{for} \quad s \leq s_{crh} \quad \text{(crystallization).} \tag{3.9}$$

Hydrodynamic interactions between particles and flow can affect transport in specific conditions (e.g. [122]). Here, no feedback of this equation to Eq. (3.3) is considered because of the very small values of the liquid volume fraction, typically smaller than 10^{-5} [123, 108] or even smaller according to Johnson et al. [124] and Morawska et al. [113], and thus droplet back-reaction on the flow is largely negligible. In Eq. (3.8), C_R is the droplet condensational growth rate, $s_{crh} = -0.55$ ($CRH = 0.45$, the so-called crystallization RH or efflorescence RH) for NaCl [125]. Figure 3 of Ref. [126] show the weak dependence of CRH on temperature. r_{Ni} is the radius of the (dry) solid part of the $i\mathrm{th}$ droplet when the salt is entirely crystallized (i.e., below CRH). The dependence of r_{Ni} on physical, chemical, and geometrical properties of the exhaled droplets is reported in the next section together with the expressions of parameters A and B. On the basis of the parameters assumed here, the ratio $r_{Ni}/R_i(0)$ is 0.16, which agrees with the estimations discussed in Ref. [127].

Physical and chemical properties of cough

The complete list of physical and chemical parameters appearing in our model, along with their baseline values adopted in this investigation, is presented in Table 3.1. Some of these quantities are deduced by other parameters. Specifically, the saturation vapor pressure above a flat water surface at temperature T (where T is in degrees Celsius) is obtained using the Magnus-Tetens approximation [128]

$$e_{sat} = 6.1078 \times 10^2 e^{(17.27T_a/(T_a+273.15))}\mathrm{Pa}, \tag{3.10}$$

and the droplet condensational growth rate is given by

$$C_R = \left[\frac{\rho_w\, R_v\,(273.15+T_a)}{e_{sat}\, D_v} + \frac{\rho_w\, L_w^2}{k_a\, R_v\,(273.15+T_a)^2} - \frac{\rho_w\, L_w}{k_a(273.15+T_a)}\right]^{-1} \tag{3.11}$$

The expressions of the coefficients A and B appearing in Eq. (3.8) follow from Ref. [12] (p. 176):

$$A = \frac{2\sigma_w}{R_v(T_a+273.15)\rho_w} \qquad \text{and} \qquad B = \frac{n_s \Phi_s \epsilon_v M_w \rho_s}{M_s \rho_w}, \tag{3.12}$$

where $n_s = 2$ is the total number of ions into which a salt molecule dissociates, $\Phi_s = 1.2$ is the practical osmotic coefficient of the salt in solution [129], $\epsilon_v = \epsilon_m(\rho_N/\rho_s)$ is the volume fraction of the dry nucleus with respect to the total droplet is the volume fraction of dry nucleus with respect to the total droplet. To complete the description, some useful relations can be easily derived from the quantities specified in Table 3.1. First, assuming that the dry nucleus of droplets is composed by a soluble phase (NaCl) and an insoluble phase (mucus) and that the typical value of the mass fraction of the former is known, the overall density of the dry nucleus can be expressed as

$$\rho_N = \frac{\rho_u}{1-\epsilon_m[1-(\rho_u/\rho_s)]} = 1.97 \times 10^3 \quad \mathrm{kg/m^3}. \tag{3.13}$$

Similarly, the density of the entire ith droplet turns out to be

$$\rho_{D\,i} = \rho_w + (\rho_N - \rho_w)\left(\frac{r_{N\,i}}{R_i(t)}\right)^3, \tag{3.14}$$

where the radius of the (dry) solid part of the droplet when NaCl is totally crystallized (i.e., below CRH) is given by

$$r_{N\,i} = R_i(0)\left(\frac{\mathcal{C}\,\rho_w}{\mathcal{C}\,\rho_w + \rho_N(1-\mathcal{C})}\right)^{1/3}, \tag{3.15}$$

being $\mathcal{C}$ the mass fraction of dry nucleus with respect to the total droplet.

Table 3.1: Physical and chemical properties assumed in the present study.

Mean ambient temperature	T_a	$25\,^\circ\mathrm{C}$
Crystallization (or efflorescence) RH	CRH	45%
Deliquescence RH	DRH	75%
Quiescent ambient RH	RH_a	60%
Density of liquid water	ρ_w	$9.97 \times 10^2\,\mathrm{kg/m^3}$
Density of soluble aerosol part (NaCl)	ρ_s	$2.2 \times 10^3\,\mathrm{kg/m^3}$
Density of insoluble aerosol part (mucus)	ρ_u	$1.5 \times 10^3\,\mathrm{kg/m^3}$
Mass fraction of soluble material (NaCl) w.r.t. the total dry nucleus	ϵ_m	0.75
Mass fraction of dry nucleus w.r.t. the total droplet	$\mathcal{C}$	$1\,\%$
Specific gas constant of water vapor	R_v	$4.6 \times 10^2\,\mathrm{J/(kg\,K)}$
Diffusivity of water vapor	D_v	$2.5 \times 10^{-5}\,\mathrm{m^2/s}$
Density of air	ρ	$1.18\,\mathrm{kg/m^3}$
Kinematic viscosity of air	ν	$1.8 \times 10^{-5}\,\mathrm{m^2/s}$
Heat conductivity of dry air	k_a	$2.6 \times 10^{-2}\,\mathrm{W/K\,m}$
Latent heat for evaporation of liquid water	L_w	$2.3 \times 10^6\,\mathrm{J/kg}$
Saturation vapor pressure	e_{sat}	$0.616\,\mathrm{kPa}$
Droplet condensational growth rate	C_R	$1.5 \times 10^{-10}\,\mathrm{m^2/s}$
Surface tension between moist air and salty water	σ	$7.6 \times 10^{-2}\,\mathrm{J/m^2}$
Molar mass of NaCl	M_s	$5.9 \times 10^{-2}\,\mathrm{kg/mol}$
Molar mass of water	M_w	$1.8 \times 10^{-2}\,\mathrm{kg/mol}$

3.2.2. Numerical and geometrical setup

The employed in-house flow solver is named FUJIN [130] and is based on the (second-order) central finite-difference method for the spatial discretization and the (second-order) Adams-Bashfort scheme for the temporal discretization. The Poisson equation for the pressure is solved using the 2DECOMP library coupled with a fast and efficient fast Fourier transform (FFT)-based approach. The solver is parallelized using the massage passing interface protocol and has been extensively validated in a variety of problems [5, 6, 92]. The droplet dynamics is computed via Lagrangian particle tracking complemented by an established droplet condensation model that has been successfully employed in the past for the analysis of rain formation processes [26]. The governing equations for the droplet dynamics Eqs. (3.5-3.8) are advanced in time using the explicit Euler scheme. The numerical domain is discretized with a uniform grid of size $3.5\mathrm{mm}$ and we verified that the following results are independent of the grid size, statistical sample, and droplet initial condition. The fluid flow equations (3.1), (3.2) and (3.3) are solved within a domain box of length $L_x = 4\mathrm{m}$, height $L_y = 2.5\mathrm{m}$, and width $L_z = 1.25\mathrm{m}$, as depicted in Fig. 3.4.

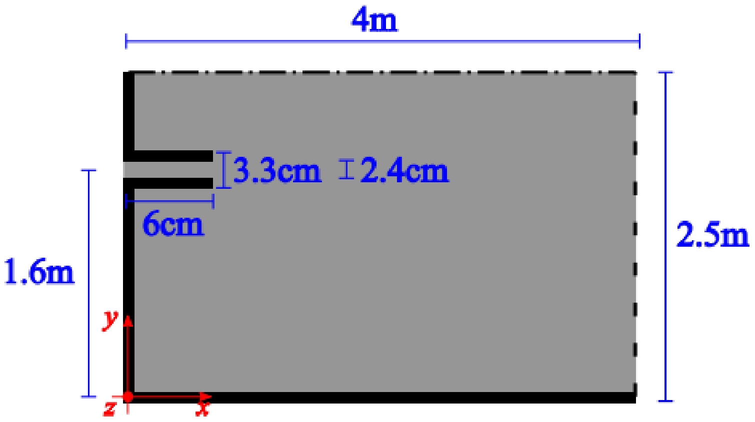

Figure 3.4: Side-view sketch of the domain used in our DNS (note that the figure is not to scale).

The fluid is initially assumed at rest, i.e., $\mathbf{u}(x, 0) = 0$. Air is thus injected through a circular pipe, placed at $z = 1.6\mathrm{m}$ above the floor, of length $l = 6\mathrm{cm}$ and internal diameter $d = 2.4\mathrm{cm}$ as an essential model of a human mouth. We use the time-varying velocity profile proposed by Gupta et al. [109] (shown in Fig. 3.1) to reproduce the cough-associated airflow. The no-slip condition applies at the bottom, i.e., $y = 0$, and left wall, i.e., $z = 0$ (solid lines in Fig. 3.4). At the top ($y = L_y$, dot-dashed), we prescribe the free-slip condition. For the supersaturation field s, at $t = 0$ we have $s(x, 0) = s_a = RH_a - 1$ everywhere in the domain. The inlet flow exiting from the mouth is assumed to be saturated air; i.e., $s = 0$. The Dirichlet condition $s = s_a$ is thus used at the bottom, left, and top boundaries. For both the velocity and supersaturation field, we impose a convective outlet boundary condition at the right boundary, $x = L_x$ (dashed line). Finally, periodic boundary conditions apply at the side walls, i.e., $z = 0$ and $z = L_z$.

In our simulations, the domain is discretized with uniform spacing $\Delta x = 3.5\mathrm{mm}$ in all directions, resulting in a total number of $N \approx 0.3$ billion grid points. Results are validated against the theoretical prediction for a turbulent puff (see Fig. 3.3). Moreover, we assessed the convergence with respect to the grid resolution, as it is shown in Fig. 3.5 (top) where we compare the probability density function of the particle evaporation time using the adopted grid setting with that obtained by doubling the spatial resolution. From the figure we can clearly observe that only minor differences occur, thus confirming the reliability of the chosen grid resolution.

The results discussed in the text are statistically significant. We varied this by halving the numerical sample (Fig. 3.5, middle) and by varying the release time of the droplets (Fig. 3.5, bottom), thus resulting in different dynamics due to the chaotic nature of the flow; for both tests the figure shows no appreciable differences.

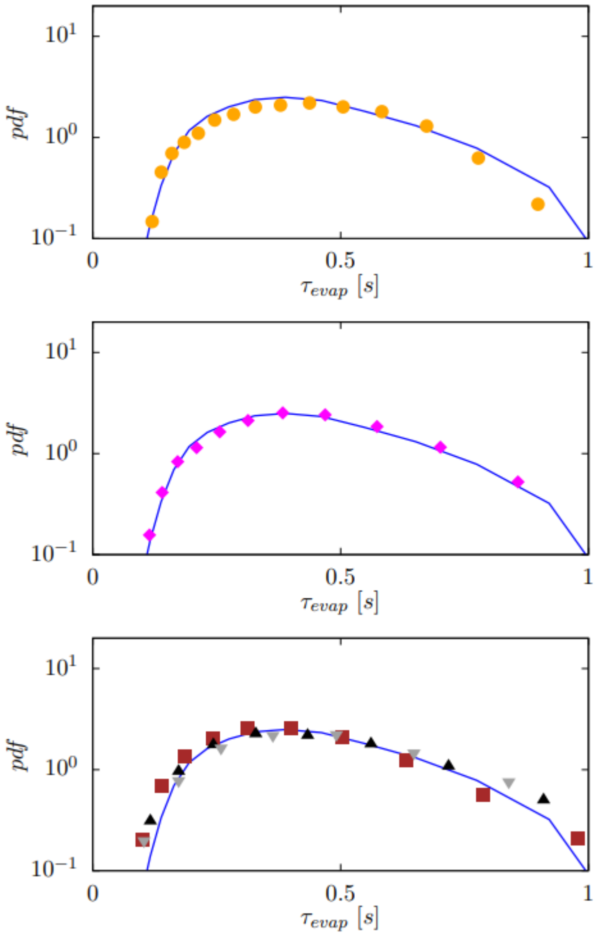

Figure 3.5: Top: Grid convergence analysis: probability density function of the particle evaporation time computed in the baseline case with spacing $\Delta x = 3.5\text{mm}$ (blue curve) and $\Delta x = 1.75\text{mm}$ (orange symbols). Middle: Convergence of the statistics: probability density function of the particle evaporation time computed in the baseline case with $N \approx 5000$ (blue line) and with half of them (magenta symbols). Bottom: Independency of the results from the initial condition: probability density function of the particle evaporation time computed in the baseline case (blue line) and when droplets are emitted with a time delay of 0.07s (brown), 0.14m (black), and 0.21s (gray).

3.3. Turbulence role in the fate of virus-containing droplets

This section is devoted to understand the combined role of turbulence and droplet inertia on the virus-containing droplet evaporation under realistic conditions mimicking a human cough. To do that, we perform accurate DNSs for the fluid flow and humidity field, complemented by a Lagrangian solver for the droplet dynamics including a dynamical equation for the evolution of the droplet radii modeling the evaporation-condensation process (see Fig. 3.2).

For the problem of respiratory droplet spreading, typical approaches found in the current literature are based on large-eddy simulations (LESs) and Reynolds-averaged Navier-Stokes (RANS) equations (see, e.g., Refs. [110, 112]). By definition, LESs and RANS equations only describe turbulent fluctuations at the largest scales involved. On the other hand, the fine structure of turbulence is expected to be crucial to correctly account for its effect on droplet evaporation. This is expected from results in atmospheric cloud microphysics where turbulence is crucial to explain the broadening of the cloud-droplet size spectrum (see, e.g., Ref. [26]). Numerical approaches based on DNS are thus crucial to assess quantitatively how turbulence dictates the fate of virus-containing droplets, and consequently provide useful insights on the spread of SARS-CoV-2 and other airborne transmitted infections.

3.3.1. Coarse-graining approaches

In order to highlight the crucial role of turbulence in the dynamics of expiratory droplets, two additional types of coarse-grained simulations have been performed as detailed in the following of this section.

Filtered DNS

In the so-called filtered DNS, we let the governing equations, i.e., the Navier-Stokes equations for the fluid flow and the advection-diffusion equation for the supersaturation field, evolve exactly as in the fully resolved DNS. However, both in the Lagrangian particle tracking and in the droplet radii evolution equation, Eqs. (3.5)-(3.8), instead of using the actual fluid velocity and/or supersaturation, we make use of their averaged values over a stencil of 7^3 Eulerian grid points surrounding the droplet. As a result, the fine structure of both the velocity and supersaturation fields is washed out.

Mean-field simulation

In this last approach, we first seed the fluid flow with 2×10^4 Lagrangian tracers from which we reconstruct a mean, time-dependent streamwise velocity field (whereas both the spanwise and the vertical components are set to zero because of the symmetry of the problem) and a mean, time-dependent supersaturation field of the turbulent puff. Such mean velocity is thus supplied to the Lagrangian particle tracking while the mean supersaturation field is supplied to the droplet radii evolution equation, Eqs. (3.5)-(3.8). Moreover, from the tracer trajectories we also measure the time evolution of the puff size. The latter is used to specify at each iteration whether the droplet resides inside or outside the puff. In the first case, we apply the described mean fields; conversely, outside the puff we impose $s = s_a$ and $\mathbf{u} = 0$.

3.3.2. The role of turbulence in the airborne transmission

As a first step in our analysis, we provide an overview of the observed dynamics by quantifying the number of airborne transmitted droplets and of those settling on the ground. Such information is reported in Fig. 3.6 from which we clearly observe that the number of sedimenting droplets represents only a tiny fraction (around 5%) of the total number of exhaled droplets. Sedimenting droplets have larger size and are characterized by a ballistic like trajectory, due to the fact that the effect of gravity largely dominates the action exerted by the flow. Because the dynamics of these droplets is ballistic, the focus will be only on the behavior of airborne transmitted droplets, with particular attention to the role of turbulent fluctuations both in their dispersion and evaporation process.

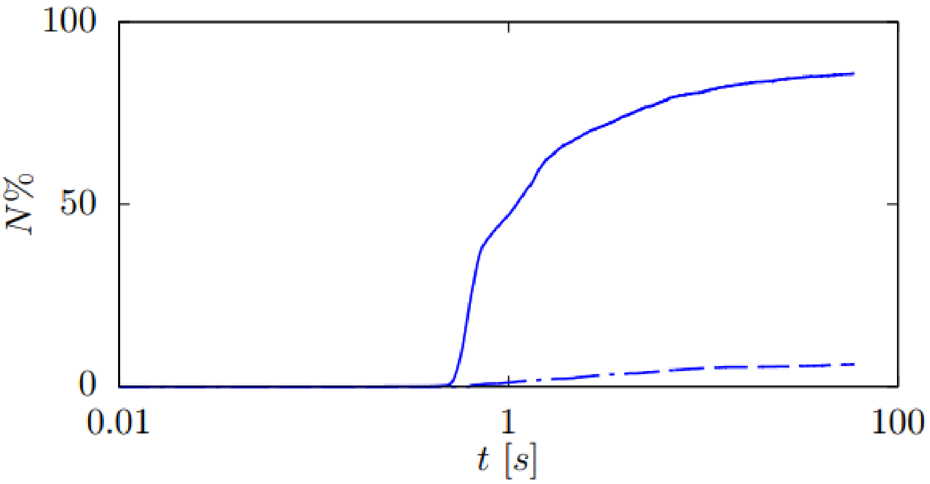

Figure 3.6: Time history of the percentage number of droplets settling on the ground (dashed line) vs those remaining airborne and reaching 1m from the mouth (solid line).

Because the supersaturation field evolves as a passive scalar in a turbulent field, it exhibits the well-known "plateau-and-cliff" structures [131]. Namely, the scalar field displays dramatic fluctuations occurring in small regions (called cliffs or fronts) separating larger areas where the scalar is well mixed (called plateau). Because airborne droplets and supersaturation are transported by the same velocity field, correlations occur between droplet trajectories and supersaturation values [26]. This phenomenon causes droplets of sufficiently small size to remain long in the large well-mixed regions where they can equilibrate with the (local) value of the supersaturation. The droplet evaporation process is thus expected to behave in time by alternating phases of equilibrium with phases of rapid evaporation, i.e., a sort of stop-and-go process. The same type of structure is also expected for the decay of droplet radii. This phenomenon can be clearly detected in Fig. 3.7 where the temporal behavior of the supersaturation field along the Lagrangian trajectory of a small airborne droplet is reported (group of lines denoted by $St < 1$) together with the time evolution of the corresponding droplet radius (see the inset of Fig. 3.7). The time history with the fully resolved DNS (solid blue line) clearly shows the effect of the plateau-and-cliff structures on the evaporation process, which is, however, absent for the larger

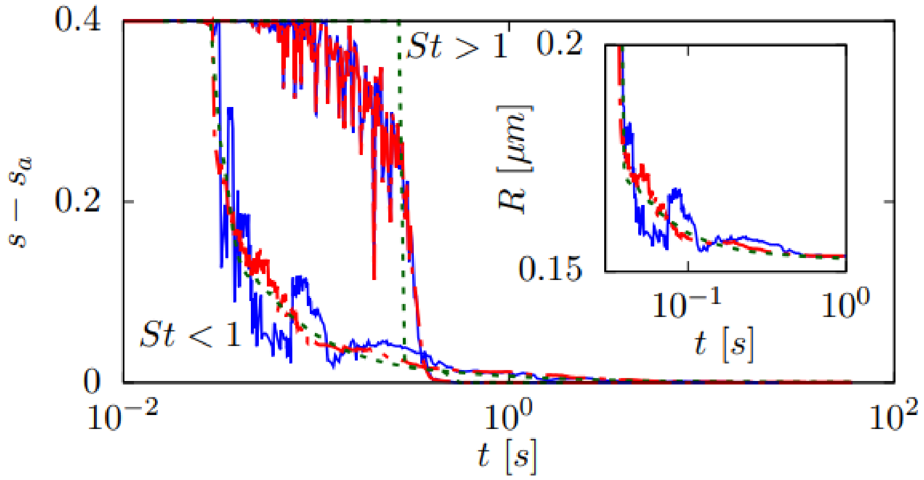

Figure 3.7: $s - s_a$ as a function of time experienced by two representative droplets in the DNS (solid blue line), filtered DNS (long-dashed red line), and mean-field simulation (dashed green line). The group of three curves close to the bottom left corner of the figure corresponds to a “small droplet” having an initial radius of 0.6×10^{-6}m and a Stokes number always smaller than 0.004 during the whole droplet evolution (referred to as $St < 1$ in the figure). The group of three curves in the upper part of the main figure corresponds to a “large droplet” having an initial radius of 0.8×10^{-3}m and a Stokes number always larger than 3 during the whole droplet evolution (referred to as $St > 1$ in the figure). The inset shows the radius time evolution of the “small droplet.”

sedimenting droplet (group of lines denoted by $St > 1$). The fact that the radius closely follows the temporal behavior of the supersaturation field (inset of Fig. 3.7) is the signature of a quasiadiabatic picture for the evaporation process (i.e., the process of radius adjustment due to evaporation is much faster than the corresponding variation of the supersaturation field). It is worth noting that if one considers the smaller droplet evolving in coarse-grained fields (long-dashed line in red, where both velocity and supersaturation have been coarse grained in space as discussed in Sec. 3.3.1.), the effect of the plateaus-and-cliffs structures on the evaporation process reduces, and eventually vanishes when the turbulent fields are replaced by their mean-field components (dashed green line).

Having shown that sufficiently small droplets correlate with the supersaturation field, let pass now to discuss the consequences on droplet motion. For smaller droplets remaining for a sufficiently long time in regions where the supersaturation field is locally constant, with a value larger (smaller) than the mean, the evaporation takes place more slowly (rapidly) than what it would be for the same droplet experiencing smoother fluctuations as in the filtered DNS or in the mean field approach. The two effects, i.e., reduction vs increase in evaporation time, are, however, not symmetric as a consequence of a positive skewness observed in the probability density function of s', the turbulent fluctuation of the supersaturation field. As shown in Fig. 3.8, a positive skewness is accompanied by a zero-mean value of s'. The net result caused by turbulent fluctuations of the supersaturation field on the fate of small droplets is thus to increase their evaporation time. Evidence of positive skewness has been reported for scalar concentration emitted by point sources within atmospheric turbulent flows [132].

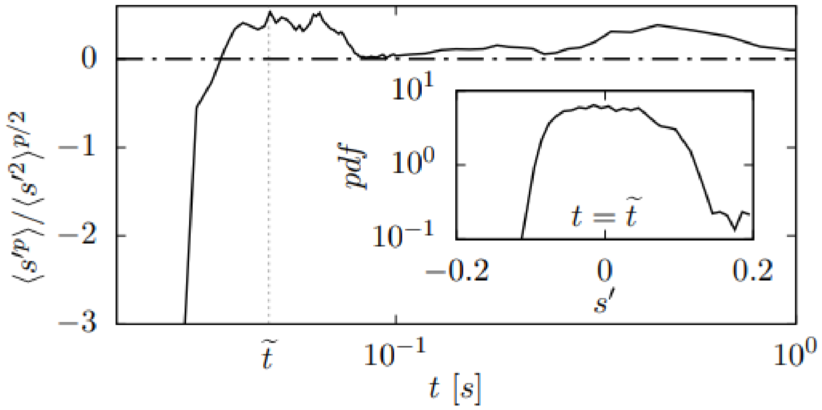

Figure 3.8: Skewness ($p = 3$, solid line) and mean value ($p = 1$, dot dashed line) of the supersaturation turbulent fluctuation s'. Inset: The probability density function of s' at the time $\tilde{t} = 0.05$s. Note the change of sign from negative to positive skewness passing from the jet to the puff phase.

Let us now quantify the delay caused by turbulence in the evaporation process by comparing, for an observation time of 60s, the time it takes for each airborne droplet to shrink to its final equilibrium radius. Let us denote those typical evaporation times as τ_{evap}. All droplets which sedimented within the observation time of 60s were not included in this analysis. The sole airborne droplets were selected here, thus automatically satisfying the requirement of having a sufficiently small radius.

The results are presented in Fig. 3.9, where the probability density functions of τ_{evap} are reported both for the fully resolved case and for the evolution with the sole mean fields (of both the carrying flow and the supersaturation field) and with the filtered DNS. The corresponding mean evaporation times are reported in Table 3.2. The role of turbulence clearly emerges, both causing delay of the evaporation process and broader probability density functions, the fingerprint of fluctuations.

Table 3.2: Droplet mean evaporation times calculated from the probability density functions of Fig. 3.9

Simulation type	DNS	Filtered DNS	Mean field
$\langle \tau_{evap} \rangle (s)$	0.4	0.3	0.2

Importantly, the observed delay in the evaporation significantly affects droplet motion. This is depicted in Fig. 3.10, where it is reported the streamwise coordinate of the center of mass of the cloud of airborne droplets, $x(t)$, as a function of time. Shown in this figure are the fully resolved DNS, the filtered DNS, and the mean-field approach. In the two cases where turbulent fluctuations are either coarse grained or entirely neglected, droplets travel further than in the fully resolved DNS. This is the fingerprint of the reduced inertia of the droplets evolving in the filtered fields. In the initial stage of their evolution, these droplets are indeed spuriously lighter than the droplets evolving in the fully resolved DNS. Being lighter, they are carried more efficiently by the underlying rapidly accelerating flow thus reaching longer distances before touching the floor. Note also that all the curves show a pronounced S-shaped kink which reflects

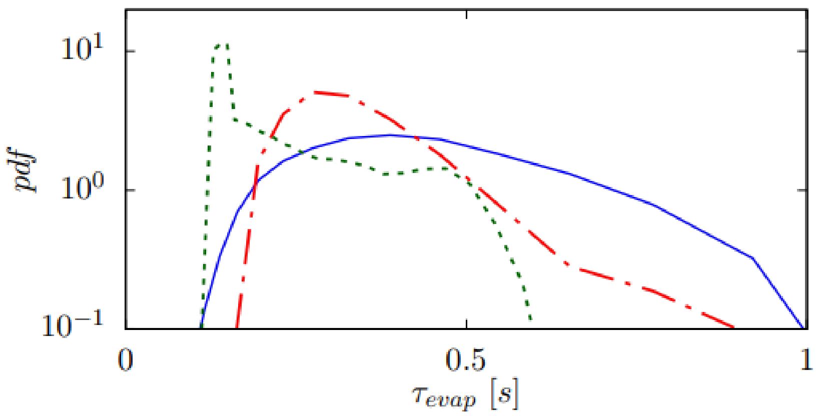

Figure 3.9: Probability density function of the time for each airborne droplet to shrink to its final equilibrium radius for the DNS (solid blue line), filtered DNS (long-dashed red line), and mean-field simulation (dashed green line). Only airborne particles in the observation time of 60s are considered.

the rapid evaporation of relatively large droplets exiting from the puff, resulting in a sudden reduction of the total mass of the droplet cloud.

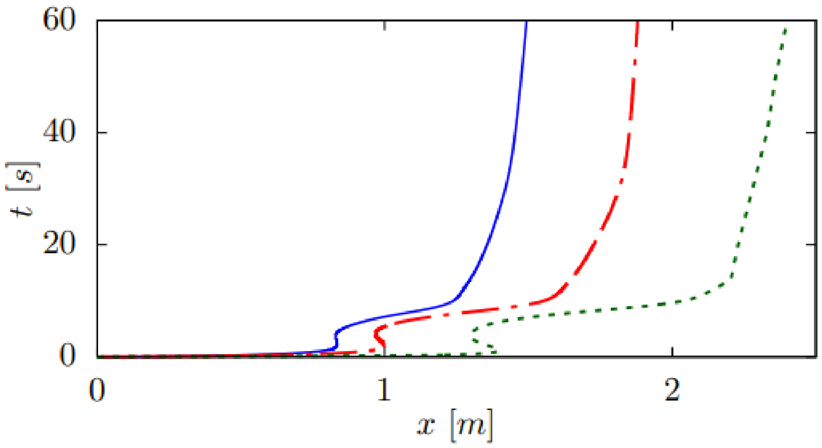

Figure 3.10: The streamwise coordinate, $x(t)$, of the center of mass of the cloud of airborne droplets. Solid blue line, DNS; long-dashed red line, filtered DNS; dashed green line, mean-field simulation.

In order to ascertain whether the observed delay of trajectories of small droplets is a genuine effect caused by the interplay between turbulence and inertia, a subset of idealized simulations have been performed where monodisperse droplets of $R_i(0) = 5\mu\text{m}$ are considered, with and without inertia, i.e. simply switching on or off the inertia in the ruling equations (3.5) and (3.6). This size is close to the peak of the droplet size distribution we have used in the previous analysis [115], and corresponds to droplets that are neither too large to be insensitive to turbulence, nor too small to make the mass loss due to evaporation negligible.

The results are shown in Fig. 3.11. Both in the presence and in the absence of droplet inertia we found the turbulence induced broadening of the probability density functions of the

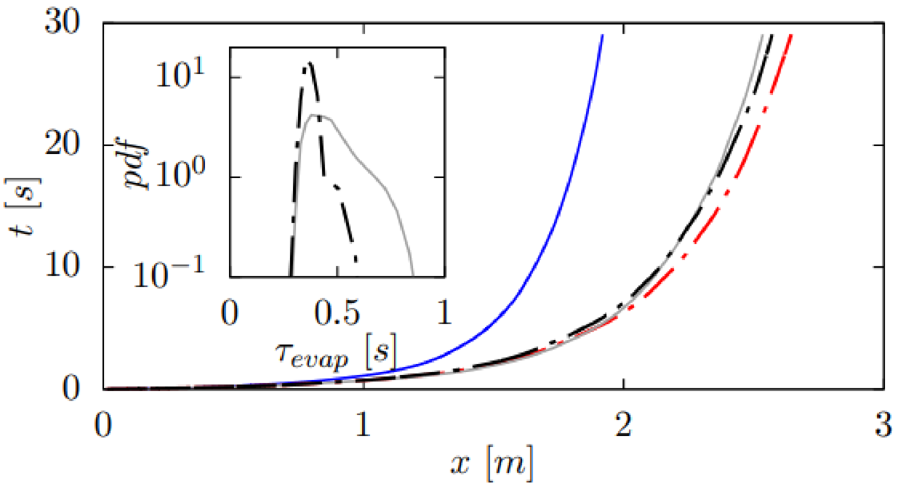

Figure 3.11: The streamwise coordinate, $x(t)$, of the center of mass of the cloud of airborne droplets. Results refer to the simulations for the monodisperse droplets of initial radius $R_i(0) = 5\mu\text{m}$ with and without inertia in the droplet ruling equations. Main frame: Inertia causes differences in droplet trajectories. DNSs with (without) inertia are represented by the solid blue (gray) curve, filtered DNSs with (without) inertia by the long-dashed red (black) curve. Inset: Turbulence causes the observed broadening of evaporation times. The probability density function of the evaporation time τ_{evap} without inertia for the DNS (solid gray curve) and for the filtered DNS (long-dashed black curve).

evaporation time. This is shown in the inset of Fig. 3.11 for the simulations without inertia. Filtering the turbulence fluctuations (long-dashed black curve in the inset) reduces the broadening as observed for the polydisperse case with inertia. It is now worth remarking that the observed difference between the mean evaporation time measured from the DNS and the one measured from the filtered DNS does not produce any relevant effect on the droplet motion when inertia is switched off in the droplet ruling equations. The similarity in the main frame between the solid gray curve and the long-dashed black curve confirms this fact. Switching on inertia, the effect of the delayed evaporation in the DNS case becomes apparent (see in the main frame the differences between the solid blue curve and the long-dashed red curve). Figure 3.11 confirms that turbulence is the root cause of the broadening of evaporation times, whereas inertia causes differences in the trajectories.

3.4. Urgent data for a scientific design of social distancing

Having understood the main physical mechanisms at play determining determining the fate of virus-containing droplets, let us now to discuss issues related to the impact of virus spreading on the society. More specifically, in this section we show how a single rule for social distancing may not be adequate to protect individuals in different environments. It is well known that SARS-CoV-2 infection relies on the spreading of small virus-containing respiratory droplets that the infected person exhales when coughing or sneezing or even simply talking or breathing [133]. However, at least two unresolved key issues (I1 and I2 in the following) remain open and need urgent attention. First (I1): we need to better characterize the sizes of the exhaled droplets for all the expulsion processes, coughing, speaking, breathing and sneezing. Flügge [134] and Wells [135] have highlighted the importance of this issue. Wells [135] and Duguid [115] were the first to propose systematic measurements of droplet sizes. A careful analysis of the state of the art on the subject reported in Seminara et al. [136] shows broad differences in the experimental results of the different investigators. For example, Zayas et al. [137] state that the droplets in the sub-micron range represent 97% of the exhaled droplets for each single cough event; for the same type of expulsion, Yang et al. [138] report a much smaller percentage of less than 4% while not even a single droplet within this subrange was measured by Duguid [115]. Moreover, experiments exploit different techniques under different ambient conditions. Finally, a rigorous presentation of data is not always provided. This lack of a systematic analysis, in addition to the natural variability across individuals, may explain the striking inconsistency of available information on the size distribution of exhaled droplets.

Second (I2): we need to establish whether viruses lingering on dry nuclei upon droplet evaporation retain their full potential of infection. There is evidence supporting that viruses coated by a lipid membrane tend to retain their infectivity longer at low relative humidity [139].

Current guidelines released by WHO for the protection from airborne virus transmission introduce the notion of a safe distance of $1 - 2\mathrm{m}$ to ensure protection from an infected individual. In the present section it is discussed the scientific foundation of these "social distancing" measures, which touches several billion individuals globally. It will be shown that diametrically opposed predictions are drawn depending on the size distribution of the respiratory droplets and ambient humidity.

3.4.1. Droplets sizes and ambient humidity effect

Let us now discuss how predictions vary across different scenarios for I1 and I2. To do that we quantify the viral load carried on dry nuclei versus liquid droplets upon cough. We leverage concepts developed in the context of atmospheric cloud formation to track the evaporation of respiratory droplets as they move away from the mouth (Fig. 3.12). To simultaneously monitor droplet position and evaporation it has been employed massive state-of-the-art direct numerical simulations (DNS) of the airflow and humidity (as done in Sec. 3.3.).

To quantify these observations we define the (relative) viral load of the $i\mathrm{th}$ droplet as the ratio between its initial volume and the cumulative initial volume of all exhaled droplets. In other words, we assume that the viral load of a given droplet is proportional to its initial volume and when the droplet undergoes evaporation the viral load is conserved (i.e. any degradation of the virus is neglected). This assumption is sensible in view of the recent findings by Fears et al. [140] showing that the SARS-CoV-2 virus retains infectivity and integrity up to 16 hours in laboratory-created respirable-sized aerosols.

Here a systematic comparative analysis across eight scenarios selected from the literature [115, 124, 138, 141] is presented. We conduct eight numerical experiments considering two different levels of ambient relative humidity ($RH = 60\%$ prefix ”Wet” and $RH = 40\%$ prefix ”Dry”) combined with four different initial size distributions of the exhaled droplets. The ”Wet” condition lays above the efflorescence RH, namely droplets never evaporate completely but remain in the liquid state in equilibrium with the surrounding ambient humidity. Conversely, our ”Dry” condition is below the efflorescence RH hence all droplets eventually evaporate completely and shrink to their dry nuclei. We simulate the ”Dry” and ”Wet” conditions for four different droplet size distributions (Fig. 3.12a) proposed by Duguid [115] (suffix ”Du”), by Johnson et al. [124] (suffix ‘Jo’), by Xie et al. [141] (suffix ‘Xi’), and by Yang et al. [138] (suffix ”Ya”). Te eight experiments are labeled: WetDu, WetJo, WetXi, WetYa, and similarly for the ”Dry” condition.

A snapshot of droplet positions demonstrates the undeniable role of droplet size at emission (Fig. 3.12b). The distribution of droplet sizes from Duguid [115] (Fig. 3.12b top) yields a scenario largely consistent with the literature [142], where droplets belong to either of two classes. Large droplets sediment owing to their weight with negligible action of the airflow (phase I in Fig. 3.12b top); small droplets remain airborne and travel within the turbulent puff (phase II in Fig. 3.12b top); after few seconds they reach their minimum size and they are carried as tracers by the airflow (phase III in Fig. 3.12b top). But a different distribution of droplet sizes, Yang et al. [138], yields an entirely different picture (Fig. 3.12b bottom): there are no large droplets, and the entire viral load is carried on small airborne droplets that never settle in our simulation.

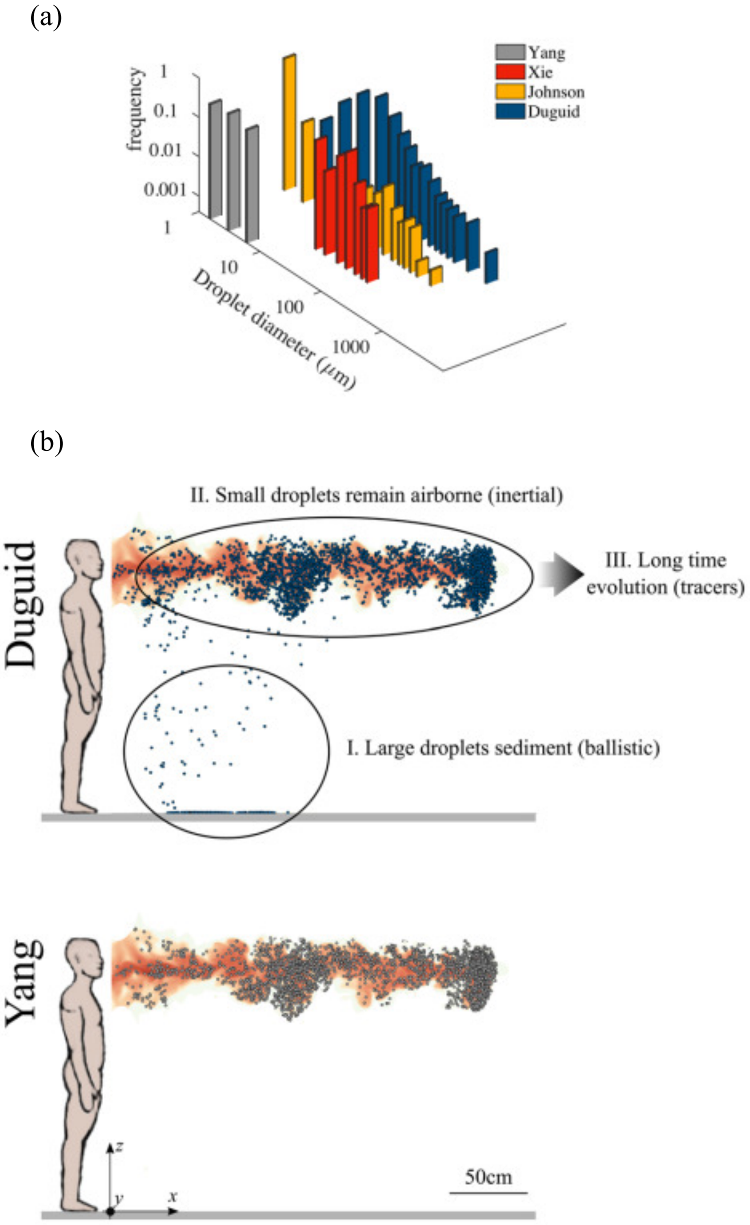

Figure 3.12: (a) Droplet initial size distributions considered in the present study: Duguid [115] (blue), Johnson et al. [124] (yellow), Xie et al. [141] (red), Yang et al. [138] (gray). (b) Relative humidity (color coded) and exhaled droplets (blue and gray spheres, not in scale) after 7.6s considering two different initial droplet size distributions: (top) Duguid [115]; (bottom) Yang et al. [138] showcases the dramatic differences in predictions depending on the initial distribution of droplet sizes. The distribution of droplet sizes from Duguid [115] contains large droplets that rapidly settle carrying most viral load on the ground, as well as many small droplets which remain airborne. In contrast, in the size distribution from Yang et al. [138] all droplets are small enough to remain airborne for the entire simulation. The ambient RH_a is 60% in all figures. Scale bar: $50\mathrm{cm}$.

Loss of viral load via sedimentation to the ground (ballistic)

In the first few seconds after exhalation, the puff rapidly loses viral load carried by larger droplets that reach the ground owing to their own weight. The amount of viral load lost through sedimentation depends dramatically on the ambient humidity and the initial distribution of droplet sizes (issue I1). For three initial conditions, nearly the entire viral load is carried to the ground after 1 to 3s (99% for the Du and Jo distributions and 45% for Xi); whereas for the last condition (Ya), exactly zero viral load reaches ground for the entire simulation (Fig. 3.13a,b). The inconsistency among predictions for the four size distributions is even more pronounced in the dry cases reported in Fig. 3.13b (Du: 94%; Jo: 61%; Xi: 12%; Ya: 0%). A summary of the cumulative viral load sedimenting to the ground after the entire simulation (60s) is reported in Table 3.3 (VL – sed).

The table additionally shows a different observable, often discussed in the literature: the number of sedimenting droplets normalized to the total number of droplets (ND – sed). Using this variable can be extremely misleading in the presence of very large droplets as these may be a negligible fraction of the total number of droplets but nonetheless carry nearly the entire viral load owing to their large volume. This is the case for the Du and Jo distributions, for which most viral load settles to the ground carried by few large droplets, yet more than 90% of the droplets are small and still remain aloft.

	WetDu	DryDu	WetJo	DryJo	WetXi	DryXi	WetYa	DryYa
ND – sed (%)	6	3	5	3	71	45	0	0
ND – 1m (%)	85	90	87	91	24	86	93	93
ND – 2m (%)	45	47	48	50	8	32	51	50
ND – 4m (%)	8	9	9	10	1	5	10	11
ND – 1m, small (%)	85	89	86	89	19	46	93	93
ND – 2m, small (%)	45	46	48	49	8	21	51	50
ND – 4m, small (%)	8	9	9	10	1	4	10	11
VL – sed (%)	99	99	99	95	99	88	0	0
VL – 1m (%)	5	3	26	15	26	60	92	92
VL – 2m (%)	0.1	0.6	0.01	2	0.2	13	51	49
VL – 4m (%)	0.02	0.07	0.0001	0.08	0.03	1	10	10
VL – 1m, small (%)	0.3	1	0.08	3	0.6	7	92	92
VL – 2m, small (%)	0.1	0.4	0.01	1	0.2	3	51	49
VL – 4m, small (%)	0.02	0.05	0.0001	0.08	0.03	0.6	10	10

Table 3.3: The cumulative number of droplets (ND) and viral load (VL) measured in the numerical experiments. Note that all the values are given in percentage. Quantities denoted with ”sed” correspond to droplets that settle on the ground within the simulation; Quantities denoted with ”1m”, ”2m” and ”4m” correspond to airborne droplets traveling up to distances of 1, 2 and 4 metres respectively; Quantities denoted with ”small” correspond to to droplets with diameter smaller than $10\,\mu\mathrm{m}$.

To complement this analysis, Fig. 3.13c shows the normalized histogram (probability density function or *pdf*) of the distance traveled by these large droplets when they reach ground, comparing the two ambient conditions for one size distribution (Du). The effect of the ambient humidity is clearly noticeable, with large droplets settling within $1\mathrm{m}$ in the Wet condition versus almost 3m in the Dry condition. Similar results hold for the other size distributions except for Ya for which all droplets remain airborne.

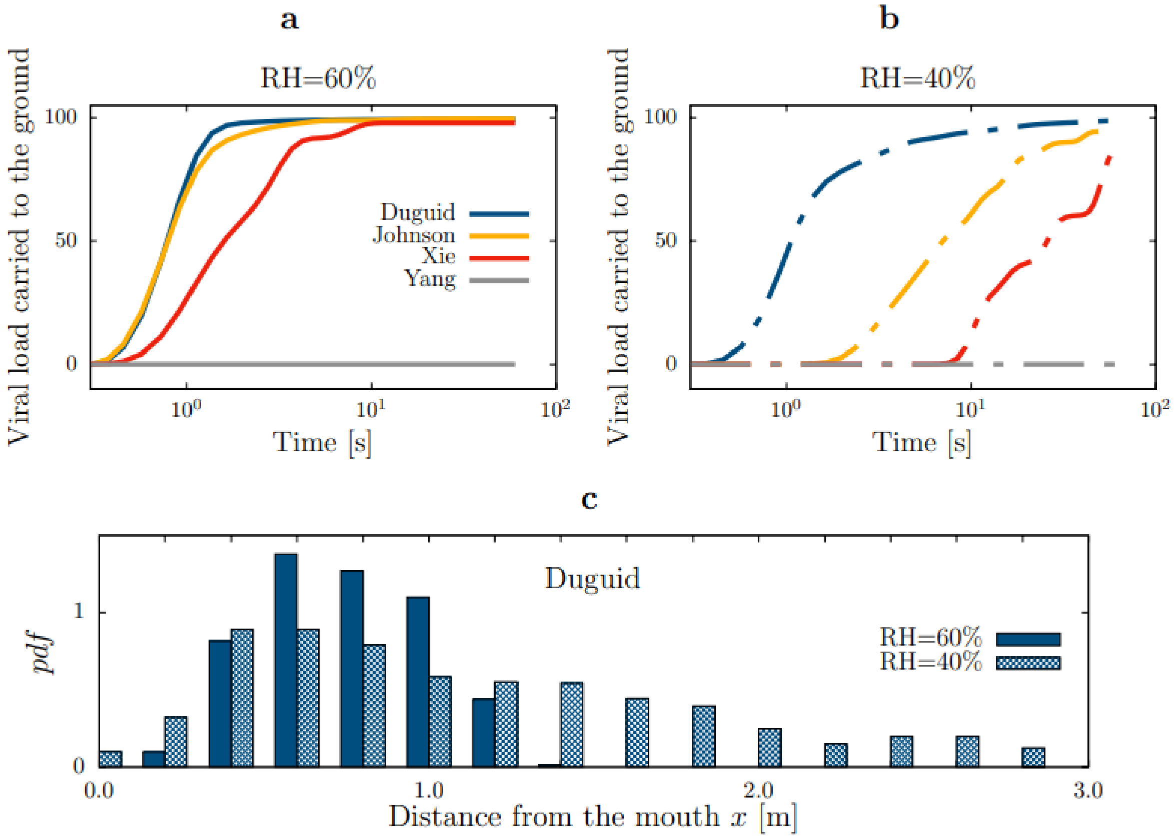

Figure 3.13: Sedimentation of large droplets. (a) Cumulative viral load sedimenting to the ground, obtained with the four different initial droplet size distributions proposed by Duguid [115] (blue), Johnson et al. [124] (yellow), Xie et al. [141] (red) and Yang et al. [138] (gray). Here, the ambient relative humidity is $RH = 60\%$. (b) Same as (a), for a dry environment, $RH = 40\%$. Most of the viral load settles within 60s for three initial distributions, whereas for one, Yang et al. [138], no droplets settle within the simulation time. (c) Probability density function of the distance from the mouth when droplets reach the ground; ambient relative humidity $RH = 60\%$ (solid blue) and $RH = 40\%$ (patterned blue). Drier environments cause further spreading: Droplets that reach the ground remain within 1m from the mouth in wet conditions, whereas they can reach nearly 3m in dry conditions.

Transport of airborne droplets (inertial)

Te fate of smaller droplets is dictated by the interplay between their inertia and the airflow, and thus it depends critically on droplet initial size and subsequent evaporation. Once again we find radically different predictions for the viral load carried by airborne droplets depending on the ambient relative humidity and initial droplet size distribution. The discrepancy in the predictions can be appreciated qualitatively in Fig. 3.14a,d where we map the cumulative viral load per unit area that travel across a vertical plane at $2\mathrm{m}$ from the mouth in the entire simulation. In the DryYa condition, considerable viral load reaches beyond $2\mathrm{m}$ from the mouth in $60\mathrm{s}$ (see Fig. 3.14a and Table 3.3, total 49%), whereas nearly no viral load travels the same distance in the DryDu condition (total 0.6%). Fig. 3.14d showcases the dramatic effect of the ambient humidity for one initial droplet size distribution (Du).

Synthetic data are summarized in Table 3.3, where we report the cumulative viral load carried by airborne droplets reaching a distance of $1\mathrm{m}$ (indicated as ”VL – 1 m”), $2\mathrm{m}$ (”VL – 2 m”) and $4\mathrm{m}$ (”VL – 4 m”) from the mouth within the total observation time of $60\mathrm{s}$. Predictions vary dramatically depending on the relative humidity and the initial droplet size distribution. E.g. as much as 10% (DryYa) or as little as $10^{-4}\%$ (WetJo) of the viral load travels $4\mathrm{m}$ or more from the mouth in $60\mathrm{s}$. Importantly, similar uncertainties persist also when considering only droplets that are smaller than $10\mu\mathrm{m}$ (see results labeled ”VL – 1 m, small”, ”VL – 2 m, small” and ”VL – 4 m, small” in Table 3.3). These droplets are candidate to reach pulmonary alveoli causing the most severe complications of COVID-19 [127] and their initial volume affects predictions of airborne infection risk models (see e.g. the model proposed by Nicas et al. [127] and its Eq. 1). Hence the uncertainty in the initial droplet size distribution (I1) affects dramatically the reliability of airborne infection risk models.

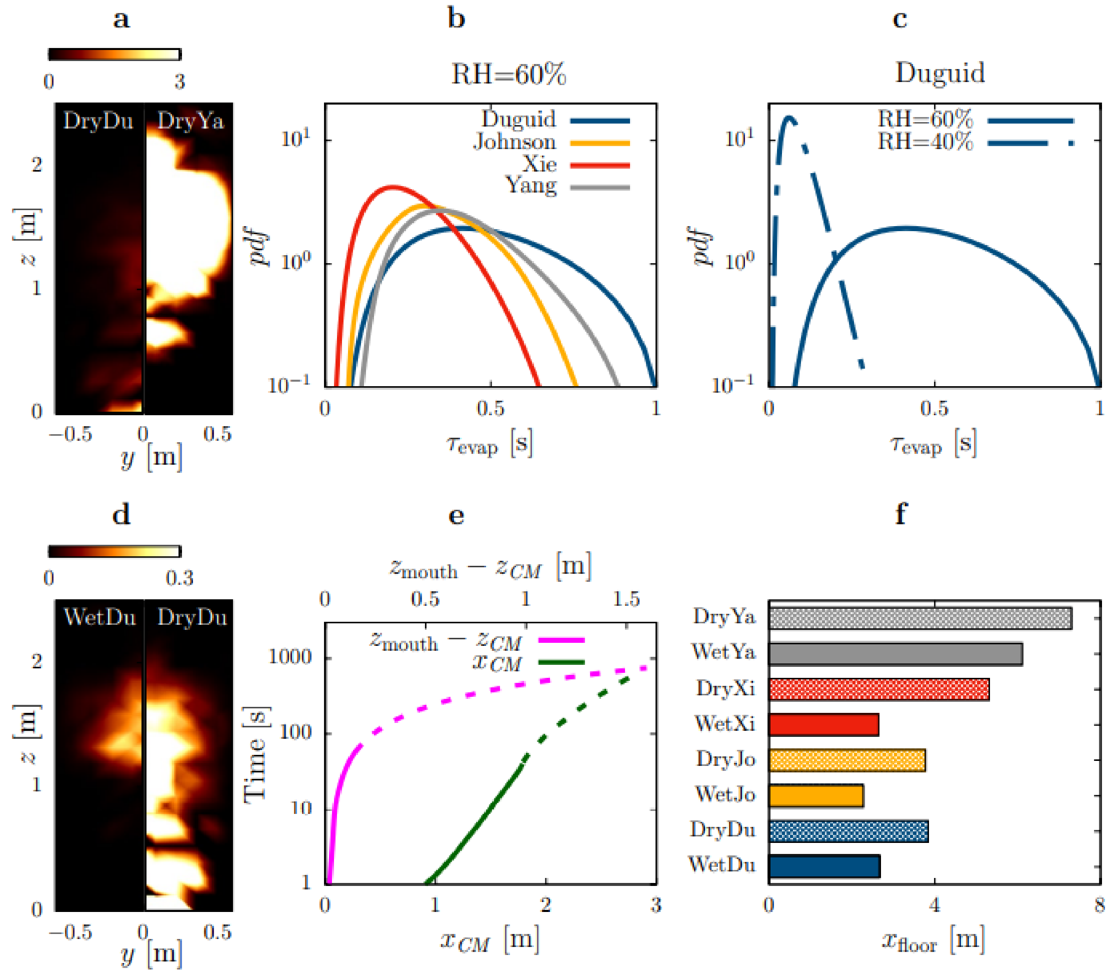

Figure 3.14: Airborne-transmitted droplets. (a, d) Cumulative viral load per unit area (% viral load/m^2) reaching a distance of 2m from the mouth after 60s. Results obtained with $RH = 40\%$ using the distribution by Duguid [115] and Yang et al. [138] (a left and right respectively) and using the distribution by Duguid [115] with $RH = 60\%$ and 40% (d left and right respectively). (b, c) Probability density function of droplet evaporation time (i.e. time for the droplet to shrink to its final radius; only airborne droplets in the observation time of 60s are considered). (b) Results with ambient $RH = 60\%$ for the four different initial droplet size distributions, i.e. Duguid [115] (blue), Johnson et al. [124] (yellow), Xie et al. [141] (red) and Yang et al. [138] (gray). (c) Results for the distribution by Duguid [115] with ambient $RH = 60\%$ (solid) and $RH = 40\%$ (dashed). The initial size distribution and the ambient humidity cause dramatic differences in the reach of airborne droplets, with variations of the order of 80% for the mean value. (e) Trajectory of the viral load center of mass (computed considering only the airborne droplets and not those that already settled on the ground) for the simulation labeled WetDu; horizontal position x_{CM} (green) and vertical position z_{CM} (magenta). The solid lines indicate the results from the simulation while the dashed ones are extrapolations over longer time using Eq. (3.16). (f) Extrapolated horizontal distance traveled by the viral load center of mass for the eight numerical experiments performed.

Long-range transmission (tracers)

Let us continue analyzing the journey of the airborne droplets proceed after the end of our simulations. After few seconds, all droplets are either liquid at their final equilibrium size ($RH = 60\%$) or shrinked to their dry nucleus ($RH = 40\%$); either way, they behave as fluid tracers. Their final destination depends on the external airflow hence on the specific indoor or outdoor environment and its aeration. In order to provide a simple estimate for the ultimate reach of the viral load, we ignore the presence of external airflow and we track the center of mass of the airborne viral load in time excluding the sedimenting droplets (see Fig. 3.14e for a typical trace). We extrapolate the trajectory to the location where the center of mass eventually reaches the ground (see Fig. 3.14f and Eq. (3.16)). This simple estimate shows that even in the absence of external airflow, small droplets travel several meters. Once again we observe a remarkable variability: while for WetJo the spreading is contained in less than $2.5\mathrm{m}$, for DryYa droplets travel beyond $7.5\mathrm{m}$. Airborne droplets reach the foor in about 20 min which is well within the 16 hours of virus survival recently measured by Fears et al. [143]. Note that in the Dry condition, the viral load reaches the floor on dry nuclei because droplets fully evaporate, whereas in the Wet condition viruses travel on droplets that retain their liquid content. Once again, the two issues I1 and I2 are crucial to establish the reach and infectious potential of droplets expelled in a cough.

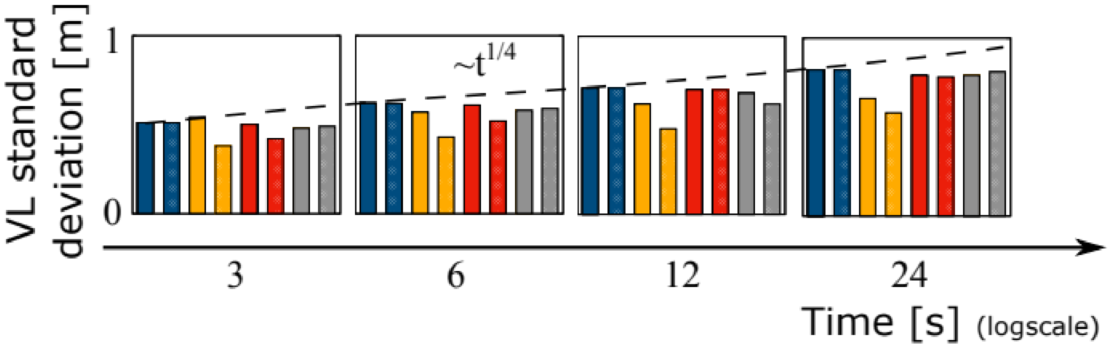

Figure 3.15: Time evolution of the viral load standard deviation for the eight numerical experiments performed. The dashed line represents the expected power-law growth predicted by means of phenomenological arguments (see Sec. 3.2.1.) The variability observed for the standard deviations associated to different initial droplet size distributions reaches values of about 30%.

Another important observable is the concentration of infectious material, which is inversely proportional to the volume of the cloud of droplets. The cloud expands at a rate that is intertwined with the turbulent nature of the cough. When droplets are shrunk to their final size and closely follow the airflow, the size of the cloud grows as $t^{1/4}$ (see Sec. 3.2.1.). This scaling holds for all our simulations at long times, as it is a fundamental property of the turbulent airflow generated by the cough. However, prior to this regime, most droplets are inertial and they follow the flow with delays that depend on their size. Hence the cloud of droplets expands at a rate that depends on droplet size distribution and evaporation. This regime is extremely complex and requires an in depth description of turbulent fluctuations. Indeed, the interaction between inertial effects and turbulence causes nontrivial correlations and ultimately slows down evaporation (see Sec. 3.3.). The distribution of evaporation times resulting from these non-trivial effects varies considerably across different conditions (Fig. 3.14b,c). In our simulations, the droplet cloud expands at different rates depending on the initial condition (see Fig.3.15). Although variations are sizeable (about 30%), they are overshadowed by the much more dramatic variations in the position of the center of mass (100%).

Estimation of the viral load landing distance. We estimate the distance from the mouth reached by the airborne droplets in the absence of external flows (depicted in Fig. 3.14f) as follows. First, we evaluate the settling velocity from Fig. 3.14e which clearly shows (when observed in linear scale) a linearly decreasing height of the viral load center of mass. From the same figure, we also obtain the time needed for the center of mass to reach the ground, t_{floor}. We now split the airborne droplets in two groups, those that are inside the puf and those outside. For the former, we estimate the streamwise coordinate of their center of mass, x_{floor}, as

$$x_{floor} - x_{min} = \int_{t_{min}}^{t_{floor}} v dt = \int_{t_{min}}^{t_{floor}} c_1 t^{-3/4} dt = \left[4c_1 t^{1/4}\right]_{t_{min}}^{t_{floor}} = 4c_1(t_{floor}^{1/4} - t_{min}^{1/4}), \quad (3.16)$$

where t_{min} is equal to 45s and corresponds to the maximum simulated time unaffected by boundary condition effects, x_{min} is the streamwise coordinate of the viral load center of mass at time t_{min} for the considered droplets, v is the mean streamwise velocity and $c1 = 1/2.2$ is a prefactor found by fitting the decay of v with $t^{-3/4}$. For the droplets outside the puff, we suppose they settle without changing their streamwise coordinate, such that $x_{floor} = x_{min}$. Finally, the center of mass of the viral load of the entire cloud of droplets has been obtained as the (initial volume) weighted average of the centers of mass of the two groups of droplets.

3.5. Virus-containing droplets exhaled by men and women

This section presents a numerical study on the dispersion of droplets released when coughing with emphasis on the characteristics associated with the gender of the exhaling subject. Previously it has been considered such kind of expiratory event in light of its importance for the effective transmission of virus-laden droplets, focusing on the accurate description of the physical process governing the transport and evaporation of droplets (see Sec. 3.3.) as well as the influence of the droplet size distribution and environmental conditions on the prediction of the final reach by direct (or short-range) transmission (see Sec. 3.4.). The same numerical setup used in Sec. 3.3. has been used to investigate the variability with respect to the human subject during a cough.

The injected airflow is prescribed according to the experimental measurements reported by Ref. [109] and shown in the left panel of Fig. 3.16. The duration of the exhalation is around $0.5\mathrm{s}$ with a peak velocity of $13\mathrm{m/s}$ for the male and of $7\mathrm{m/s}$ for the female subject. The resulting Reynolds numbers (based on the peak velocity and on the mouth average radius) are about 9×10^3 and 5×10^3, respectively. Concerning the initial droplet size distribution, we assume here the one from Ref. [115], still considered as a reference on the subject. Accordingly, we consider initial droplet radii approximately ranging from 1 to $1000\mu\mathrm{m}$ with the 95% falling between 1 and $50\mu\mathrm{m}$. Droplets are set initially at rest and randomly distributed within a sphere of radius $1\mathrm{cm}$ located inside the circular pipe from which the exhaled airflow is released. The size distribution is the same for the male and female case, this choice being justified since for the droplet size distribution no significant differences between male and female subjects are reported in the current literature [124, 138, 141]. Here, $RH_a = 60\%$ is considered.

Fig. 3.17 shows a typical side view of our results obtained after $7\mathrm{m}$ from the respiratory event. The figure clearly shows that the resulting droplet dynamics can be macroscopically classified in two distinct behaviors: i)some droplets leave the humid and turbulent air puff released from the mouth and travel vertically within the still ambient fluid, eventually settling on the ground at a relatively short distance from their emission point, showing a predominantly ballistic motion; ii) other droplets travel for long distance within the humid air forming a cloud of so-called airborne droplets. Although the same general classification can be done for the male and female case, in the latter the distance traveled by both sets of droplets is substantially reduced. To assess the risk of virus transmission, we define the viral load as the ratio between the initial volume of a subset of droplets (e.g., settling or remaining airborne) and the total initial volume of all exhaled droplets. The right panel in Fig. 3.16 shows the mean velocity resulting from our simulations along with the predicted scaling. Differences can be clearly noticed between the male and female case in the initial jet stage (for which we have different inlet velocity profiles), while both cases agree very well with the theoretical decay law from around half second. The different initial jet phase results in a different coefficient for the scaling law, with the male profile following the law $0.45t^{-3/4}$ and the female one $0.19t^{-1/4}$.

Having characterised the main features of the emitted airflow, we now move to the analysis of the droplet transmission mechanisms, focusing at first on the settling droplets. The left panel in Fig. 3.18 shows as a function of time the viral load of settling droplets. We can observe that in the first few seconds after exhalation, the puff rapidly loses viral load carried by large droplets to the ground. For both the male and female subjects, after around $5\mathrm{s}$ approximately

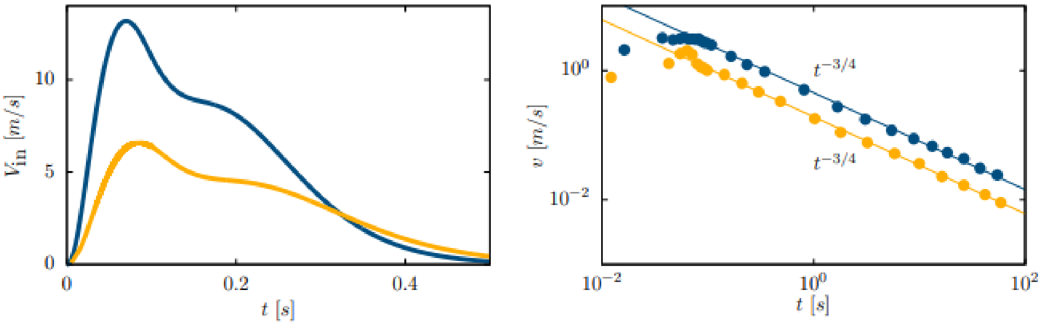

Figure 3.16: (Left) Time-varying inlet airflow velocity of cough according to Ref. [115]. The blue and orange lines are used to distinguish the velocity profiles of a male and female subject, respectively. (Right) Time history of the mean streamwise velocity component v. The lines show the expected scaling while the symbols are the results of our simulations.

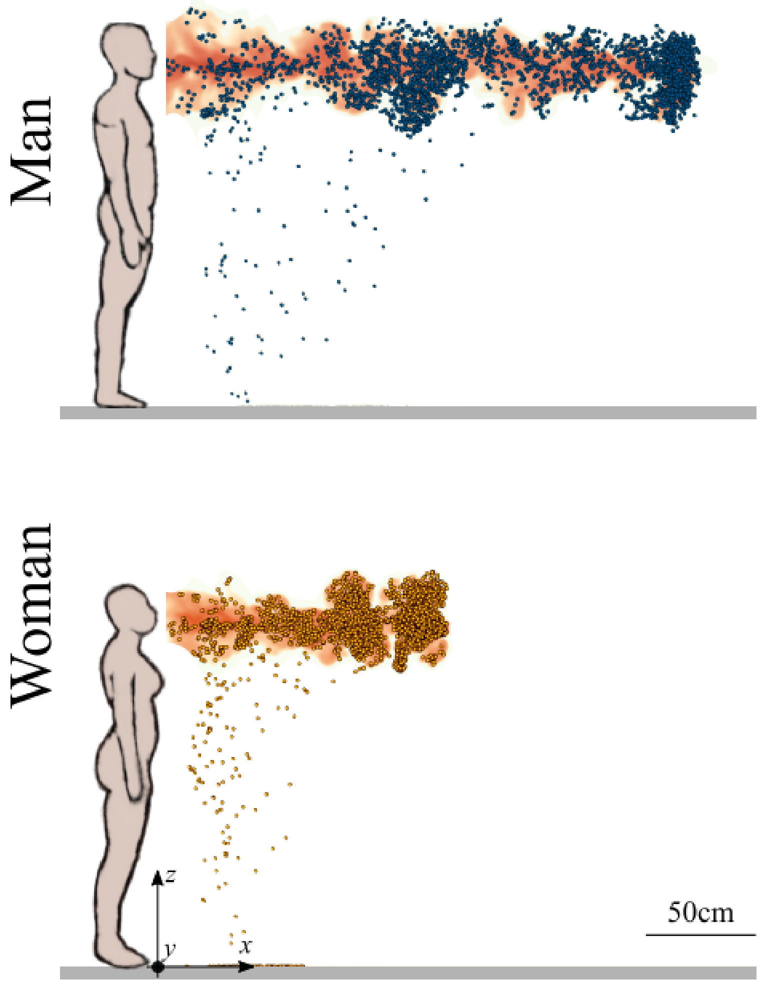

Figure 3.17: Side view of the instantaneous relative humidity field (color coded) and exhaled droplet positions (blue and orange spheres, not in scale) after 7.6s from the starting of cough, for both the male (top) and female (bottom) subject case.

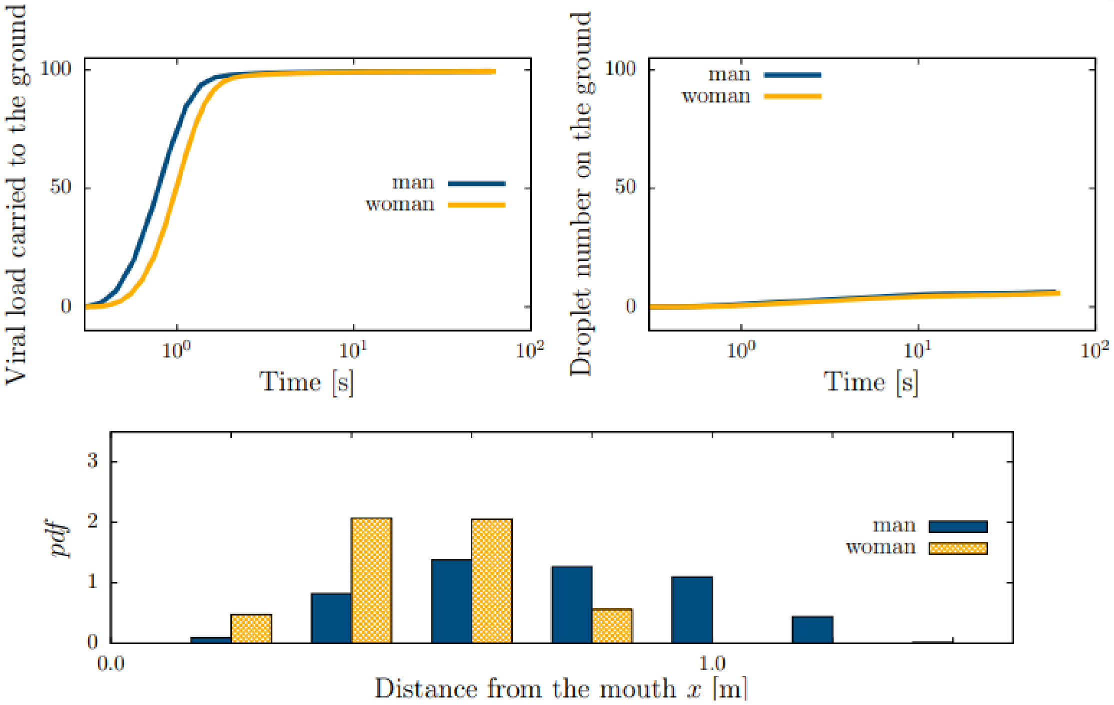

Figure 3.18: Top: Cumulative viral load (left) and normalized droplet number (right) settling to the ground as a function of time (both quantities are expressed as percentage). Bottom: Probability density function of the distance from the mouth when droplets reach the ground. In the figures, the blue and orange colors distinguish the results for male and female, respectively

99% of the viral load has reached the ground; this large percentage is however due to a very small number of droplets, around 5%, as shown in the right panel of Fig. 3.18, thus indicating that 95% of droplets remain airborne after $60\mathrm{s}$ (note that, at this time, all droplets are still within the computational domain). The distance reached by the settling droplets is reported in the bottom of Fig. 3.18 where it is shown the probability density function of the distance traveled by the large droplets when they reach ground. For men, the maximum distance at the ground reached by the large droplets is $1.5\mathrm{m}$, reducing to $1\mathrm{m}$ for women. It is worth noticing that in both cases this distance is within the social-distancing limits suggested by the World Health Organization.

Let us now focus on the smaller droplets that experience airborne transmission. Droplets travel into a non-saturated field and thus evaporate; in Fig. 3.19-left it is reported the temporal evolution of the supersaturation field s sampled along the Lagrangian trajectory of a typical small and large droplets. For the large droplet (dashed lines), we observe that the supersaturation field remains similar to the one inside the mouth for long time, indicating an initial slow dynamics due to the droplet inertia, followed by a rapid decay towards the ambient value as soon as the droplet leaves the turbulent puff. On the contrary, the supersaturation field felt by the small droplet (solid lines) shows the so-called “plateaux-and-cliffs” behaviour, where the scalar field displays dramatic fluctuations occurring in small regions (cliffs) separating larger areas where the scalar is well mixed (plateaux). Because of this, small droplets tend to remain long in the large well-mixed regions where they can equilibrate with the local value of supersat-

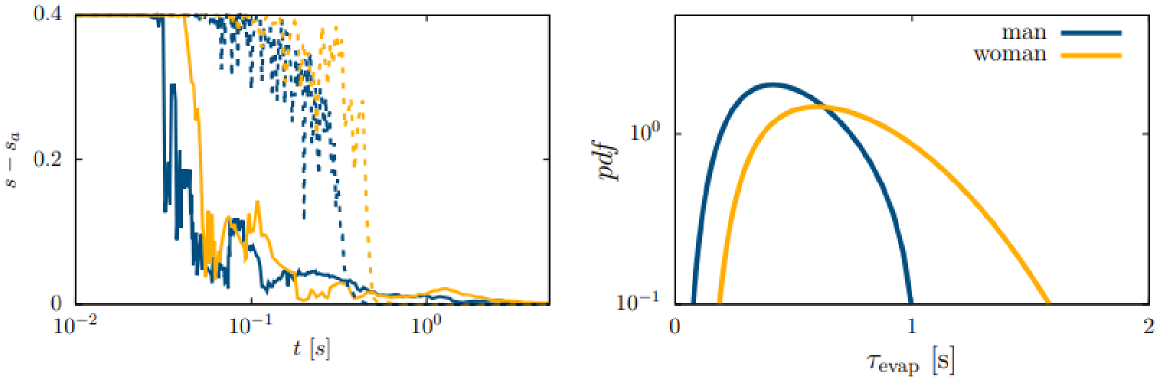

Figure 3.19: (Left) $s - s_a$ as a function of time experienced by two representative droplets. The solid and dashed lines are used to distinguish a small and large droplet. (Right) Probability density function of the droplet evaporation time τ_{evap}, i.e. the time for the droplet to shrink to its final radius. The observation time is 60s.

uration. The resulting dynamical process is thus made, as discussed in Sec. 3.3., of equilibrium phases alternating with phases of rapid evaporation. Focusing on the influence of the subject gender, the same behavior can be observed for both men (blue) and women (orange), with the latter showing an overall delay in the dynamics due to the reduced velocity of the exhaled airflow.

The delay in the dynamics for the female subject in turns affects the evaporation process. We thus quantify this feature by measuring the time τ_{evap} needed to reach the final equilibrium size for each airborne droplet, as shown in the right panel of Fig. 3.19; in particular, it is reported the probability density function of τ_{evap} for both the male and female case. In general we find broad probability density functions, which is the fingerprint of turbulent fluctuations. However, while for men the mean evaporation time is around 0.4s, with values ranging between 0.1s and 1s, for women it increases to 0.6s, with the tail of the distributions even reaching 1.5s.

As a further consequence, the observed delay in the evaporation significantly affects the droplet motion. Indeed, we find different predictions for the viral load carried by airborne droplets for the two subjects. In particular, the left panel of Fig. 3.20 shows the cumulative viral load per unit area reaching the distance of 2m from the mouth. In the male-subject simulation, considerable viral load reaches the distance covering an area of around 1m in size, while in the female-subject case much less viral load reaches the same distance. To fully quantify the distance traveled by airborne droplets, we track the position of the center of mass of the cloud made exclusively of such subset. For the first 60s we can directly compute this quantity from our numerical results while for longer times we extrapolate the trajectory up to the location where the center of mass eventually reaches the ground (see Eq. (3.16)). It clearly appears that, in the absence of external airflow, small airborne droplets can travel several meters: for both men and women, the cloud reaches the ground in about 20 min; due to the different horizontal speed, however, in the female case the center of mass stops at about 1.5m while in the male case it approaches 3m.

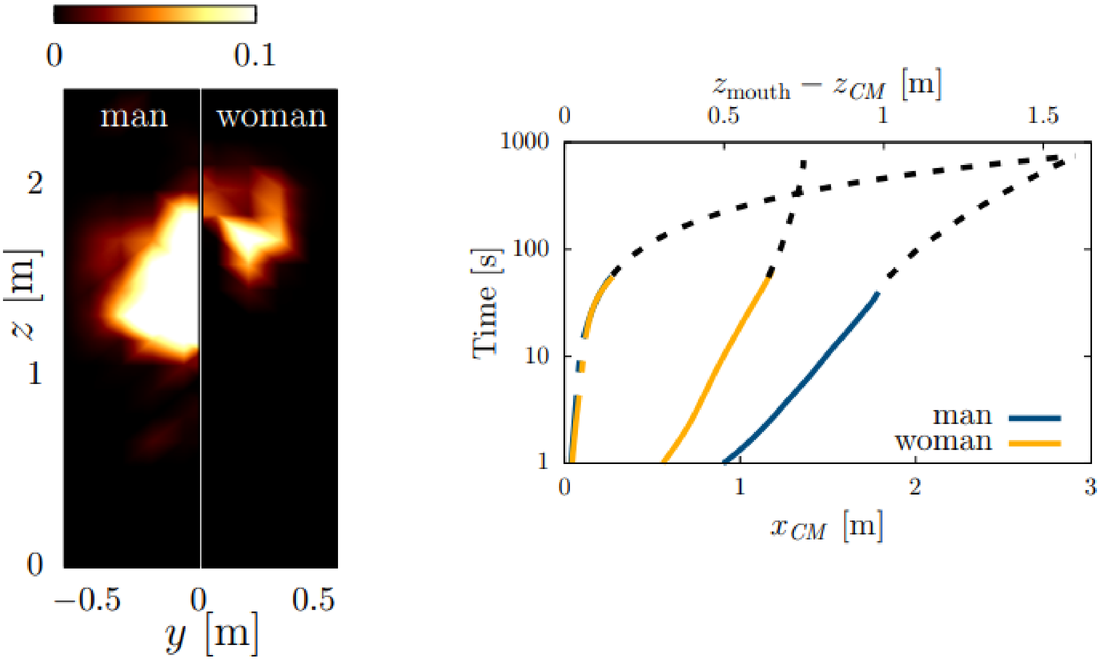

Figure 3.20: (Left) Cumulative viral load per unit area reaching a distance of $2\mathrm{m}$ from the mouth after $60\mathrm{s}$. (Right) Trajectory of the viral load center of mass (computed considering only the airborne droplets): horizontal position x_{CM} (solid line) and vertical position z_{CM} (dash-dotted line). The colored lines indicate the results from the simulation while the black dotted ones are extrapolations over longer times.

3.6. Role of barriers in the spread of virus-containing droplets

This section is dedicated to investigate the effectiveness of the the barriers, one of the many tools for preventing infections, such as COVID-19. Barriers are often used to protect individuals within indoor environments. Numerous devices have been developed and deployed in an effort to protect healthcare workers during high-risk procedures, and in indoor workplaces to protect employees and customers. However, only a few studies have thoroughly and quantitatively examined their impact on the dispersion of droplets and aerosols [144, 145]. The available results show that the placement of large transparent plastic sheets over patients' faces can limit the contamination area [146], showing that such protective tools are helpful in decreasing the contamination from droplet dispersion [147].

To make a step forward in characterizing the efficacy of barriers in the mitigation of airborne transmission, an improvement has been applied to the DNSs employed in Secs. 3.3., 3.4. and 3.5., i.e. the set of the incompressible Navier-Stokes equations are now coupled to the advection-diffusion equation for the temperature field [148]. We are in this way accounting the temperature dependence in the saturated vapor pressure.

3.6.1. Accounting for temperature variations

The fluid flow is now governed by the well-known Oberbeck-Boussinesq equations (i.e., the set of the incompressible Navier–Stokes equations coupled to the advection-diffusion equation for the temperature field) [148]:

$$\partial_t \boldsymbol{u} + \boldsymbol{u} \cdot \boldsymbol{\partial} \boldsymbol{u} = -\frac{1}{\rho} \boldsymbol{\partial} p + \nu \partial^2 \boldsymbol{u} - \beta \boldsymbol{g} (T - T_a), \tag{3.17}$$

$$\boldsymbol{\partial} \cdot \boldsymbol{u} = 0, \tag{3.18}$$

$$\partial_t T + \boldsymbol{u} \cdot \boldsymbol{\partial} T = \kappa \partial^2 T, \tag{3.19}$$

where $\boldsymbol{u}(\boldsymbol{x}, t)$ and $p(\boldsymbol{x}, t)$ are the fluid (here air) velocity and pressure fields; ν, ρ and β are the (constant) kinematic viscosity, density and thermal expansion coefficient of the air; $\boldsymbol{g} = (0, 0, -g)$ is the gravitational acceleration, $T(\boldsymbol{x}, t)$ is the puff temperature field and T_a is the (constant) quiescent ambient temperature; finally, κ is the air thermal diffusion coefficient. Air exhaled by human expulsion is rich of water vapor, thus the specific humidity q is modeled by the advection-diffusion equation [149]

$$\partial_t q + \boldsymbol{u} \cdot \boldsymbol{\partial} q = D_v \partial^2 q, \tag{3.20}$$

where D_v is the water vapor diffusivity. In human exhalations $q \ll 1$, and we obtain $q \sim r \sim e\epsilon/p_a$ where r is the mixing ratio, e is the water vapor pressure, p_a is the ambient pressure and ϵ is the ratio between molar mass of water vapor and molar mass of dry air [149]. From the above relationships, it then follows that the supersaturation field is $s = e/e_{sat} - 1 \sim r/r_{sat} - 1$, where the subscript '$sat$' denotes the value at saturation. Exploiting the Magnus-Tetens relationship between e_{sat} and T (in which the temperature T is in degrees Celsius, see Ref. [128] and Sec.

3.2.1.) one immediately gets the supersaturation field s from the integration of the advection-diffusion equation, Eq. (3.20), for q.

The respiratory droplets are modeled using the same set of equations already described in Sec. 3.2.1.. The list of the relevant parameters used in these numerical experiments is reported in Table 3.4.

Table 3.4: List of physical and chemical parameters assumed in the present work.

Mean ambient temperature	T_a	$25\,°\mathrm{C}$
Crystallization (or efflorescence) RH	CRH	45%
Deliquescence RH	DRH	75%
Quiescent ambient RH ('Wet')	RH_a	60%
Quiescent ambient RH ('Dry')	RH_a	35%
Density of liquid water	ρ_w	$9.97 \times 10^2\,\mathrm{kg/m^3}$
Density of soluble aerosol part (NaCl)	ρ_s	$2.2 \times 10^3\,\mathrm{kg/m^3}$
Density of insoluble aerosol part (mucus)	ρ_u	$1.5 \times 10^3\,\mathrm{kg/m^3}$
Mass fraction of soluble material (NaCl) w.r.t. the total dry nucleus	ϵ_m	0.75
Mass fraction of dry nucleus w.r.t. the total droplet	$\mathcal{C}$	$1\,\%$
Specific gas constant of water vapor	R_v	$4.6 \times 10^2\,\mathrm{J/(kg\,K)}$
Diffusivity of water vapor	D_v	$2.5 \times 10^{-5}\,\mathrm{m^2/s}$
Density of air	ρ	$1.18\,\mathrm{kg/m^3}$
Kinematic viscosity of air	ν	$1.8 \times 10^{-5}\,\mathrm{m^2/s}$
Heat conductivity of dry air	k_a	$2.6 \times 10^{-2}\,\mathrm{W/K\,m}$
Latent heat for evaporation of liquid water	L_w	$2.3 \times 10^6\,\mathrm{J/kg}$
Saturation vapor pressure	e_{sat}	$0.616\,\mathrm{kPa}$
Droplet condensational growth rate	C_R	$1.5 \times 10^{-10}\,\mathrm{m^2/s}$
Surface tension between moist air and salty water	σ	$7.6 \times 10^{-2}\,\mathrm{J/m^2}$
Molar mass of NaCl	M_s	$5.9 \times 10^{-2}\,\mathrm{kg/mol}$
Molar mass of water	M_w	$1.8 \times 10^{-2}\,\mathrm{kg/mol}$
Molar mass of water vapor and molar mass of dry air ratio	ϵ	0.61

3.6.2. Numerical set-up

The initial droplet size distribution is the well known distribution from Ref. [115], with droplet radii approximately ranging from 1 to $1000\,\mu\mathrm{m}$ and the 95% falling between 1 and $50\,\mu\mathrm{m}$. Droplets are set initially at rest and randomly distributed within a sphere of radius $1\,\mathrm{cm}$ located inside the circular pipe from which the exhaled airflow is released; in our simulations, we assume the initial temperature of the exhaled air to be equal to $30\,^oC$, as in Ref. [113]. Finally, the exhaled droplets enter the ambient initially at rest with a relative humidity RH_a. Fig. 3.21 shows a sketch of the geometrical setup employed in our simulations. We consider a domain box of length $L_x = 3\,\mathrm{m}$, width $L_y = 2\,\mathrm{m}$ and height $L_z = 3\,\mathrm{m}$. The center of the barrier is placed at $1.6\,\mathrm{m}$ from the ground, having a height of $0.5\,\mathrm{m}$. The distance d of the barrier from the mouth is varied together with the ambient relative humidity. The fluid is initially at rest, i.e.

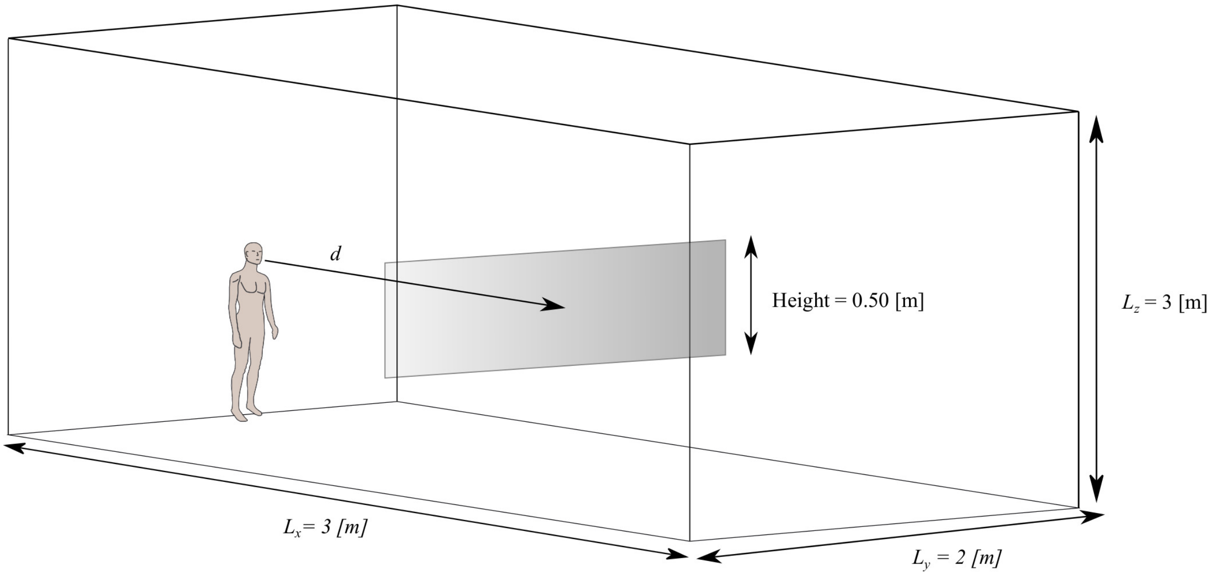

Figure 3.21: Sketch of the geometrical setup employed in our study.

$\boldsymbol{u}(\boldsymbol{x}, 0) = \mathbf{0}$, and at the ambient supersaturation $s(\boldsymbol{x}, 0) = s_a = \mathrm{RH}_a - 1$. The exhaled air is assumed to be fully saturated [113] (i.e. $s_{\mathrm{mouth}} = 0$) and is injected through a round opening of area $A_{\mathrm{mouth}} = 4.5\,\mathrm{cm}^2$ mimicking the mouth, at a distance from the ground of $z_{\mathrm{mouth}} = 1.6\,\mathrm{m}$. The injected airflow is prescribed according to the experimental measurements reported by Gupta et al. [109], already discussed in previous sections. Also in this case, the corresponding to a Reynolds numbers (based on the peak velocity and on the mouth average radius) of about 9×10^3. For the other domain boundaries, we prescribe the no-slip condition to simulate the presence of the body and the flow inside a room at the bottom ($z = 0$), top ($z = L_z$) and left ($x = 0$) boundaries. For both the velocity and supersaturation field, we impose a convective outlet boundary condition at the right boundary ($x = L_x$). Finally, periodic boundary conditions are enforced in the spanwise direction (i.e., $y = 0$ and $y = L_y$).

To model the presence of the barrier, here we use the immersed boundary method (IBM) originally proposed by Kajishima et. al. [150]. For the present simulations, the numerical domain is discretised with uniform grid spacing $\Delta x = 1.75\,\mathrm{mm}$ in all directions, resulting in a total number of approximately 1.2 billion grid points. The convergence of the results was verified by comparing the results with those obtained by doubling the grid resolution.

Exploiting such DNS approach, ten numerical experiments were performed for five possible barrier configurations at two different environmental conditions. Specifically, we consider a barrier with a height of 0.5 m which extends indefinitely along the spanwise direction, and vary the distance from the mouth at which the barrier is placed. Five geometrical configurations are considered: barrier placed at 0.25 m, 0.5 m, 0.75 m, 1 m from the mouth, and the configuration without any barrier for the sake of comparison. For each barrier, we consider two different values of ambient relative humidity, 'Dry' and 'Wet', corresponding to $RH_a = 30$ and $RH_a = 60$, respectively. In the 'Wet' condition, droplets do not evaporate completely but remain in equilibrium with the surrounding environment. In contrast, in the 'Dry' condition all droplets evaporate completely and shrink to their dry nuclei.

3.6.3. The role of barriers

To assess the associated risk of transmission, also in this case, the viral load VL, carried by the exhaled droplets has been quantified, by tracking the position of each droplet for a time of $15\mathrm{s}$. The focus is on the role of the barrier in removing the VL from air, and how the presence of the barrier can modify the sedimentation pattern of the VL to the ground. In Fig. 3.22 are shown three representative cases of the virus-containing droplets exhaled during a cough, with and without barrier in front of the mouth. The trajectories of the droplets are strongly modified by the presence of the barrier, as well as the amount of the viral load settling and remaining in the air.

In order to quantify the spread of the virus-containing droplets in indoor environments where a barrier is present (Fig. 3.21), we study the evolution of the viral load that settles to the ground, that deposits on the barrier and that remains airborne. Table 3.5 reports a summary of the cumulative VL after the overall simulation time ($15\mathrm{s}$), separating the contribution collected on the barrier, that settling to the ground and that remaining in the air, together with the corresponding number of droplets normalized to the total number of droplets (ND). Note however that the latter quantity can be misleading because of the presence of a few biggest droplets carrying the largest part of the viral load. For example, in the case of the barrier at a distance of $0.25\mathrm{m}$ from the mouth: in the 'Dry' condition, almost 47% of the droplets impact on the barrier carrying a VL of 98.9%; in the 'Wet' case instead, 67% of the droplets impact on the barrier, yet representing only 29% of the VL. From Table 3.5, it is possible to observe small differences between the 'Dry' and 'Wet' cases in terms of the number of droplets reaching the ground (1% and 1.57%, respectively), while large differences are evident for the carried viral load, 0.32% and 70%, respectively.

Table 3.5: Cumulative viral load (VL) and number of droplets (ND) on the barrier, to the ground and remaining in the air, for the two ambient humidities considered.

Barrier distance	VL on barrier (%)	VL to ground (%)	VL in air (%)	ND on barrier (%)	ND to ground (%)	ND in air (%)
'Dry' 0.25 m	98.91	0.32	0.77	47	1.57	51.43
'Dry' 0.5 m	95.15	3.24	1.61	32.38	0.66	66.96
'Dry' 0.75 m	19.22	78.15	2.63	17.81	0.97	81.22
'Dry' 1 m	3.78	92.54	3.68	5.35	1.13	93.52
'Dry' No barrier	0	95.81	4.19	0	1.11	98.89
'Wet' 0.25 m	29.3	70.64	0.06	67.3	1	31.7
'Wet' 0.5 m	14.46	85.26	0.27	45.13	1.42	53.45
'Wet' 0.75 m	6	93.57	0.43	22.6	3.08	74.32
'Wet' 1 m	1.38	98.1	0.52	8.39	4.64	86.97
'Wet' No barrier	0	99.43	0.57	0	5.05	94.95

Differences between the 'Dry' and 'Wet' conditions can be found when evaluating the distance from the mouth traveled by the droplets. Fig. 3.23 shows the probability density function (*pdf*) of the horizontal distance traveled by the droplets when they reach the ground. For the two ambient conditions, we count the number of the settled droplets at the time of $15\mathrm{s}$, comparing the results for different distances of the barrier from the mouth. The effect of the barrier is particularly evident in the cases where it is closer to the mouth, where the largest amount of droplets settles within $0.1\mathrm{m}$ and $0.5\mathrm{m}$, respectively, for both the 'Dry' and 'Wet' conditions. When the barrier is present, it is also possible to note the effect of the ambient humidity that

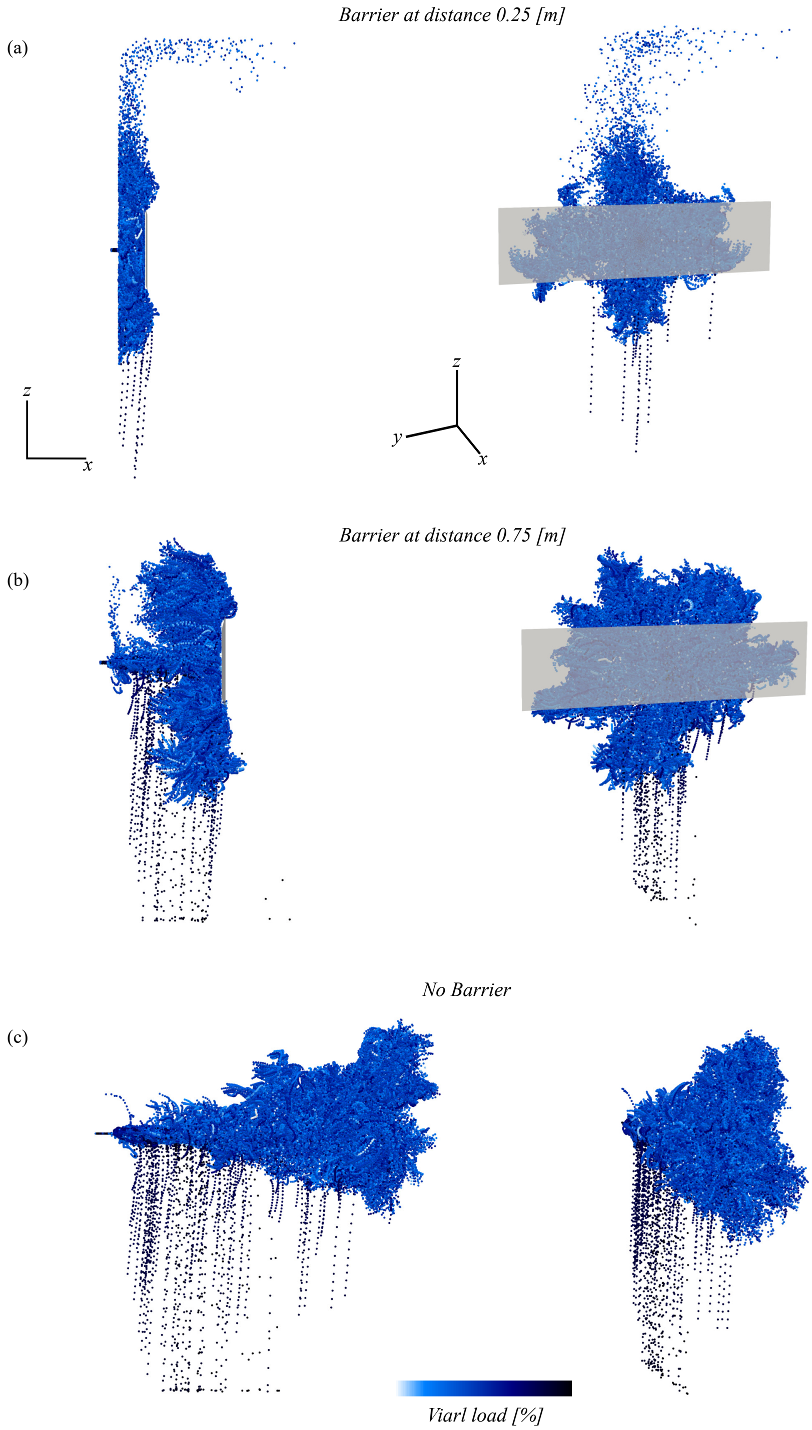

Figure 3.22: Side (left panels) and 3-D (right panels) views of virus-containing droplet trajectories computed by means of high-resolution DNS for three representative configurations, i.e., with barrier placed at a distance of (a) $0.25\mathrm{m}$ and (b) $0.75\mathrm{m}$ from the mouth and (c) without barrier. Results are shown for the 'Dry' condition. Droplets are colored by their Viral Load ($\%$, see its definition in the main text).

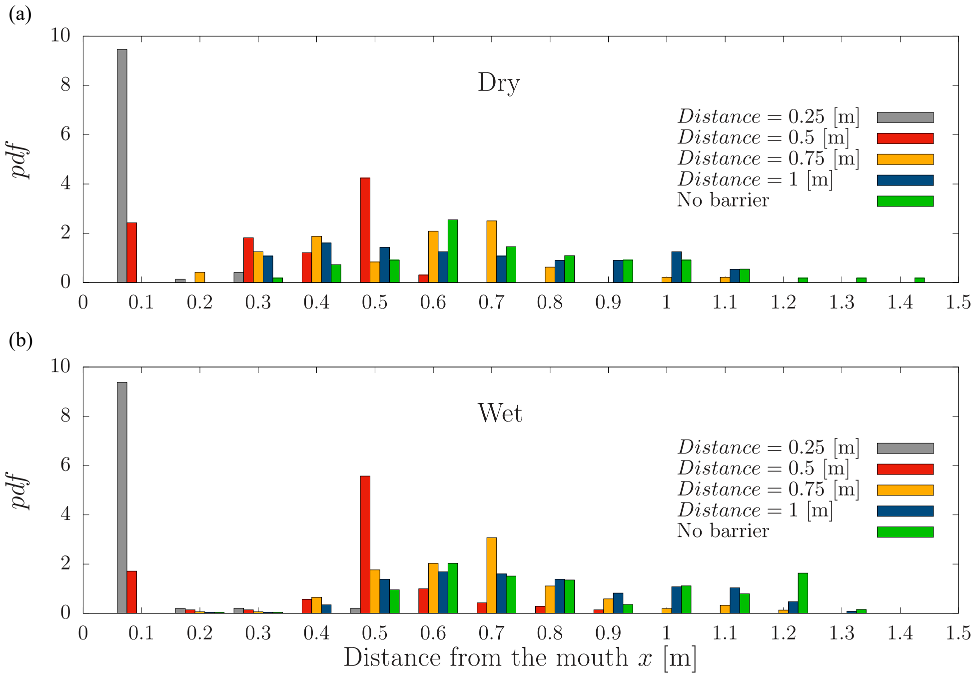

Figure 3.23: Probability density function of the distance from the mouth when droplets reach the ground. (a) 'Dry condition', (b) 'Wet' condition.

allows the droplets to travel for a larger distance in the 'Wet' condition with respect to the 'Dry' condition. This is in contrast with the cases without barrier, where the droplets are found to travel for larger distances in the 'Dry' condition. This is a clear inertial effect of the larger droplets: in the 'Wet' condition droplets are typically heavier than in the 'Dry' condition and follow ballistic trajectories, thus being able to overcome the barrier from below. On the other hand, the light droplets of the 'Dry' condition behave essentially as fluid tracers, thus remaining trapped in the vortical structures generated by the presence of the barrier (see Fig. 3.22).

To complement this analysis, in Fig. 3.24a and b we show the cumulative VL settling to the ground as a function of the distance from the mouth. We compare the settled VL with different distances of the barrier from the mouth, superimposing the case without barrier for the sake of comparison, for the 'Dry' and 'Wet' conditions. It is possible to notice the effect of the barrier in determining the amount of VL that reaches the ground: by increasing the distance of the barrier, the settling VL grows, for both the 'Dry' and 'Wet' ambient conditions. As expected, a higher amount of VL reaches the ground for the 'Wet' condition, especially when the barrier is close to the mouth (barrier distance of $0.25\mathrm{m}$ and $0.5\mathrm{m}$). By looking at the 'Wet' condition in Fig. 3.24b, we observe that the presence of the barrier has a negligible influence on the amount of settled VL when the barrier is far from the mouth, e.g. $0.75\mathrm{m}$ and $1\mathrm{m}$. Moreover, a greater distance is traveled by the VL in the 'Wet' condition with respect to the 'Dry' condition when the barrier is present. In Fig. 3.24c, we quantify the maximum distance reached by the VL settled to the ground; except for the case of the barrier at a distance of $0.75\mathrm{m}$, where the maximum distance is almost the same between the two ambient humidities, the 'Wet' condition shows always the higher maximum distance.

The study of the distance traveled by droplets and viral load is important to define protocols

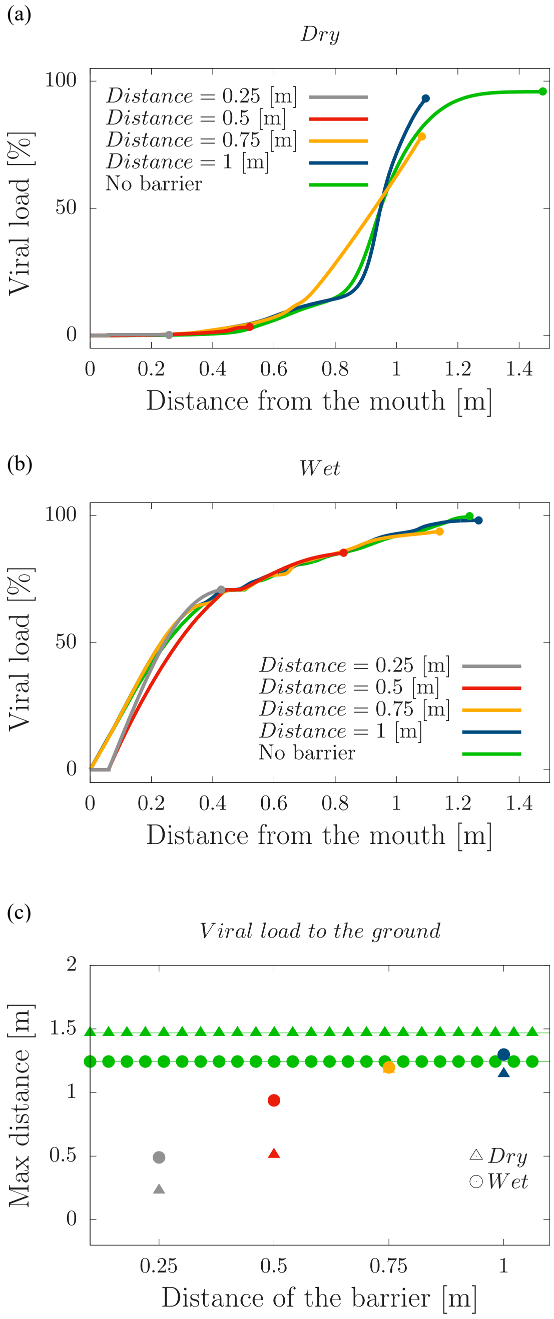

Figure 3.24: Cumulative Viral Load settling to the ground (%) as a function of the distance from the mouth: (a) ‘Dry’ and (b) ‘Wet’ conditions. The grey line represent the case with the barrier at 0.25 $[\mathrm{m}]$, the red line that at 0.5 $[\mathrm{m}]$, the yellow line at 0.75 $[\mathrm{m}]$, the blue line at 1 $[\mathrm{m}]$ and the green line the case without barrier. The dots at the end of the lines indicate the maximum distance reached by the cumulative viral load. (c) Maximum distance reached by the cumulative settling Viral Load in the (triangles) ‘Dry’ and (’circles’) ‘Wet’ conditions. The green point lines indicate the cases without barrier.

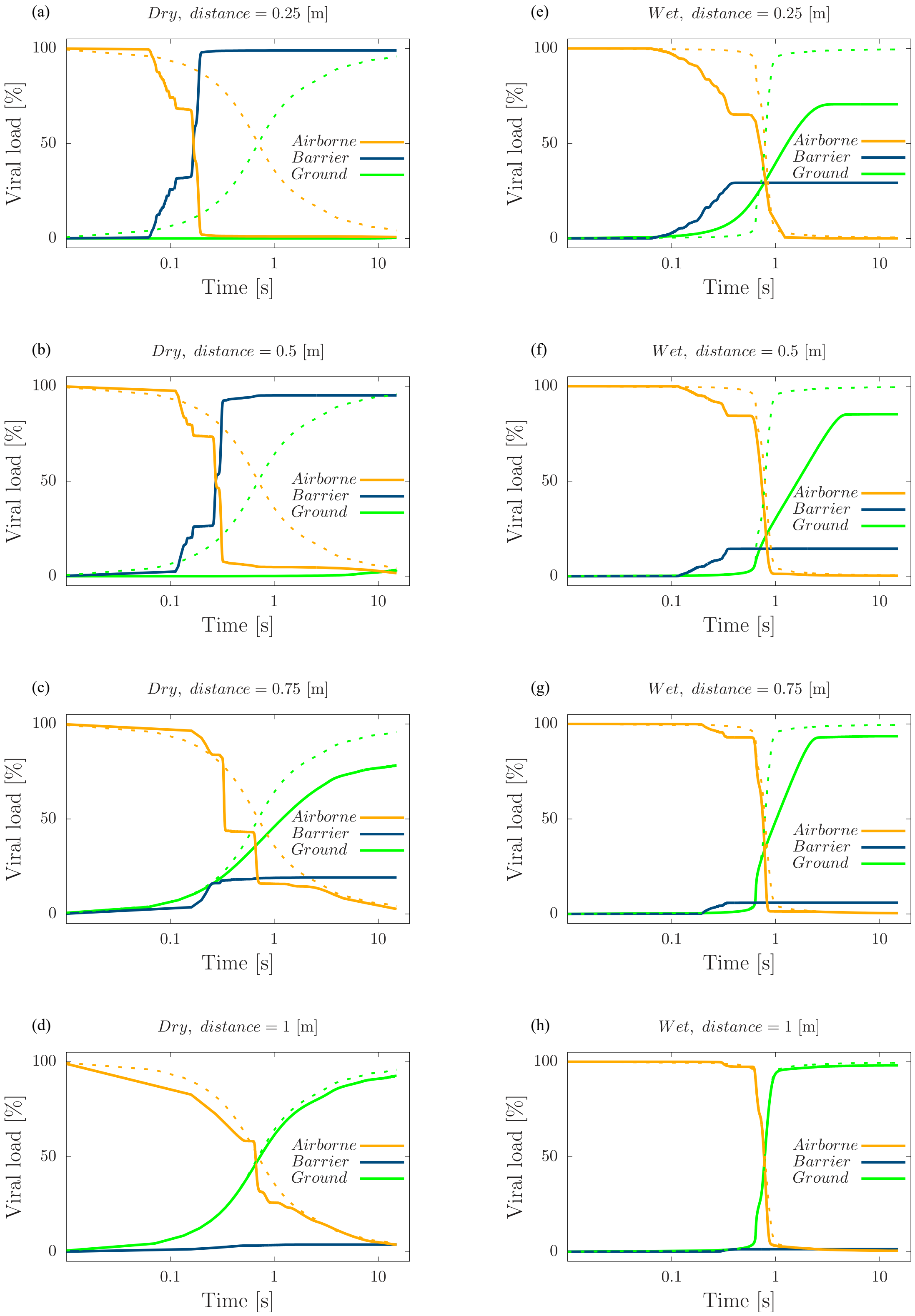

Figure 3.25: Time history of the cumulative Viral Load settling to the ground (green), captured by the barrier (blue) and remaining airborne (yellow). For the sake of comparison, we include the results for the case without barrier (dashed lines of the same colors).

and rules to protect people living in indoor environment. Studying the time history of the exhaled viral load during a cough is another important issue in order to quantify how long the viral load takes to settle and to impact on the barrier. In Fig. 3.25 it is shown the cumulative VL settling to the ground, that was captured by the barrier and that remaining airborne, in the observation time of $15\mathrm{s}$, for the 'Dry' and 'Wet' ambient conditions. Especially for the 'Dry' condition, the role of the barrier is crucial when it is close to the mouth, where almost 99% of the VL is captured in less than $1\mathrm{s}$ (Fig. 3.25a and Fig. 3.25b). This is not the case for the 'Wet' condition, where with a barrier at a distance of $0.25\mathrm{m}$ and $0.5\mathrm{m}$ from the mouth, only 29% and 15% of the VL is captured by the barrier, respectively, in less than $1\mathrm{s}$ (Fig. 3.25e and Fig. 3.25f). As far as the airborne viral load is concerned, we found a lower residence time in the air for the 'Dry' condition (less than $1\mathrm{s}$), in comparison with the 'Wet' condition where instead it is almost $1\mathrm{s}$ (Fig. 3.25a and Fig. 3.25e). By placing the barrier at increasing distances from the mouth, the captured VL reduces progressively. The amount of VL remaining in the air increases more for the 'Dry' cases, with longer residence time with respect to the 'Wet' ones, where the majority of VL is loss by sedimentation (Fig. 3.25b, Fig. 3.25c, Fig. 3.25d, Fig. 3.25f, Fig. 3.25g and Fig. 3.25h). Considering a barrier at a distance of $0.75\mathrm{m}$ from the mouth, we find 6% of the airborne VL after $6\mathrm{s}$ for the 'Dry' condition, while it is 0.57% for the 'Wet' one. Also, it can be observed the negligible effect of the barrier when it is at $1\mathrm{m}$ from the mouth (Fig. 3.25d and Fig. 3.25h). This is more evident for the 'Wet' condition, where the curves are substantially superimposed to those for the cases without barrier (Fig. 3.25h).

Once the viral load is removed from the air by sedimentation or by impacting on the barrier, the remaining viral load is still airborne and can have a crucial role in disease transmission, such as COVID-19 infection [151]. Thus, in the last step of our analysis we focus on the distance traveled by the airborne viral load. In Fig. 3.26a and b we report the cumulative airborne VL as a function of the distance from the mouth, for the two ambient conditions considered. Note that here 100% of the VL represents the total amount of the airborne viral load only. For both the 'Dry' and 'Wet' conditions, the barrier has an important role in determining the distance traveled by the airborne VL, also when the barrier is far form the mouth; this distance is always lower with respect to the case when the barrier is not present, where the VL can travel more than $2\mathrm{m}$ from the mouth. Indeed, the traveled distance is approximately $1.3\mathrm{m}$ and $1\mathrm{m}$ for the 'Dry' and 'Wet' conditions with the barrier at $1\mathrm{m}$ from the mouth. Of particular interest is the role of the distance of the barrier in determining the distance traveled by the airborne viral load: By displacing the barrier away from the mouth, the traveled distance increases; however, when the barrier is very close to the mouth ($0.25\mathrm{m}$), the distance traveled is higher than in the other cases ($0.5\mathrm{m}$, $0.75\mathrm{m}$ and $1\mathrm{m}$) for both the 'Dry' and 'Wet' conditions. This can be appreciated from Fig. 3.22a, where the presence of the barrier determines an upward flow velocity, which carries the lightest droplets above the barrier and then let them travel beyond for larger distances. We quantify the maximum distance reached by the airborne viral load in the observation time in Fig. 3.26c. Also here, we can note the nontrivial effect of the barrier when it is at a distance of $0.25\mathrm{m}$, where the airborne viral load travels for large distance beyond the barrier, more than in the other cases. Finally, due to the lighter weight of the droplets in the 'Dry' conditions, the maximum distance is always greater than what we observe in the 'Wet' conditions, except for the case with a barrier at $0.75\mathrm{m}$ where the maximum distance is approximately the same for the two conditions considered.

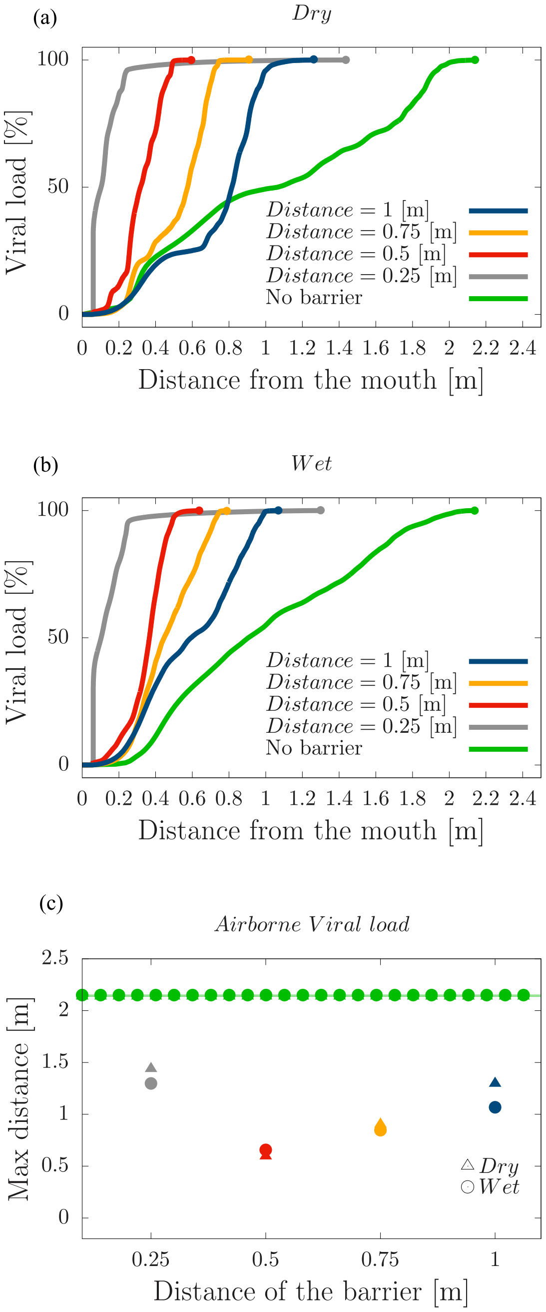

Figure 3.26: Cumulative airborne Viral Load (%) in function of the distance from the mouth (a) for the 'Dry' and (b) 'Wet' conditions. The grey line represent the case with the barrier at a distance from the mouth of 0.25 [m], the red line that at 0.5 [m], the yellow line at 0.75 [m], the blue line at 1 [m] and the green line for the case without barrier. The dots at the end of the lines indicate the maximum distance reached by the cumulative viral load. Note that here the 100% of the Viral load represent the total amount of the airborne Viral Load. (c) Maximum distance reached by the cumulative airborne Viral Load in the (triangles) 'Dry' and ('circles') 'Wet' conditions. The green point lines indicate the cases without barrier.

3.7. Summary and conclusions

By means of high-resolutions DNS experiments, this chapter investigated the physical mechanisms involved in violent expiratory events such as coughing or sneezing, focusing on different aspects related to the spread of virus-containing droplets. The droplet dynamics are evolved by means of a Lagrangian model including the evolution of droplet radius to properly describe the droplet evaporation process.

In particular the role of turbulence has been investigated, with a focus on the evaporation and consequent airborne spread of small exhaled droplets. By assuming an initial size distribution of the droplet [115], each single droplet has been tracked in time, by distinguishing between larger droplets which settle on the ground ballistically and the smaller droplets which remain trapped in the turbulent puff. For such airborne droplets, we found that turbulence plays a crucial role in determining their evaporation time. The comparison with two different coarse-graining techniques, i.e., filtered DNS and mean-field simulation, demonstrate this result. Compared to the DNS results, we find that coarse graining leads to underestimating droplet evaporation time up to 100%. Correspondingly, we find that DNSs are crucial to accurately describe the inertial effects in droplet trajectory and ultimately predict their flight time and final reach. Importantly, the heated debate on social distancing rules depends crucially on these observables.

As a second stage, the influence of different ambient humidity conditions and different initial size distributions of the droplet, taken from literature, have been considered. Here, the central observable is the relative viral load, i.e. the amount of virus carried by an individual droplet normalized to the total amount of virus in the ensemble of droplets. Note that to connect the relative viral load to the probability of infection, further information is needed. With these simulations we demonstrate that currently available information is inadequate to design social distancing recommendations on a solid scientific basis. Indeed, diametrically opposed predictions are drawn depending on the size distribution of the respiratory droplets and ambient humidity: (i) most versus none of the viral load settles in the first $1-2\mathrm{m}$ in few seconds; (ii) all viral load is carried on dry nuclei versus liquid droplets and (iii) small airborne particles travel less than $2.5\mathrm{m}$ versus more than $7.5\mathrm{m}$. Those results show that a single rule for social distancing may not be adequate to protect individuals in different environments. Te relative humidity of the environment has a particularly dramatic effect, with all droplets evaporating to their dry nuclei under sufficiently dry conditions, and all droplets remaining liquid under sufficiently wet environmental conditions.

The third step investigates the influence of the gender of the emitting subject in the dynamics of violent expiratory events in order to better characterize the transport and evaporation process undergone by the exhaled saliva droplets. Although the physical process is found to be essentially the same from a qualitative viewpoint, substantial quantitative differences occur between men and women in terms of the droplet final reach and evaporation time. The horizontal distance traveled by droplets is found to be generally larger for men, and so is for the cumulative viral load reaching a 2-meter distance. For women the droplet evaporation time is larger due to a slower dynamics while residing within the turbulent puff. Overall, the results can be associated to the different characteristic airflow, with a typically stronger expulsion for men. It should be pointed out that the influence of gender is typically correlated with other physical parameters, such as the weight of the subject. It cannot therefore be excluded the latter to have a dominant role in the dynamics of expiratory events.

Finally, it has been studied the spread of the virus-containing droplets in indoor environments where a barrier is present. To investigate the role of barriers as protection devices from the viral load exhaled during a cough, we considered two ambient relative humidity (”Dry” and ”Wet” condition) and four distances of the barrier from the mouth comparing the obtained results with the case without barrier. Because of the larger inertia of droplets in the ’Wet’ case, which determine ballistic events during the transport process, we find that in the ”Wet” condition, the settling viral load travels for larger distances with respect to the ”Dry” condition, for all the barrier distances investigated. This fact is in contrast with the observation in the case without barrier, where, as expected and in agreement on what shown in Sec. 3.4., it is the ”Dry” case that allows the VL to settle further away from the mouth. Since the lightest droplets behave as fluid tracers, they remain trapped in the vortices created by the exhaled flow impacting on the barrier, thus making it difficult to travel for larger distances. This is the main mechanism caused by the barrier as a protection device. Indeed, it has been observed a greater amount of viral load captured by the barrier in the ”Dry” case, especially when it is close to the mouth. As for the airborne viral load, results show a larger amount of airborne viral load for cases in the ”Dry” condition, which increases with the distance of the barrier from the mouth. The barrier has therefore an important role to limit the distance traveled by the airborne VL, since it is always smaller than that in the case without barrier. Furthermore, the ”Dry” cases show a greater distance traveled from the mouth with respect to the ”Wet” cases.

The quantitative and qualitative results obtained in this study, can actively contribute to select optimal strategies of protection and mitigation of the airborne infection transmission, within indoor and outdoor environments. The results are not restricted to COVID-19, being valid for all the infections where the main route of transmission is via airborne virus-containing droplets.

Chapter 4
Conclusions

The thesis is divided in two parts. The first part is focused on the measure of flow properties by means of slender objects, i.e. rigid fibers and slender swimmers. Two different strategies have been employed to model the fiber: first an active model, a fully-coupled fiber described in terms of an immersed-boundary method, and, second, a passive model, a one-way coupling where the fiber is described by the slender body theory. The motion of the fiber is investigated for different classes of closed streamline flows, steady or time dependent, two-dimensional or three dimensional. The preliminary stage is the characterization of the fiber inertia. This has been done in terms of rotational Stokes number, which is evaluated as a function of the fiber linear density. The rotational Stokes number has been evaluated only for the fiber fully coupled to the fluid flow, since for the fiber modeled with the passive model it is an assigned parameter. The main result is that the fiber turns out to be a proxy of the underlying flow by considering the velocity difference between the fiber end points and the same difference relative to the underlying fluid velocity, both projected along the direction normal to the fiber. If the fiber length is sufficiently small, compared to the characteristic length-scale of the flow, the two-point velocity difference reduces to the transverse component of the flow velocity derivative along the fiber direction. Then, by composing an assembly of rigid fibers, three for a two dimensional flow and eight for a three dimensional flow, it is possible to reconstruct the whole gradient tensor of the flow, by simply solving a liner system of equations during the Lagrangian tracking of the assembly. Moreover, results suggest that the coupling between the flow and the fiber could be neglected, for sufficiently small Stokes number.

As a step forward, it has been investigated the perception of hydrodynamics signal by slender swimmers, which from a fluid dynamics point of view can be classified as pusher or puller swimmers. A model for a slender swimmer has been proposed by imposing the no-slip condition and the propulsion force on the same half length of the slender motile object, the spreading of the pushing/pulling forcing acting on the fluid being imposed on the other half (the so-slip condition was not applied in that portion of the Lagrangian grid). In the limit of Stokes flow and in a fluid initially at rest, the flow motion determined by the swimmer model has been validated with the di-Stokeslet solution with excellent agreement. Once the swimmer model has been validated, the reached swimming velocity given a propulsion force has been assessed. The results show that pusher and puller swimmers reach different swimming velocity given the same propulsion force. An interesting result is that the slender-body theory can be related to the resulting swimming velocity for pushers but not for pullers. The reason to understand this finding is the different vorticity generated by the motion of the two swimmer type. By exploiting a chaotic flow field with flow Reynolds number up to 10, a swimming number ranging between zero and one, and different swimmer inertia, the capability of slender swimmers to sense hydrodynamics signals has been tested. Results show that despite the perturbation caused by the swimmer motion, there exist hydrodynamics observables practically unaffected by the swimmer motion, i.e. the swimmer velocity differences evaluated at the swimmer ends, projected along a direction on a plane normal to the swimmer orientation. This capability has been tested for a wide range of flow/swimmer Reynolds number, both pusher and puller, thus suggesting the robustness of our findings, at least in the range of Reynolds number investigated.

The capability of rigid fibers and slender swimmer to measure two-point flow observables has potential application in non-intrusive experimental measurement techniques allowing to access small-scale, multi-point properties of fluid flows, offering an alternative to other methods (i.e. PIV and PTV), by following artificial self-propelled slender objects or by Lagrangian tracking of rigid fibers or assembly of them.

The second part of this thesis investigates the spreading of virus-containing droplets during a human cough under realistic conditions. More specifically, a turbulent puff, used to model a human cough, has been studied in order to track the spreading of the exhaled droplets. To this aim, high resolutions DNS have been performed for the fluid flow and humidity field, complemented by a passive Lagrangian solver for the droplet dynamics including a dynamical equation for the evolution of the droplet radii modeling the evaporation-condensation process. After the phenomenological validation of the turbulent puff, the role of turbulence has been investigated, by focusing on the evaporation and consequent airborne spread of small exhaled droplets. Each single droplet has been tracked in time, by distinguishing between larger droplets which settle on the ground ballistically and the smaller droplets which remain trapped in the turbulent puff. The comparison of results obtained with fully resolved DNS and two different coarse-graining techniques, i.e., filtered DNS and mean-field simulation, demonstrate that turbulence plays a crucial role in determining their evaporation time, since coarse graining techniques leads to underestimating droplet evaporation time up to 100%, compared with DNS results.

Once the main physical mechanisms ruling the the fate of virus-containing droplets has been understood, the impact of virus spreading on the society has been discussed. The main observable is the relative viral load, i.e. the amount of virus carried by an individual droplet normalized to the total amount of virus in the ensemble of droplets. By considering the influence of different ambient humidity conditions and different initial size distributions of the droplet, taken from literature, it has been demonstrated that currently available information is inadequate to design social distancing recommendations on a solid scientific basis. In fact, opposed predictions can be drawn depending on the size distribution of the respiratory droplets and ambient humidity, showing that a single rule for social distancing may not be adequate to protect individuals in different environments. The results can be summarized as follow: (i) most versus none of the viral load settles in the first $1 - 2\mathrm{m}$ in few seconds; (ii) all viral load is carried on dry nuclei versus liquid droplets and (iii) small airborne particles travel less than $2.5\mathrm{m}$ versus more than $7.5\mathrm{m}$.

As an additional step, the influence of the gender of the emitting subject in the dynamics of violent expiratory events has been investigated, in order to better characterize the transport and evaporation process undergone by the exhaled saliva droplets. The physical process is found to be essentially the same from a qualitative viewpoint, but substantial quantitative differences occur between men and women in terms of the droplet final reach and evaporation time. Due to the different characteristic airflow, with a typically stronger expulsion for men, the horizontal distance traveled by droplets is found to be larger for men, and so it is for the cumulative viral load reaching a 2-meter distance. Moreover, for women the droplet evaporation time is larger due to a slower dynamics while residing within the turbulent puff.

As last step, the role of barriers, as protection device from disease infection, within indoor environment has been investigated. Two relative ambient humidities has been considered, denoted by 'Dry' and 'Wet' condition, and four distances of the barrier from the mouth has been taken into account. The obtained results has been compared with the 'Dry' and 'Wet' condition without barrier. The results show that in 'Wet' condition the settling viral load travels for larger distances with respect to the 'Dry' condition, for all the barrier distances investigated, because of the larger inertia which determine ballistic events during the transport process. The lightest droplets behave as fluid tracers, and then, they remain trapped in the vortices created by the exhaled flow impacting on the barrier, thus making it difficult to travel for larger distances. Indeed, the 'Dry' case shows a greater amount of viral load captured by the barrier, especially when it is close to the mouth. As concern the airborne viral load, it results to be larger in 'Dry' conditions, and it increases with the distance of the barrier from the mouth, although it is always smaller than that in the case without barrier.

The study described above is clearly motivated by the recent pandemic situation due to COVID-19 infection, although it is valid for all the infections where the main route of transmission is via airborne virus-containing droplets, by contributing to select optimal strategies of protection and mitigation of the airborne infection transmission, within indoor and outdoor environments.

In conclusion, this thesis reports results of numerical experiments exploiting active and passive models for fibers and particles modeling in different environmental flow applications, showing how rigid fibers and slender swimmers can be used to access to flow properties, and how the study of the flow can be used to access information on spreading of droplets.

Further research interests

The research interests born during the PhD period went beyond what is reported in the main structure of this thesis. In particular, the focus shifted to the study of suspensions of slender swimmers in the regime of finite Reynolds number.

The motion of swimming organisms in the Stokes regime has been widely explored, both theoretically and numerically, as reported in the review paper by Pak and Lauga [152]. In contrast, swimming at moderate Reynolds numbers, where inertia plays a significant role, has received far less attention to date. The hydrodynamic interactions of swimming organisms in this regime are significantly different from the Stokes regime for microorganisms, as well as for fish and birds, which involve flow separation and detached vortex structures [153].

Since the collective behavior of swimmer suspensions in inertial regimes has been poorly studied and little is known on the generated flow field, the focus has been to investigate the resulting flow motions due to a swarm of slender swimmers, in the regime of finite Reynolds number, based on the swimmer length scale and swimming velocity. To this aim, by using an inertial slender swimmer model, which is able to behave as pusher or puller, and validated in the Stokes regime, as shown in Sec. 2.2.4., the suspensions of pushers and pullers have been investigated in dilute volume fractions, and swimming Reynolds numbers, Re_s, ranging from 1 to 50. By using direct numerical simulations, the objective has been to identify the existence of correlated flow motions and to investigate hydrodynamic interactions in the regime of finite Reynolds number, by exploiting a state-of-the-art fully resolved immersed boundary method.

In order to characterize the emergence of flow patterns due to the swarm of slender swimmers, simulations have been performed with the swimmers starting from an isotropic orientation, in a tri-periodic domain. The fluid, initially at rest, has been left to evolve under the disturbance generated by the collective swimming of mono-disperse suspensions of pushers and pullers.

Results reveal a flow field characterized by velocity fluctuations significantly larger than the isolated swimming speed. These velocities decrease as the Re_s increases, leading to complex flow motions which are correlated on length scales smaller and smaller as the swimming Reynolds number increases. While pullers generate higher velocity fluctuations, the correlation lengths are always larger for pushers, for all investigated Re_s and volume fraction. The correlation lengths range from sizes comparable to the swimmer length, for low Re_s, to less than the half swimmer length, for high Re_s. The spectral analysis of the flow field, resulting by the swimmers motion, reveals that the kinetic energy of the velocity field is picked at smaller and smaller scales by increasing Re_s. Moreover, the pullers energy peak is found at smaller scales with respect to pushers. These results confirm the observation of decreasing correlated motion as Re_s grows, which are always smaller for suspensions of pullers. Finally, the analysis on hydrodynamic interactions between swimmers shows that pullers are locally more disordered with respect to pushers, although pullers result to be more hydrodynamically linked. For low Re_s, pushers present a tendency to parallel swimming, which decreases as Re_s increases, while pullers at low Re_s show a slight departure from the initial isotropic state. For high Re_s, pullers show the tendency to anti-parallel swimming. As Re_s increases, the anti-parallel swimming is progressively reduced, while the tendency to parallel swimming increases.

In the same framework as the one considered here, it will be also interesting to investigate the late-time evolution of swimmer dynamics, a regime that may be described in terms of eddy diffusivities. Are the resulting eddy diffusivities, provided that a diffusive motion sets in, the same for pusher and puller swimmers? Are there regimes of anomalous diffusion and are these regimes different for pullers and pushers? Answering all these questions will shed further light on how finite Reynolds number swimmers interact each other and with the surrounding fluid.

BIBLIOGRAPHY

[1] G. A. Voth and A. Soldati. Anisotropic particles in turbulence. *Annu. Rev. Fluid Mech.*, 49(1):249–276, 2017.

[2] Vishal A Patil and James A Liburdy. Scale estimation for turbulent flows in porous media. *Chemical Engineering Science*, 123:231–235, 2015.

[3] Annick Pouquet and Raffaele Marino. Geophysical turbulence and the duality of the energy flow across scales. *Physical review letters*, 111(23):234501, 2013.

[4] Stefano Brizzolara, Marco Edoardo Rosti, Stefano Olivieri, Luca Brandt, Markus Holzner, and Andrea Mazzino. Fiber tracking velocimetry for two-point statistics of turbulence. *arXiv preprint arXiv:2010.15912*, 2020.

[5] Marco Edoardo Rosti, Arash Alizad Banaei, Luca Brandt, and Andrea Mazzino. Flexible fiber reveals the two-point statistical properties of turbulence. *Physical review letters*, 121(4):044501, 2018.

[6] Marco E Rosti, Stefano Olivieri, Arash A Banaei, Luca Brandt, and Andrea Mazzino. Flowing fibers as a proxy of turbulence statistics. *Meccanica*, 55(2):357–370, 2020.

[7] Shima Parsa and Greg A Voth. Inertial range scaling in rotations of long rods in turbulence. *Physical review letters*, 112(2):024501, 2014.

[8] Ankur D Bordoloi and Evan Variano. Rotational kinematics of large cylindrical particles in turbulence. *Journal of Fluid Mechanics*, 815:199–222, 2017.

[9] S Bounoua, G Bouchet, and Gautier Verhille. Tumbling of inertial fibers in turbulence. *Physical review letters*, 121(12):124502, 2018.

[10] Christophe Brouzet, Gautier Verhille, and Patrice Le Gal. Flexible fiber in a turbulent flow: A macroscopic polymer. *Physical review letters*, 112(7):074501, 2014.

[11] B. Hejazi, M. Krellenstein, and G. A. Voth. Using deformable particles for single-particle measurements of velocity gradient tensors. *Exp. Fluids*, 60(10):153, Sep 2019.

[12] Stefan Kramel, Greg A Voth, Saskia Tympel, and Federico Toschi. Preferential rotation of chiral dipoles in isotropic turbulence. *Physical review letters*, 117(15):154501, 2016.

[13] JLG Oliveira, CWM Van der Geld, and Johannes GM Kuerten. Lagrangian velocity and acceleration statistics of fluid and inertial particles measured in pipe flow with 3d particle tracking velocimetry. *International journal of multiphase flow*, 73:97–107, 2015.

[14] Stephen B Pope. Lagrangian pdf methods for turbulent flows. *Annual review of fluid mechanics*, 26(1):23–63, 1994.

[15] PK Yeung. Lagrangian investigations of turbulence. *Annual review of fluid mechanics*, 34(1):115–142, 2002.

[16] WH Gauvin, S Katta, and FH Knelman. Drop trajectory predictions and their importance in the design of spray dryers. *International Journal of Multiphase Flow*, 1(6):793–816, 1975.

[17] George Barker Jeffery. The motion of ellipsoidal particles immersed in a viscous fluid. *Proceedings of the Royal Society of London. Series A, Containing papers of a mathematical and physical character*, 102(715):161–179, 1922.

[18] Jason E Butler and Braden Snook. Microstructural dynamics and rheology of suspensions of rigid fibers. *Annual Review of Fluid Mechanics*, 50:299–318, 2018.

[19] K Gustavsson, J Einarsson, and B Mehlig. Tumbling of small axisymmetric particles in random and turbulent flows. *Physical review letters*, 112(1):014501, 2014.

[20] S. Parsa, E. Calzavarini, F. Toschi, and G. A. Voth. Rotation rate of rods in turbulent fluid flow. *Phys. Rev. Lett.*, 109:134501, Sep 2012.

[21] M Byron, J Einarsson, K Gustavsson, G Voth, B Mehlig, and E Variano. Shape-dependence of particle rotation in isotropic turbulence. *Physics of Fluids*, 27(3):035101, 2015.

[22] Sergio Chibbaro, Cristian Marchioli, Maria Vittoria Salvetti, and Alfredo Soldati. Particle tracking in les flow fields: conditional lagrangian statistics of filtering error. *Journal of Turbulence*, 15(1):22–33, 2014.

[23] DO Njobuenwu and M Fairweather. Dynamics of single, non-spherical ellipsoidal particles in a turbulent channel flow. *Chemical Engineering Science*, 123:265–282, 2015.

[24] Gregory Lecrivain, Rohan Rayan, Antonio Hurtado, and Uwe Hampel. Using quasi-dns to investigate the deposition of elongated aerosol particles in a wavy channel flow. *Computers & Fluids*, 124:78–85, 2016.

[25] F Bianco, Sergio Chibbaro, Cristian Marchioli, Maria Vittoria Salvetti, and Alfredo Soldati. Intrinsic filtering errors of lagrangian particle tracking in les flow fields. *Physics of Fluids*, 24(4):045103, 2012.

[26] Antonio Celani, Gregory Falkovich, Andrea Mazzino, and Agnese Seminara. Droplet condensation in turbulent flows. *EPL (Europhysics Letters)*, 70(6):775, 2005.

[27] Paolo Gualtieri, F Picano, Gaetano Sardina, and Carlo Massimo Casciola. Exact regularized point particle method for multiphase flows in the two-way coupling regime. *Journal of Fluid Mechanics*, 773:520–561, 2015.

[28] F Zhao and BGM Van Wachem. Direct numerical simulation of ellipsoidal particles in turbulent channel flow. *Acta Mechanica*, 224(10):2331–2358, 2013.

[29] F Zhao, WK George, and BGM Van Wachem. Four-way coupled simulations of small particles in turbulent channel flow: The effects of particle shape and stokes number. *Physics of Fluids*, 27(8):083301, 2015.

[30] Wei-Xi Huang, Soo Jai Shin, and Hyung Jin Sung. Simulation of flexible filaments in a uniform flow by the immersed boundary method. *Journal of computational physics*, 226(2):2206–2228, 2007.

[31] Charles S Peskin. Flow patterns around heart valves: a numerical method. *Journal of computational physics*, 10(2):252–271, 1972.

[32] Stefano Olivieri, Francesco Viola, Andrea Mazzino, and Marco E. Rosti. Direct numerical simulation of flapping flags in grid-induced turbulence. *Physics of Fluids*, 33(8):085116, 2021.

[33] Rajat Mittal, Haibo Dong, Meliha Bozkurttas, Alfred Loebbecke, and Faddy Najjar. Analysis of flying and swimming in nature using an immersed boundary method. In *36th AIAA Fluid Dynamics Conference and Exhibit*, page 2867, 2006.

[34] Seyedsaeed Mirazimi. *Meso-swimmer suspensions: immersed boundary simulations of hydrodynamic interactions between worm-like swimmers*. PhD thesis, Science: Department of Mathematics, 2018.

[35] Robert Dillon, Lisa Fauci, Aaron Fogelson, and Donald Gaver III. Modeling biofilm processes using the immersed boundary method. *Journal of Computational Physics*, 129(1):57–73, 1996.

[36] O. du Roure, A. Lindner, E. N. Nazockdast, and M. J. Shelley. Dynamics of flexible fibers in viscous flows and fluids. *Annu. Rev. Fluid Mech.*, 51(1):539–572, 2019.

[37] M. J. Shelley and J. Zhang. Flapping and bending bodies interacting with fluid flows. *Annu. Rev. Fluid Mech.*, 43:449–465, 2011.

[38] S. Bagheri, A. Mazzino, and A. Bottaro. Spontaneous symmetry breaking of a hinged flapping filament generates lift. *Phys. Rev. Lett.*, 109:154502, Oct 2012.

[39] U. Lācis, N. Brosse, F. Ingremeau, A. Mazzino, F. Lundell, H. Kellay, and S. Bagheri. Passive appendages generate drift through symmetry breaking. *Nat. Commun.*, 5:5310, 2014.

[40] U. Lācis, S. Olivieri, A. Mazzino, and S. Bagheri. Passive control of a falling sphere by elliptic-shaped appendages. *Phys. Rev. Fluids*, 2:033901, Mar 2017.

[41] C. Marchioli, M. Fantoni, and A. Soldati. Orientation, distribution, and deposition of elongated, inertial fibers in turbulent channel flow. *Phys. Fluids*, 22(3):033301, 2010.

[42] M. Do-Quang, G. Amberg, G. Brethouwer, and A. V. Johansson. Simulation of finite-size fibers in turbulent channel flows. *Phys. Rev. E*, 89:013006, Jan 2014.

[43] C. Marchioli, L. Zhao, and H. I. Andersson. On the relative rotational motion between rigid fibers and fluid in turbulent channel flow. *Phys. Fluids*, 28(1):013301, 2016.

[44] R. Ni, S. Kramel, N. T. Ouellette, and G. A. Voth. Measurements of the coupling between the tumbling of rods and the velocity gradient tensor in turbulence. *J. Fluid Mech.*, 766:202–225, 2015.

[45] L. Sabban, A. Cohen, and R. van Hout. Temporally resolved measurements of heavy, rigid fibre translation and rotation in nearly homogeneous isotropic turbulence. *J. Fluid Mech.*, 814:42–68, 2017.

[46] S. Kuperman, L. Sabban, and . van Hout. Inertial effects on the dynamics of rigid heavy fibers in isotropic turbulence. *Phys. Rev. Fluids*, 4:064301, Jun 2019.

[47] N. Pujara, G. A. Voth, and E. A. Variano. Scale-dependent alignment, tumbling and stretching of slender rods in isotropic turbulence. *J. Fluid Mech.*, 860:465–486, 2019.

[48] R. J. Adrian. Particle-imaging techniques for experimental fluid mechanics. *Annu. Rev. Fluid Mech.*, 23(1):261–304, 1991.

[49] K. Hoyer, M. Holzner, B. Lüthi, M. Guala, A. Liberzon, and W. Kinzelbach. 3D scanning particle tracking velocimetry. *Exp. Fluids*, 39(5):923, Aug 2005.

[50] D. Schanz, S. Gesemann, and A. Schröder. Shake-the-box: Lagrangian particle tracking at high particle image densities. *Exp. Fluids*, 57(5):70, Apr 2016.

[51] S. Bounoua, G. Bouchet, and G. Verhille. Tumbling of inertial fibers in turbulence. *Phys. Rev. Lett.*, 121:124502, Sep 2018.

[52] Thierry Dombre, Uriel Frisch, John M Greene, Michel Hénon, A Mehr, and Andrew M Soward. Chaotic streamlines in the abc flows. *Journal of Fluid Mechanics*, 167:353–391, 1986.

[53] L Biferale, A Crisanti, M Vergassola, and A Vulpiani. Eddy diffusivities in scalar transport. *Physics of Fluids*, 7(11):2725–2734, 1995.

[54] Hamidreza Ardeshiri, Ibtissem Benkeddad, François G Schmitt, Sami Souissi, Federico Toschi, and Enrico Calzavarini. Lagrangian model of copepod dynamics: Clustering by escape jumps in turbulence. *Physical Review E*, 93(4):043117, 2016.

[55] Bernard Bonnard, Monique Chyba, Jéremy Rouot, and Daisuke Takagi. Sub-riemannian geometry, hamiltonian dynamics, micro-swimmers, copepod nauplii and copepod robot. *Pacific Journal of Mathematics for Industry*, 10(1):1–27, 2018.

[56] David H Gire, Vikrant Kapoor, Annie Arrighi-Allisan, Agnese Seminara, and Venkatesh N Murthy. Mice develop efficient strategies for foraging and navigation using complex natural stimuli. *Current Biology*, 26(10):1261–1273, 2016.

[57] Simona Colabrese, Kristian Gustavsson, Antonio Celani, and Luca Biferale. Flow navigation by smart microswimmers via reinforcement learning. *Physical review letters*, 118(15):158004, 2017.

[58] Knut Drescher, Raymond E. Goldstein, Nicolas Michel, Marco Polin, and Idan Tuval. Direct measurement of the flow field around swimming microorganisms. *Phys. Rev. Lett.*, 105:168101, Oct 2010.

[59] Knut Drescher, Jörn Dunkel, Luis H. Cisneros, Sujoy Ganguly, and Raymond E. Goldstein. Fluid dynamics and noise in bacterial cell–cell and cell–surface scattering. *Proceedings of the National Academy of Sciences*, 108(27):10940–10945, 2011.

[60] Eric Lauga and Thomas R Powers. The hydrodynamics of swimming microorganisms. *Reports on Progress in Physics*, 72(9):096601, aug 2009.

[61] R. Di Leonardo, L. Angelani, D. Dell'Arciprete, G. Ruocco, V. Iebba, S. Schippa, M. P. Conte, F. Mecarini, F. De Angelis, and E. Di Fabrizio. Bacterial ratchet motors. *Proceedings of the National Academy of Sciences*, 107(21):9541–9545, 2010.

[62] Mikayla L Carlson, Sean L Seyler, and Steve Pressé. Swimming, fast and slow: strategy and survival of bacterial predators in response to chemical cues. *bioRxiv*, 2020.

[63] Kristian Gustavsson, Luca Biferale, Antonio Celani, and Simona Colabrese. Finding efficient swimming strategies in a three-dimensional chaotic flow by reinforcement learning. *The European Physical Journal E*, 40(12):1–6, 2017.

[64] Eric Lauga. Bacterial hydrodynamics. *Annual Review of Fluid Mechanics*, 48(1):105–130, 2016.

[65] Maximilian Seyrich, Zahra Alirezaeizanjani, Carsten Beta, and Holger Stark. Statistical parameter inference of bacterial swimming strategies. *New Journal of Physics*, 20(10):103033, 2018.

[66] Anders Andersen, Navish Wadhwa, and Thomas Kiørboe. Quiet swimming at low reynolds number. *Phys. Rev. E*, 91:042712, Apr 2015.

[67] Giorgio Pessot, Hartmut Löwen, and Andreas M. Menzel. Binary pusher–puller mixtures of active microswimmers and their collective behaviour. *Molecular Physics*, 116(21-22):3401–3408, 2018.

[68] M. Borgnino, K. Gustavsson, F. De Lillo, G. Boffetta, M. Cencini, and B. Mehlig. Alignment of nonspherical active particles in chaotic flows. *Phys. Rev. Lett.*, 123:138003, Sep 2019.

[69] Enkeleida Lushi, Hugo Wioland, and Raymond E. Goldstein. Fluid flows created by swimming bacteria drive self-organization in confined suspensions. *Proceedings of the National Academy of Sciences*, 111(27):9733–9738, 2014.

[70] Dóra Bárdfalvy, Shan Anjum, Cesare Nardini, Alexander Morozov, and Joakim Stenhammar. Symmetric mixtures of pusher and puller microswimmers behave as noninteracting suspensions. *Physical Review Letters*, 125(1):018003, 2020.

[71] Filippo De Lillo, Massimo Cencini, William M. Durham, Michael Barry, Roman Stocker, Eric Climent, and Guido Boffetta. Turbulent fluid acceleration generates clusters of gyrotactic microorganisms. *Phys. Rev. Lett.*, 112:044502, Jan 2014.

[72] Charu Datt and Gwynn J Elfring. Active particles in viscosity gradients. *Physical review letters*, 123(15):158006, 2019.

[73] Christian Hoell, Hartmut Löwen, and Andreas M. Menzel. Particle-scale statistical theory for hydrodynamically induced polar ordering in microswimmer suspensions. *The Journal of Chemical Physics*, 149(14):144902, 2018.

[74] Markus Bär, Robert Großmann, Sebastian Heidenreich, and Fernando Peruani. Self-propelled rods: Insights and perspectives for active matter. *Annual Review of Condensed Matter Physics*, 11:441–466, 2020.

[75] L Huber, R Suzuki, T Krüger, E Frey, and AR Bausch. Emergence of coexisting ordered states in active matter systems. *Science*, 361(6399):255–258, 2018.

[76] François-Gaël Michalec, Itzhak Fouxon, Sami Souissi, and Markus Holzner. Zooplankton can actively adjust their motility to turbulent flow. *Proceedings of the National Academy of Sciences*, 114(52):E11199–E11207, 2017.

[77] Anupam Sengupta, Francesco Carrara, and Roman Stocker. Phytoplankton can actively diversify their migration strategy in response to turbulent cues. *Nature*, 543(7646):555–558, 2017.

[78] Heidi L. Fuchs and Gregory P. Gerbi. Seascape-level variation in turbulence- and wave-generated hydrodynamic signals experienced by plankton. *Progress in Oceanography*, 141:109 – 129, 2016.

[79] D. M. Fields, D. S. Sheaffer, and M. J. Weissburg. Mechanical and neural responses from the mechanosensory hairs on the antennule of gaussia princeps. *Mar. Ecol. Prog. Ser.*, 227:176–186, 2019.

[80] Xiaohe Hu, Yonggang Jiang, Zhiqiang Ma, Yuanhang Xu, and Deyuan Zhang. Bioinspired flexible lateral line sensor based on p (vdf-trfe)/bto nanofiber mat for hydrodynamic perception. *Sensors*, 19(24):5384, 2019.

[81] Siti Nurmaini and Tutuko Bambang. Intelligent robotics navigation system: Problems, methods, and algorithm. *International Journal of Electrical and Computer Engineering*, 7:pp. 3711–3726, 2017.

[82] M. Kruusmaa, P. Fiorini, W. Megill, M. de Vittorio, O. Akanyeti, F Visentin, L. Chambers, H. El Daou, M. Fiazza, J. Ježov, M. Listak, Rossi L., T. Salumae, Toming G., R. Venturelli, D. S. Jung, Brown J., F. Rizzi, A. Qualtieri, J. L. Maud, and A. Liszewski. Filose for svenning: A flow sensing bioinspired robot. *IEEE Robotics Automation Magazine*, 21(3):51–62, 2014.

[83] Yonggang Jiang, Zhiqiang Ma, and Deyuan Zhang. Flow field perception based on the fish lateral line system. *Bioinspiration & Biomimetics*, 14(4):041001, may 2019.

[84] B. Colvert, G. Liu, H. Dong, and E. Kanso. How can a source be located by responding to local information in its hydrodynamic trail? In *2017 IEEE 56th Annual Conference on Decision and Control (CDC)*, pages 2756–2761, 2017.

[85] William C Eberhardt, Brendan F Wakefield, Christin T Murphy, Caroline Casey, Yousef Shakhsheer, Benton H Calhoun, and Colleen Reichmuth. Development of an artificial sensor for hydrodynamic detection inspired by a seal's whisker array. *Bioinspiration & Biomimetics*, 11(5):056011, aug 2016.

[86] M. Fitzpatrick, G. M. Reis, J. Anderson, L. Bobadilla, W. Al Sabban, and R. N. Smith. Development of environmental niche models for use in underwater vehicle navigation. *IET Cyber-systems and Robotics*, 2(2):67–77, 2020.

[87] Enkeleida Lushi and Charles S Peskin. Modeling and simulation of active suspensions containing large numbers of interacting micro-swimmers. *Computers & Structures*, 122:239–248, 2013.

[88] NH Brummell, F Cattaneo, and SM Tobias. Linear and nonlinear dynamo properties of time-dependent abc flows. *Fluid Dynamics Research*, 28(4):237, 2001.

[89] Arash Alizad Banaei, Marco Edoardo Rosti, and Luca Brandt. Numerical study of filament suspensions at finite inertia. *Journal of Fluid Mechanics*, 882, 2020.

[90] Alexandre M Roma, Charles S Peskin, and Marsha J Berger. An adaptive version of the immersed boundary method. *Journal of computational physics*, 153(2):509–534, 1999.

[91] Arash Alizad Banaei, Marco Edoardo Rosti, and Luca Brandt. Numerical study of filament suspensions at finite inertia. *Journal of Fluid Mechanics*, 882, 2020.

[92] Stefano Olivieri, Assad Akoush, Luca Brandt, Marco E Rosti, and Andrea Mazzino. Turbulence in a network of rigid fibers. *Physical Review Fluids*, 5(7):074502, 2020.

[93] Stefano Olivieri, Luca Brandt, Marco E Rosti, and Andrea Mazzino. Dispersed fibers change the classical energy budget of turbulence via nonlocal transfer. *Physical Review Letters*, 125(11):114501, 2020.

[94] Y.N. Young and M. J. Shelley. Stretch-coil transition and transport of fibers in cellular flows. *Phys. Rev. Lett.*, 99:058303, Aug 2007.

[95] N. Quennouz, M. Shelley, O. Du Roure, and A. Lindner. Transport and buckling dynamics of an elastic fibre in a viscous cellular flow. *J. Fluid Mech.*, 769:387–402, 2015.

[96] Joost de Graaf and Joakim Stenhammar. Stirring by periodic arrays of microswimmers. *Journal of Fluid Mechanics*, 811:487–498, 2017.

[97] Thomas Kiørboe, Houshuo Jiang, Rodrigo Javier Gonçalves, Lasse Tor Nielsen, and Navish Wadhwa. Flow disturbances generated by feeding and swimming zooplankton. *Proceedings of the National Academy of Sciences*, 111(32):11738–11743, 2014.

[98] Xiao-Hua Zhao, Keng-Huat Kwek, JI-Bin Li, and Ke-Lei Huang. Chaotic and resonant streamlines in the abc flow. *SIAM Journal on Applied Mathematics*, 53(1):71–77, 1993.

[99] J.K. Eaton and J.R. Fessler. Preferential concentration of particles by turbulence. *Int. J. Multiph. Flow*, 20:169 – 209, 1994.

[100] J. Bec, L. Biferale, G. Boffetta, A. Celani, M. Cencini, A. Lanotte, S. Musacchio, and F. Toschi. Acceleration statistics of heavy particles in turbulence. *J. Fluid Mech.*, 550:349–358, 2006.

[101] J. Bec, L. Biferale, M. Cencini, A. Lanotte, S. Musacchio, and F. Toschi. Heavy particle concentration in turbulence at dissipative and inertial scales. *Phys. Rev. Lett.*, 98:084502, Feb 2007.

[102] J. H. E. Cartwright, U. Feudel, G. Károlyi, A. de Moura, O. Piro, and T. Tél. *Dynamics of Finite-Size Particles in Chaotic Fluid Flows*, pages 51–87. Springer Berlin Heidelberg, Berlin, Heidelberg, 2010.

[103] P. Castiglione, A. Crisanti, A. Mazzino, M. Vergassola, and A. Vulpiani. Resonant enhanced diffusion in time-dependent flow. *J. Phys. A: Math. Gen.*, 31(35):7197–7210, sep 1998.

[104] Diego Lopez and Elisabeth Guazzelli. Inertial effects on fibers settling in a vortical flow. *Physical Review Fluids*, 2(2):024306, 2017.

[105] Nicholas G Chisholm, Dominique Legendre, Eric Lauga, and Aditya S Khair. A squirmer across reynolds numbers. *Journal of Fluid Mechanics*, 796:233–256, 2016.

[106] D. Krug, M. Holzner, B. Lüthi, M. Wolf, A. Tsinober, and W. Kinzelbach. A combined scanning PTV/LIF technique to simultaneously measure the full velocity gradient tensor and the 3D density field. *Meas. Sci. Technol.*, 25(6):065301, apr 2014.

[107] J. M. Lawson and J. R. Dawson. A scanning PIV method for fine-scale turbulence measurements. *Exp. Fluids*, 55(12):1857, Nov 2014.

[108] Lydia Bourouiba, Eline Dehandschoewercker, and John WM Bush. Violent expiratory events: on coughing and sneezing. *Journal of Fluid Mechanics*, 745:537–563, 2014.

[109] Jitendra K Gupta, C-H Lin, and Q Chen. Flow dynamics and characterization of a cough. *Indoor air*, 19(6):517–525, 2009.

[110] Bin Zhao, Zhao Zhang, and Xianting Li. Numerical study of the transport of droplets or particles generated by respiratory system indoors. *Building and Environment*, 40(8):1032–1039, 2005.

[111] Shengwei Zhu, Shinsuke Kato, and Jeong-Hoon Yang. Study on transport characteristics of saliva droplets produced by coughing in a calm indoor environment. *Building and environment*, 41(12):1691–1702, 2006.

[112] Yu Feng, Thierry Marchal, Ted Sperry, and Hang Yi. Influence of wind and relative humidity on the social distancing effectiveness to prevent covid-19 airborne transmission: A numerical study. *Journal of aerosol science*, 147:105585, 2020.

[113] LJGR Morawska, GR Johnson, ZD Ristovski, Megan Hargreaves, Kerrie Mengersen, Shay Corbett, Christopher Yu Hang Chao, Yuguo Li, and David Katoshevski. Size distribution and sites of origin of droplets expelled from the human respiratory tract during expiratory activities. *Journal of aerosol science*, 40(3):256–269, 2009.

[114] Hans R Pruppacher and James D Klett. Microstructure of atmospheric clouds and precipitation. In *Microphysics of clouds and precipitation*, pages 10–73. Springer, 2010.

[115] JP Duguid. The size and the duration of air-carriage of respiratory droplets and droplet-nuclei. *Epidemiology & Infection*, 44(6):471–479, 1946.

[116] Leslie SG Kovasznay, Hajime Fujita, and Rena L Lee. Unsteady turbulent puffs. In *Advances in Geophysics*, volume 18, pages 253–263. Elsevier, 1975.

[117] Mazzino Andrea and Rosti Marco Edoardo. Unraveling the secrets of turbulence in a fluid puff. *Physical Review Letters*, 127(9), 2021.

[118] Lewis Fry Richardson. Atmospheric diffusion shown on a distance-neighbour graph. *Proceedings of the Royal Society of London. Series A, Containing Papers of a Mathematical and Physical Character*, 110(756):709–737, 1926.

[119] Martin R Maxey and James J Riley. Equation of motion for a small rigid sphere in a nonuniform flow. *The Physics of Fluids*, 26(4):883–889, 1983.

[120] Marco Martins Afonso, Paolo Muratore-Ginanneschi, Sílvio MA Gama, and Andrea Mazzino. Eddy diffusivity of quasi-neutrally-buoyant inertial particles. *Physical Review Fluids*, 3(4):044501, 2018.

[121] Eric P Vejerano and Linsey C Marr. Physico-chemical characteristics of evaporating respiratory fluid droplets. *Journal of The Royal Society Interface*, 15(139):20170939, 2018.

[122] Marcus Roper, Agnese Seminara, MM Bandi, Ann Cobb, Helene R Dillard, and Anne Pringle. Dispersal of fungal spores on a cooperatively generated wind. *Proceedings of the National Academy of Sciences*, 107(41):17474–17479, 2010.

[123] Lian-Ping Wang and Martin R Maxey. Settling velocity and concentration distribution of heavy particles in homogeneous isotropic turbulence. *Journal of fluid mechanics*, 256:27–68, 1993.

[124] GR Johnson, Lidia Morawska, ZD Ristovski, Megan Hargreaves, Kerrie Mengersen, Christopher Yu Hang Chao, MP Wan, Y Li, Xaiojan Xie, David Katoshevski, et al. Modality of human expired aerosol size distributions. *Journal of Aerosol Science*, 42(12):839–851, 2011.

[125] Ulrike Lohmann, Felix Lüönd, and Fabian Mahrt. *An introduction to clouds: From the microscale to climate*. Cambridge University Press, 2016.

[126] Guang Zeng, Judas Kelley, J Duncan Kish, and Yong Liu. Temperature-dependent deliquescent and efflorescent properties of methanesulfonate sodium studied by atr-ftir spectroscopy. *The Journal of Physical Chemistry A*, 118(3):583–591, 2014.

[127] Mark Nicas, William W Nazaroff, and Alan Hubbard. Toward understanding the risk of secondary airborne infection: emission of respirable pathogens. *Journal of occupational and environmental hygiene*, 2(3):143–154, 2005.

[128] John Monteith and Mike Unsworth. *Principles of environmental physics: plants, animals, and the atmosphere*. Academic Press, 2013.

[129] Li Liu, Yuguo Li, Peter Vilhelm Nielsen, Jianjian Wei, and Rasmus Lund Jensen. Short-range airborne transmission of expiratory droplets between two people. *Indoor air*, 27(2):452–462, 2017.

[130] https://groups.oist.jp/cffu/code.

[131] Boris I Shraiman and Eric D Siggia. Scalar turbulence. *Nature*, 405(6787):639–646, 2000.

[132] Chiara Nironi, Pietro Salizzoni, Massimo Marro, Patrick Mejean, Nathalie Grosjean, and Lionel Soulhac. Dispersion of a passive scalar fluctuating plume in a turbulent boundary layer. part i: Velocity and concentration measurements. *Boundary-layer meteorology*, 156(3):415–446, 2015.

[133] Sima Asadi, Anthony S Wexler, Christopher D Cappa, Santiago Barreda, Nicole M Bouvier, and William D Ristenpart. Aerosol emission and superemission during human speech increase with voice loudness. *Scientific reports*, 9(1):1–10, 2019.

[134] Carl Flügge. Ueber luftinfection. *Zeitschrift für Hygiene und Infektionskrankheiten*, 25(1):179–224, 1897.

[135] William F Wells. On air-borne infection: study ii. droplets and droplet nuclei. *American journal of Epidemiology*, 20(3):611–618, 1934.

[136] Giovanni Seminara, Bruno Carli, Guido Forni, Sandro Fuzzi, Andrea Mazzino, and Andrea Rinaldo. Biological fluid dynamics of airborne covid-19 infection. *Rendiconti Lincei. Scienze fisiche e naturali*, pages 1–33, 2020.

[137] Gustavo Zayas, Ming C Chiang, Eric Wong, Fred MacDonald, Carlos F Lange, Ambikaipakan Senthilselvan, and Malcolm King. Cough aerosol in healthy participants: fundamental knowledge to optimize droplet-spread infectious respiratory disease management. *BMC pulmonary medicine*, 12(1):1–12, 2012.

[138] Shinhao Yang, Grace WM Lee, Cheng-Min Chen, Chih-Cheng Wu, and Kuo-Pin Yu. The size and concentration of droplets generated by coughing in human subjects. *Journal of Aerosol Medicine*, 20(4):484–494, 2007.

[139] Mark D Sobsey and John Scott Meschke. Virus survival in the environment with special attention to survival in sewage droplets and other environmental media of fecal or respiratory origin. *Report for the World Health Organization, Geneva, Switzerland*, 70:19–39, 2003.

[140] Alyssa C Fears, William B Klimstra, Paul Duprex, Amy Hartman, Scott C Weaver, Kenneth S Plante, Divya Mirchandani, Jessica Ann Plante, Patricia V Aguilar, Diana Fernández, et al. Early release-persistence of severe acute respiratory syndrome coronavirus 2 in aerosol suspensions.

[141] Xiaojian Xie, Yuguo Li, Hequan Sun, and Li Liu. Exhaled droplets due to talking and coughing. *Journal of the Royal Society Interface*, 6(suppl_6):S703–S714, 2009.

[142] Rajat Mittal, Rui Ni, and Jung-Hee Seo. The flow physics of covid-19. *Journal of fluid Mechanics*, 894, 2020.

[143] Alyssa C Fears, William B Klimstra, Paul Duprex, Amy Hartman, Scott C Weaver, Kenneth S Plante, Divya Mirchandani, Jessica Ann Plante, Patricia V Aguilar, Diana Fernández, et al. Persistence of severe acute respiratory syndrome coronavirus 2 in aerosol suspensions. *Emerging infectious diseases*, 26(9):2168, 2020.

[144] Ryan Vincent William Endersby, Esther Ching Yee Ho, Adam Oscar Spencer, David Howard Goldstein, and Edward Schubert. Barrier devices for reducing aerosol and droplet transmission in covid-19 patients: advantages, disadvantages, and alternative solutions. *Anesthesia & Analgesia*, 131(2):e121–e123, 2020.

[145] Karthika Asokan, Bibilash Babu, and Arya Jayadevan. Barrier enclosure for airway management in covid-19 pandemic. *Indian Journal of Anaesthesia*, 64(Suppl 2):S153, 2020.

[146] Prok Laosuwan, Athitarn Earsakul, Patt Pannangpetch, and Jariya Sereeyotin. Acrylic box versus plastic sheet covering on droplet dispersal during extubation in covid-19 patients. *Anesthesia and Analgesia*, 2020.

[147] Eric A Fried, George Zhou, Ronak Shah, Da Wi Shin, Anjan Shah, Daniel Katz, and Garrett W Burnett. Barrier devices, intubation, and aerosol mitigation strategies: Personal protective equipment in the time of coronavirus disease 2019. *Anesthesia and analgesia*, 2020.

[148] Guido Boffetta and Andrea Mazzino. Incompressible Rayleigh–Taylor turbulence. *Annual Review of Fluid Mechanics*, 49:119–143, 2017.

[149] Murry L Salby. *Fundamentals of atmospheric physics*. Elsevier, 1996.

[150] Takeo Kajishima, TAKIGUCHI Satoshi, Hiroyuki HAMASAKI, and Yutaka MIYAKE. Turbulence structure of particle-laden flow in a vertical plane channel due to vortex shedding. *JSME International Journal Series B Fluids and Thermal Engineering*, 44:526–535, 2001.

[151] Lydia Bourouiba. Turbulent Gas Clouds and Respiratory Pathogen Emissions: Potential Implications for Reducing Transmission of COVID-19. *JAMA*, 323(18):1837–1838, 05 2020.

[152] On Shun Pak and Eric Lauga. Generalized squirming motion of a sphere. *Journal of Engineering Mathematics*, 88(1):1–28, 2014.

[153] Gaojin Li, Anca Ostace, and Arezoo M Ardekani. Hydrodynamic interaction of swimming organisms in an inertial regime. *Physical Review E*, 94(5):053104, 2016.

Publications

Cavaiola, M., Olivieri, S., and Mazzino, A. (2020). The assembly of freely moving rigid fibres measures the flow velocity gradient tensor. Journal of Fluid Mechanics, 894, A25. doi:10.1017/jfm.2020.288

Rosti, M.E., Olivieri, S., Cavaiola, M. Seminara, A., and Mazzino A. (2020). Fluid dynamics of COVID-19 airborne infection suggests urgent data for a scientific design of social distancing. Sci Rep 10, 22426. https://doi.org/10.1038/s41598-020-80078-7

Rosti, M. E., Cavaiola, M., Olivieri, S., Seminara, A., and Mazzino, A. (2021). Turbulence role in the fate of virus-containing droplets in violent expiratory events. Physical Review Research, 3(1), 013091

Cavaiola, M., and Mazzino A. (2021). Self-propelled slender objects can measure flow signals net of self-motion. Physics of Fluids 33, 053603 https://doi.org/10.1063/5.0051325

Cavaiola, M., Olivieri, S., Guerrero, J., Mazzino, A., and Rosti, M. E. (2022). Role of barriers in the airborne spread of virus-containing droplets: a study based on high-resolution direct numerical simulations. Physics of Fluids 34, 015104 https://doi.org/10.1063/5.0072840

Olivieri, S., Cavaiola, M., Mazzino, A. and Rosti, M. E. (2022). Transport and evaporation of virus-containing droplets exhaled by men and women in typical cough events. Meccanica 57, 567–575. https://doi.org/10.1007/s11012-021-01469-2

Cavaiola, M. (2022). Suspension of slender swimmers at finite Reynolds numbers. Physics of Fluids 34, 027113 https://doi.org/10.1063/5.0081866